Fatigue behavior of impacted carbon fiber reinforced plastics

Biagini, D.

DOI
10.4233/uuid:09ac860d-dbf7-4d02-a750-8267afbdb26a

Publication date
2024

Document Version
Final published version

Citation (APA)
Biagini, D. (2024). *Fatigue behavior of impacted carbon fiber reinforced plastics*. [Dissertation (TU Delft), Delft University of Technology]. https://doi.org/10.4233/uuid:09ac860d-dbf7-4d02-a750-8267afbdb26a

Propositions

accompanying the dissertation

Fatigue behavior of impacted carbon fiber reinforced plastics

by

Davide Biagini

1. In composite post-impact fatigue research, the rapid growth of planar delamination receives the most attention but is the least interesting phase of damage propagation. (This proposition pertains to this dissertation)
2. Fatigue after impact in composites can be described only if different damage processes activated at different load levels are considered.
(This proposition pertains to this dissertation)
3. Applying the no-growth approach should not absolve the composite community from providing a rigorous definition of growth.
(This proposition pertains to this dissertation)
4. Future research on damage modes identification via acoustic emissions should prioritize modelling of source and propagation over complex data analysis strategies.
5. Scientists formulate questions more than they provide answers; generative AI does not alter their role significantly.
6. For scientists climate change is a topic, for policymakers a responsibility.
7. Behind meritocracy is the false belief that people deserve their lack of success.
8. Self-doubt is vital in the development of a Ph.D. candidate and should be treated as a soft skill.
9. Education, at any level, should cultivate passion; acquisition of knowledge and skills is consequential.
10. Happiness has cheap ingredients, like pizza.

These propositions are regarded as opposable and defendable, and have been approved as such by the promotor dr. R. C. Alderliesten

Fatigue behavior of impacted carbon fiber reinforced plastics

Fatigue behavior of impacted carbon fiber reinforced plastics

Proefschrift

ter verkrijging van de graad van doctor
aan de Technische Universiteit Delft,
op gezag van de Rector Magnificus Prof. dr. ir. T.H.J.J. van der Hagen,
voorzitter van het College voor Promoties,
in het openbaar te verdedigen op
Dinsdag, 15 oktober 2024 om 10:00 uur

door

Davide BIAGINI

Master of Science in Aerospace Engineering,
University of Bologna, Italië,
geboren te Modena, Italië.

Dit proefschrift is goedgekeurd door de

promotor: Dr. ir. R. C. Alderliesten
copromotor: Dr. ir. J. A. Pascoe

Samenstelling promotiecommissie:

Rector Magnificus,	voorzitter
Dr. ir. R. C. Alderliesten,	Technische Universiteit Delft
Dr. ir. J. A. Pascoe,	Technische Universiteit Delft

Onafhankelijke leden:	
Prof. dr. G. Allegri	University of Bristol
Prof. dr. E. Lindgaard	Aalborg University
Prof. dr. C. Kassapoglou	Technische Universiteit Delft
Dr. ir. L. Warnet	University of Twente
Dr. D. Zarouchas	Technische Universiteit Delft
Prof. dr. ir. R. Benedictus	Technische Universiteit Delft, reservelid

Keywords: Composite Materials, Fatigue, Impact damage, Delamination, Acoustic Emission, Ultrasound scan

Printed by: Impskamp printing

Cover:

ISBN …

An electronic version of this dissertation is available at
http://repository.tudelft.nl/.

Contents

Summary

Impacts in aviation are so common that it's more a question of 'when' than 'if' they will occur during the lifetime of an aircraft. Potential sources include bird strikes, unconfined engine failures, foreign objects on runways, hailstorms, tools accidentally dropped during maintenance, and more. Carbon fiber reinforced polymers (CFRP), increasingly used in aviation, dissipate impact energy through various fracture mechanisms originating inside the material. The resulting damage is often a complex structure composed of multiple delaminations, intralaminar matrix cracks and fiber failures. Despite causing extensive damage, low-energy impacts may leave only small surface dents, making detection difficult and allowing several flights to pass before damage is noticed. It was observed that if cyclic load is applied to impacted components, the impact damage can act as an initiation site for fatigue phenomena. Compression fatigue in particular, once of little relevance for metals, is now crucial for assessing damage tolerance in CFRP aeronautical structures due to several instabilities affecting the impacted composite structure like buckling and fiber kinking.

In the past, several experimental studies have provided a description of compression after impact fatigue growth focusing on the projected delamination area or width. Among these tests, there is a discrepancy between observations reporting a phase in which no delamination growth outside of the impact delamination projected area was followed by phases of fast and unstable growth and other observations in which the growth of delamination was observed from the beginning of fatigue life. Despite the effort made in previous research, it is unclear how fatigue after impact growth should be defined and which phases constitute the process. Considering this knowledge gap, and the relevance of this topic for civil aviation, the primary goal of this thesis was to conduct fundamental research on the phenomenon of compression after impact (CAI) fatigue.

CAI fatigue tests were conducted and delamination propagation was monitored by adopting a combination of ultrasound through thickness attenuation and pulse-echo scans. In addition to ultrasounds, digital image correlation (DIC) analysis was used to track the local buckling of sublaminates and provide an indirect measurement of delaminations situated close to the impacted surface. The through-thickness transmission scan showed initial growth of delamination in the non-delaminated cone, a phenomenon previously documented only in quasi-static CAI tests. The echo-pulse scan revealed the initial growth of shorter delaminations located close to the impacted face falling within the projected damage area. Both of these phenomena occurred before the onset of delamination growth perpendicular to the loading direction, extending beyond the projected delamination area and could have been classified as no-growth phases by previous studies overlooking these phenomena.

The selection of the wrong damage descriptors however, was not sufficient to explain the discrepancies observed in growth trends by previous works. In the case of long-life fatigue tests, an initial no-growth phase was present, even when using a more precise damage descriptor that considers the early growth of shallow delaminations. These findings suggested that the behavior of fatigue damage propagation could vary depending on the applied load and the local stresses within the impact damage area.

To investigate what was happening in the initial phase of no apparent growth and provide an updated description of fatigue after impact phenomenon, acoustic emission monitoring was adopted. A series of preliminary experiments were conducted on various layups to isolate acoustic signals and associate them with specific damage modes. The knowledge acquired in the preliminary tests was then applied to the monitoring of quasi-static and fatigue CAI tests. To analyze acoustic emissions in CAI fatigue tests, a convolutional neural network was developed to perform the classification of signals based on their wavelet coefficients.

The quasi-static CAI test monitoring revealed how different phases of damage propagation take place at different load levels. Progressively increasing the compressive load a variation of the active damage modes and the scale of damage events was observed. Also the fatigue tests showed how the effect of varying maximum compressive stress must be considered in the description of CAI fatigue. Depending on the applied stress, phases of damage propagation characterized by different activities of the damage modes occurred. Considering the results it was hypothesized that load thresholds may exist determining different phases in fatigue life, such as the immediate growth of delamination, a phase of transition before delamination where damage propagates undetected by C-scan, or an absolute no-growth behavior. Changing the compressive stress applied to the impacted coupon not only affects the velocity of propagation and the expected fatigue life but also alters the 'history', i.e., the sequence of phases in damage propagation.

In addition to the phenomenological study of CAI fatigue, surrogate tests were conducted to observe the compression fatigue growth of 'surrogate' impact damage, recreated using multiple PTFE inclusions inside the laminate. By utilizing this approach, similar and dissimilar growth patterns were observed, compared to CAI fatigue tests. Similarly to CAI fatigue, in an advanced growth state, the planar growth of multiple delaminations in the perpendicular to load direction happened. The dissimilarities regarded the position in depth of delamination growth and the local buckling profiles. Despite the limitations, the fatigue growth of multiple planar delaminations was obtained in compression fatigue. The growth of these delaminations, in opposition to fatigue after impact cases, proved to be slow and stable. This suggests that, if the conditions are similar to the surrogate, a 'slow growth' of planar delamination can happen in compression fatigue.

The surrogate tests were used to validate a VCCT numerical analysis with suppressed propagation, which was devised to capture the strain energy release rate profiles in a simplified version of impact damage. A parametric analysis was then conducted analyzing different configurations of impact damage and boundary conditions. It was found that a state with global buckling without restrictions promotes the increase of SERR in a single interface. On the contrary, suppressed global buckling and enhanced local buckling produce high SERR in multiple interfaces of the same damage geometry. This observation has important implications since in many applications global buckling is unrestrained. It was also estimated that the growth inside the impact cone, a phenomenon documented in the CAI fatigue test in this thesis, may depend on the size of the non-delaminated central area generated during the impact.

Samenvatting

Inslagen in de luchtvaart zijn zo gebruikelijk dat het meer een kwestie is van 'wanneer' dan 'of' ze zullen voorkomen tijdens de levensduur van een vliegtuig. Potentiële oorzaken zijn onder meer vogelaanvaringen, ongecontroleerde motorstoringen, vreemde voorwerpen op landingsbanen, hagelstormen, gereedschap dat per ongeluk tijdens onderhoud wordt laten vallen, enzovoorts. Koolstofvezelversterkte polymeren (CFRP), welke steeds vaker gebruikt worden in de luchtvaart, dissiperen inslagenergie via verschillende breukmechanismen die binnen in het materiaal ontstaan. De resulterende schade is vaak een complexe structuur bestaande uit meerdere delaminaties, intralaminaire matrixscheuren en gebroken vezels. Ondanks dat ze uitgebreide schade veroorzaken, kunnen inslagen met een lage energie slechts kleine oppervlaktedeukjes achterlaten, waardoor detectie moeilijk is en er meerdere vluchten kunnen passeren voordat de schade wordt opgemerkt. Er is waargenomen dat als cyclische belasting wordt toegepast op getroffen componenten, de inslagschade kan dienen als initiatieplaats voor vermoeiingsverschijnselen. Compressievermoeiing, eens van weinig belang voor metalen, is nu cruciaal voor het beoordelen van schadetolerantie in CFRP-luchtvaartconstructies vanwege verschillende instabiliteiten die de getroffen composietstructuur beïnvloeden, zoals knikken en vezelverbuiging.

In het verleden hebben verschillende experimentele studies een beschrijving gegeven van de groei van vermoeiing ten gevolge van compressie na inslag, waarbij de nadruk lag op het geprojecteerde delaminatieoppervlakte of de breedte hiervan. Onder deze experimenten is er een discrepantie tussen observaties welke een fase rapporteren waarin geen delaminatiegroei buiten het geprojecteerde gebied van delaminatie na inslag plaatsvond, gevolgd door fasen van snelle en onstabiele groei, en andere observaties waarin de groei van delaminatie vanaf het begin van de vermoeiingslevensduur werd waargenomen. Ondanks de inspanningen in eerdere onderzoeken is het onduidelijk hoe de groei van vermoeiing na inslag moet worden gedefinieerd en welke fasen het proces defineren. Gezien deze kennislacune en de relevantie van dit onderwerp voor de burgerluchtvaart, is het primaire doel van deze scriptie om fundamenteel onderzoek uit te voeren naar het fenomeen van compressievermoeiing na inslag (CAI-vermoeiing).

CAI-vermoeiingsproeven zijn uitgevoerd waarbij delaminatiepropagatie is gevolgd doormiddel van een combinatie van ultrasone transmissie verzwakking door de materiaaldiepte en pulse-echo-scans. Naast ultrasone scans is digitale beeldcorrelatie (DIC) -analyse gebruikt om de lokale knik van sublaminaat en te volgen en een indirecte meting van delaminaties dicht bij het getroffen oppervlak te maken. De scan door de dikte heen toont aanvankelijke groei van delaminatie in de niet-gedelamineerde kegel, een fenomeen dat eerder alleen is gedocumenteerd in quasi-statische CAI-proeven. De echo pulse scan toont de aanvankelijke groei van kortere delaminaties welke zich dicht bij het getroffen oppervlak bevonden, binnen het geprojecteerde schadegebied. Beide fenomenen zijn aanwezig voor het begin van de groei van delaminatie loodrecht op de beladingsrichting, die zich uitstrekte buiten het geprojecteerde delaminatiegebied en welke door eerdere studies,

die deze fenomenen over het hoofd zagen, als geen-groeifasen zouden kunnen worden geclassificeerd.

Het selecteren van verkeerde schadedescriptoren is echter niet voldoende om de waargenomen discrepanties in groeitrends door eerdere werken te verklaren. In het geval van vermoeiingsproeven met een lange levensduur was een initiële fase zonder groei aanwezig, zelfs bij het gebruik van een nauwkeurigere schadedescriptor welke rekening houdt met de vroege groei van oppervlakkige delaminaties. Deze bevindingen suggereren dat het gedrag van vermoeiingsschadepropagatie kan variëren afhankelijk van de toegepaste belasting en de lokale spanningen binnen het gebied van de inslagschade.

Om te onderzoeken wat er gebeurt in de initiële fase zonder schaanbare groei en een bijgewerkte beschrijving van het fenomeen van vermoeiing na inslag te bieden, is akoestische emissiemonitoring toegepast. Een reeks voorlopige experimenten is uitgevoerd op verschillende laminaten om akoestische signalen te isoleren en te associëren met specifieke schademodi. De kennis welke is opgedaan in de voorlopige proeven, is vervolgens toegepast op de monitoring van quasi-statische en vermoeiings CAI-proeven. Om akoestische emissies in CAI-vermoeiingsproeven te analyseren, is een 'convolutional neural network' ontwikkeld om classificatie van signalen uit te voeren op basis van hun wavelet-coëfficiënten.

De monitoring van quasi-statische CAI-proeven onthulde hoe verschillende fasen van schadepropagatie plaatsvinden bij verschillende belastingsniveaus. Bij het progressief verhogen van de compressieve belasting werd een variatie van de actieve schademodi en de omvang van schadegebeurtenissen waargenomen. Ook de vermoeiingsproeven toonden aan hoe het effect van variërende maximale compressieve spanning moet worden meegenomen in de beschrijving van CAI-vermoeiing. Afhankelijk van de toegepaste spanning deden zich fasen van schadepropagatie voor die werden gekenmerkt door verschillende activiteit van de schademodi. Op basis van de resultaten werd verondersteld dat belastingdrempels kunnen bestaan die verschillende fasen in de vermoeiingslevensduur bepalen, zoals de onmiddellijke groei van delaminatie, een overgangsfase vóór delaminatie waarin schade zich voortplant zonder door C-scan te worden gedetecteerd, of een absoluut geen-groei-gedrag. Het veranderen van de toegepaste compressieve spanning op de getroffen coupon beïnvloedt niet alleen de snelheid van propagatie en de verwachte vermoeiingslevensduur, maar verandert ook de 'geschiedenis', d.w.z. de volgorde van fasen in schadepropagatie.

Naast de fenomenologische studie van CAI-vermoeiing werden surrogaatproeven uitgevoerd om de compressievermoeiingsgroei van 'surrogaat'-inslagschade te observeren, nagemaakt met behulp van meerdere PTFE-inclusies in het laminaat. Door deze benadering te gebruiken, werden vergelijkbare en verschillende groeipatronen waargenomen in vergelijking met CAI-vermoeiingsproeven. Net als bij CAI-vermoeiing vond in een gevorderde groeifase de vlakke groei van meerdere delaminaties loodrecht op de belastingsrichting plaats. De verschillen betroffen de positie in de diepte van delaminatiegroei en de lokale buigprofielen. Ondanks de beperkingen werd de vermoeiingsgroei van meerdere vlakke delaminaties verkregen bij compressievermoeiing. De groei van deze delaminaties, in tegenstelling tot vermoeiing na imnslaggevallen, bleek traag en stabiel te zijn. Dit suggereert dat, als de omstandigheden vergelijkbaar zijn met het surrogaat, een 'trage groei' van vlakke delaminatie kan optreden bij compressievermoeiing.

De surrogaatproeven werden gebruikt om een virtuele scheursluitingstechniek (VCCT) numerieke analyse met onderdrukte propagatie te valideren, die was ontworpen om de profielen van de vrijgave van de rekenergie in een vereenvoudigde versie van inslagschade vast te leggen. Daarna werd een parametrische analyse uitgevoerd waarbij verschillende configuraties van inslagschade en randvoorwaarden werden geanalyseerd. Er werd vastgesteld dat een toestand met globale buiging zonder beperkingen de toename van SERR in een enkele interface bevordert. Darentegen produceren, onderdrukte globale buiging en verbeterde lokale buiging hoge SERR in meerdere interfaces van dezelfde schadegeometrie. Deze observatie heeft belangrijke implicaties aangezien in veel toepassingen globale buiging onbelemmerd is. Er werd ook geschat dat de groei binnen de inslagkegel, een fenomeen dat in de CAI-vermoeiingstest in dit proefschrift is gedocumenteerd, kan afhangen van de grootte van het niet-delamineerde centrale gebied dat tijdens de inslag wordt gegenereerd.

1

Introduction

Despite the effort made in previous research, the comprehension of fatigue after impact in carbon fiber reinforced polymers (CFRP) remains limited. We do not know precisely what determines the onset of the fatigue process. Once the fatigue process starts we are not able to evaluate its growth. Because of those knowledge gaps, we are currently exploiting only a portion of the potential of CFRP.

1.1 Damage tolerant design in aviation; a lesson learned from accidents

Lightweight structure design aims at minimizing weight while ensuring safety. Unfortunately, in the course of aviation history, safety was not ensured on various occasions and structural failure has led to many accidents. In the Comet crashes of 1954, cracks initiated at riveted holes propagated due to the cyclic pressurization of the fuselage and caused the explosion of the cabin. The following investigation concluded that 'by pressurizing the fuselage during the certification test up to twice the expected pressure, the fatigue life of the structure had been enhanced' [1]. In this way the test overestimated the fatigue life of the structure. At the time, designers were not aware of the retardation effect of tensile overloads in metal fatigue crack growth. In the subsequent years, through the expansion of fundamental knowledge regarding fracture mechanics and fatigue, the potential for unintended effects resulting from flawed assumptions, such as those that led to the accidents in 1954, was diminished. *However, could we exclude that unexpected cracks or damage would ever cause any other accidents?* It was clear at the time that aircraft operate in various conditions, with random sources of damage.

Considering this, the certification authorities progressively realized that more than focusing on a particular aspect of the design, a global change of philosophy was needed. Until then, structures were designed following the safe-life principle, meaning that components were required to exhibit a fatigue life exceeding the operational life of the aircraft. This approach didn't consider the occurrence of unpredicted damage before the end of life. After the Comet accidents, a fail-safe approach was increasingly implemented to address unexpected flaws by using structural redundancy. The existence of multiple site damage however, meaning multiple cracks propagating simultaneously in different locations, made in many cases the structural redundancy ineffective. Going back to the Comet cases, and other fatigue accidents, there is one aspect particularly upsetting. If someone had inspected the fuselage of the aircraft before the last flight, there is a chance that the cracks would have been noticed, the airplane stopped and the crash would have been avoided.

In 1978 the safe-life and fail-safe approach were embedded and updated in the **damage tolerance** design [2] which, after being updated several times, is still the design philosophy in-use [3]. Damage tolerance is grounded on one fundamental concept: *since damage can and will occur, we assume that damage is already present during the first operation.* In the presence of damage, the structure must be able to operate until the damage is identified and a repair action is performed. Compared to the previous design philosophies, damage tolerance mandates periodic targeted inspections of the structural components. If correctly implemented, this design philosophy addresses the presence of manufacturing flaws, unexpected damage occurring during operations, or caused by unconventional loading conditions. As said, there are many sources of damage in aviation with different levels of severity and different probabilities of detection. In the presence of large-size and severe damage obvious to the flight crew during the operations, the structure is often required to withstand the continuation of the flight safely. Smaller and less detectable damage instead, is expected to go unnoticed for a large number of flights. During this period, the structure has to maintain the required strength regardless of the combined action of cyclic loading, corrosion, temperature, and any other detrimental effects.

1.2 Damage tolerance in CFRP; the relevance of fatigue after impact analysis

Composite materials have been increasingly used in the aviation industry over the past decades. The new generation Airbus A350 XWB is composed of 53% composite materials by weight [4], whereas the Boeing 787 Dreamliner consists of 50% composite materials by weight [5]. Among composite materials, carbon fiber-reinforced plastics (CFRP) are by far the most represented, thanks to their combination of high specific stiffness and strength.

CFRP at its core is a composition of carbon fibers and a polymeric matrix. The fibers provide tensile stiffness and strength along their longitudinal direction, while the matrix provides lateral support and is essential to transfer the loads between the fibers. Having a preferential direction of strength is both the biggest advantage and pitfall of CFRP. If unidirectional loading is applied aligned with fibers, the strength-to-weight ratio is outstanding. However, in case the load is not aligned with fibers, the material reacts poorly and is more likely to crack due to the brittleness of the matrix. Even in the case of layup of plies (Figure 1.1) exhibiting quasi-isotropic behavior along the composite plane, one big limitation persists: the composite material reacts poorly to out-of-plane loads.

In the case of impacts, due to the brittle nature of the polymeric matrix, the impact energy is dissipated through various fracture mechanisms originating inside the material [6]. In civil aviation, impacts can be caused by birds, uncontained engine failure, foreign objects on the runways, hail storms, tools accidentally dropped during maintenance, and more. Because of the frequency of occurrence, the structures exposed to impacts are the object of a careful impact damage tolerance evaluation. Due to the geometry of many exposed structures, like the case of panels, impacts tend to happen in the out of plane direction, which is also the weakest direction of the laminate, as explained previously.

The damage tolerant design of CFRP is regulated in the guidance published by the FAA as Advisory Circular (AC) 20-107B [7] and by EASA as Acceptable Means of Compliance (AMC) 20-29 [8]. In those documents, different strength requirements are assigned to different impact damage visibility (Figure 1.2). In the presence of obvious damage that is evident to the flight crew and requires immediate repair, the aircraft must conclude a continued safe flight. In case of impact damage that can be detected within a few flights from the occurrence, the structure is asked to carry the limit load. In the case of visible impact damage (VID), several flights can pass between the impact event and the detection of damage, while BVID may never be found. Damage tolerance philosophy as introduced in the previous section, requires that in case of undetected damage, the structure maintains the ultimate strength regardless of cyclic loading and other detrimental effects. However, it was shown that if in-plane cyclic compression is applied to impacted CFRP, fatigue failure has been reported at compressive loads lower than 70% of residual strength after impact [9, 10]. This phenomenon is similar to crack propagation in metal tensile fatigue which, after fatigue loading, fails at stresses lower than the initial residual strength. However, the specific case of compressive fatigue loads after impact are generally not critical in metals.

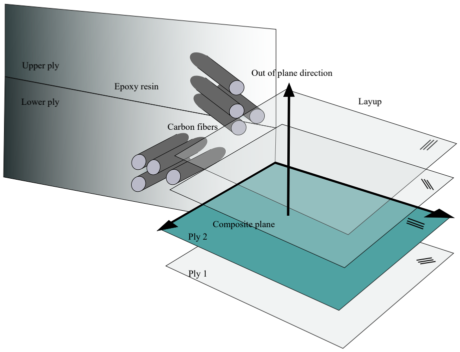

Figure 1.1: A simplified scheme of CFRP, showing plies having different fiber orientations stacked one on top of each other to form a layup

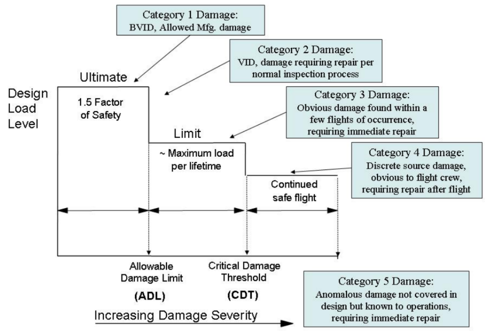

Figure 1.2: Damage tolerance guidelines for CFRP dictated by the EASA [8] the FAA [7]

The compression after impact fatigue analysis, once of little relevance in the context of metals, assumes paramount significance in the damage tolerance analysis of CFRP aeronautical structures for three main reasons:

- impacts are frequent in aviation;
- impact damage in CFRP develops internally and is difficult to detect;
- impacted CFRP fails under cyclic compressive load lower than residual strength.

Having asserted the relevance of fatigue after impact assessments for aeronautical damage tolerance design, the following sections describe the classification of impact events and the features of impact damage in detail. Subsequently, a review of experimental works concerning fatigue after impact is presented to highlight the most relevant knowledge gaps.

1.3 Impact events classification

An impact entails the transfer of energy between an impacting object and an impacted object. In solid media, impact energy is transmitted by stress waves that propagate from the impact contact point. The impact duration is related to the time it takes for the energy to be transferred from the impacting object to the impacted object. Generally, shorter impact durations tend to produce higher-frequency components in the stress waves, while longer durations result in lower-frequency components. The work by Olsson [11] showed that, in the case of impact on plates, it is the ratio between the impactor and the impacted plate masses that primarily determines the impact time and, consequently, the dynamics of the plate response.

Based on this consideration, three main categories of dynamic responses can be identified based on the impactor-plate mass ratio (Figure 1.3):

1. Small impactor/plate mass ratio: The impact duration is very short, and the response is dominated by dilatational waves. In this case, the plate's response depends on local properties at the contact point and has little dependency on the boundary conditions or overall bending rigidity.

2. Medium impactor/plate mass ratio: This case is characterized by a medium response time and is dominated by flexural and shear waves.

3. High impactor/plate mass ratio: Long impact time, the response is in the quasi-static regime. Increasing the impact duration, the dependency on the boundary conditions and overall bending rigidity becomes more relevant.

The high local stresses generated during the plate response are the mechanisms responsible for the formation of impact damage in CFRP. Not surprisingly, different types of dynamic responses result in different impact damage morphology. In the experiments by Olsson [11], the same impact kinetic energy was obtained using a high impactor/plate mass ratio at low velocity and a smaller impactor/plate mass ratio at higher velocity. The results showed a largely different damage severity, proving that even with the same impact energy, different elastic responses result in different impact damage. The previous categorization is based on the mass ratios and derives from the study of impact dynamics. A second impact classification, devised to collect the relevant cases for aeronautics, was often used in the past. This classification is based on impact velocity:

1. ballistic impacts (> 100 m/s); usually projectile impacts

2. high-velocity impacts (HVI) (10-100 m/s); bird strikes, FOD during takeoff or landing

3. low-velocity impacts (LVI) (1-10 m/s); hail during ground operations, tool drop during maintenance.

The two classifications can be combined to identify some critical cases for damage tolerance analysis. For example, an LVI with a low impactor-plate mass ratio will hardly produce any damage. On the contrary, an HVI with a high impactor-plate mass ratio will result in obvious damage and structure perforation like in the case of a strike with heavy birds. An interesting case to be analyzed is the LVI happening with a high impactor/plate mass ratio (dynamic response of category 3). This is the case for example of a tool drop during maintenance. In this case, the plate responds quasi-statically and generates a small indentation which is hard to detect and a large internal damage. In the previous section, this condition was defined as BVID and its relevance for damage tolerance analysis was addressed. We must consider that BVID is a definition based on damage detectability only. While it is true that low-velocity impacts combined with a high mass ratio will most likely result in BVID, it cannot be said that all BVIDs are generated by low-velocity impacts. We could have for example a high-velocity impact producing a large superficial damage in an area difficult to inspect. Due to its low detectability, this type of damage could also be classified as BVID, even if its damage morphology is different.

Having made this remark the present work will focus on the much more frequent case of a low-velocity impact happening with a high impactor/plate mass ratio resulting in BVID. In the following section, the features of such damage will be discussed in detail.

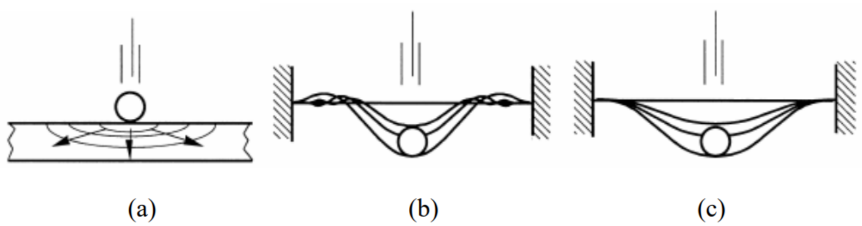

Figure 1.3: Impact response classification: a) short b) medium c) long impact time [11]

1.4 Barely visible impact damage topology

The topology of impact damage depends not only on the impact parameters (weight and velocity) but also on the impactor shape [12], on the laminate stacking sequence [13, 14], on the impacted plate thickness and constraint conditions [6]. Having recognized that multiple factors are involved, impact kinetic energy has been often used in experiments as a first impact damage severity indicator. If we impact a CFRP component with increasing kinetic energy but remain in the LVI-high mass ratio condition (section 1.3), we observe different damage modes originating at different energy levels [6].

At lower energy levels, the first noticeable damage is the **matrix cracking** within individual plies. Optical microscopy has been applied to sections of impacted specimens [15, 16] revealing two types of cracks: tensile matrix cracks and shear matrix cracks (figure 1.4a). Tensile matrix cracks are formed close to the back face of the specimen due to the bending deformation of the plate and they are characterized by a 90° angle with respect to the in-plane direction. Shear matrix cracks instead are mainly formed due to the out-of-plane shear stress and they are generally characterized by a 45° angle with respect to the in-plane direction. Shear stresses arise inside the laminate because of the combined effect of contact stress, and mismatch of bending stiffness between the different plies. In every ply, matrix cracks form preferentially in the two maximum shear regions symmetrical to the impact contact point [17].

Starting from intra-ply matrix crack tips, fracture propagates in the in-plane direction along the resin-rich regions which are present in the interface between different plies forming **delamination**. According to experimental evidence, more than kinetic energy levels, the onset of delamination can be linked to a threshold peak reaction force measured in the composite plate [18]. In the early ‘90s, it was observed that delamination propagates preferentially from the tips of existing transverse tensile and shear matrix cracks [19] (Figure 1.4.c). Starting from these locations, delamination propagates mostly under mode II opening caused by the mismatching bending stiffness of adjacent plies [13]. This explains why mode II fracture toughness is the material property most affecting the areal extension of impact delamination [20]. Early experimental works suggested that delamination assumes a “peanut” shape bounded by the upper and lower ply orientation [6]. More recently however, thanks to the combined use of ultrasound C-scans and X-ray CT scans, it was possible to construct a more precise image of a "typical" impact delamination shape, which appears to be more similar to a double triangular shape in case of a 45-degree mismatch angle between adjacent plies [21, 22].

To summarize, for a given interface, delamination originates from existing matrix cracks in the upper ply and then propagates in the direction of the lower ply fiber orientation [14] (Figure 1.4), where the upper ply is the one closer to the impacted face. The described damage mechanism well agrees with side microscopic images and C-scans that are present in literature [21] and was observed in quasi-static indentation tests as well [23]. It is not surprising that to correctly estimate delamination shape in impact simulations, the interaction between matrix cracks and delamination needs to be included in models [24, 25]. Delaminations having the described features, tend to form in every interface between plies with mismatching orientations, creating a complex tridimensional damage shape (Figure 1.4). If the impact kinetic energy is increased, a roughly linear increase of the projected delaminated area can be observed [6] until the appearance of a new damage mode.

A feature that was sometimes observed in BVID, is the presence of a non-delaminated cone exactly below the impact contact area [21]. The presence of this cone can be explained by considering the contact out-of-plane compression stress originating during the impact. This stress state has the effect of reducing the opening displacement of delaminations in the central area.

If impact energy is further increased, **fiber failures** start to happen close to the impact location and near the back face due to contact and tensile stresses and within plies as a consequence of interlaminar shear stress. [6]. Figure 1.4 illustrates the structure of a BVID which is formed in a thick plate composed of a quasi-isotropic layup of unidirectional CFRP plies, with a constant mismatch angle of 45 degrees.

1

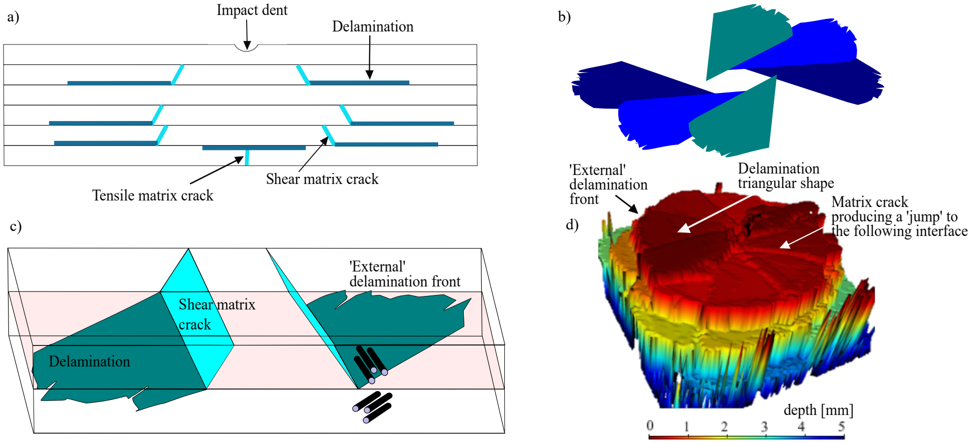

Figure 1.4: BVID in a quasi-isotropic laminate with 45deg angle mismatch between plies a) side view representation b) representation of delaminations (top view) in different interfaces showing the double-triangular shape c) representation of a single interface between two plies showing delamination originating from shear matrix crack d) ultrasound scan of actual impact damage showing the 3d delamination envelope

1.5 Fatigue after impact; critical review of past experiments and major knowledge gaps

The comprehension of BVID fatigue remains limited; we still don't know what happens in the initial stages of fatigue and we have not precisely described fatigue damage propagation. Before discussing the knowledge that is still missing, let's start with some known facts.

It has been determined that impact damage in CFRPs can propagate under in-plane tension fatigue [26], compression fatigue [27], tension/compression fatigue [28] and shear fatigue [29]. Among these loading conditions, compressive cycles have a larger influence on the degradation of strength [28]. Compressive loading presents the additional challenge of instabilities affecting single plies (fiber kinking) and interfaces (sub-laminates buckling). For those reasons, most of the research efforts have been directed towards compressive cyclic loading [30].

Uda et al.'s [31] experimental campaign showed that SN curves of epoxy CFRPs with various initial impact damage sizes tend to converge into a single curve when the following normalization is applied:

$$\frac{\sigma_{max}}{\sigma_{ult(CAI)}} \tag{1.1}$$

In the equation, σ_{max} refers to the maximum compression load in the fatigue cycle, while $\sigma_{ult(CAI)}$ refers to the residual compressive static strength after impact evaluated experimentally. To explain why this normalization produces a collapse of the S-N curves, we need to consider BVID as a notch internal to the material. Thanks to Griffith's contribution

[32], we understand that a similar stress state at the notch tips can be achieved by either enlarging the crack or increasing the applied stress. In the context of impact damage, local stress states at the crack fronts can similarly increase with higher applied stress or larger impact damage. The normalization of the maximum stress applied in fatigue tests by the residual CAI strength implies a comparison of the fatigue life of cracks under similar local stress states, given that residual strength depends on the impact damage size. Therefore, the normalization of applied stress by residual strength is widely adopted in the literature. While this procedure allows for the comparison of fatigue life in different impact damage sizes, certain challenges arise. Firstly, the compression after impact strength value is either statistically derived from other specimens impacted under similar (but never identical) conditions or calculated using models attempting to estimate residual strength from impact damage. In both cases, an exact value for the residual strength is not available. Even if we could derive the real residual strength, it remains unclear whether static failure and fatigue propagation involve the same processes. It is possible that a more suitable similitude parameter could be found in damage geometry if the stress states are described. However, this necessitates an understanding of impact damage and fatigue after impact which is currently unavailable.

Many experiments have identified a fatigue limit at 60% of the residual CSAI [9, 10]. Below this threshold, no significant degradation in residual strength was observed. Mitrovic et al. [9] examined the effect of variable amplitude loading and found that High-Low loading cycles are more detrimental than Low-High cycles. Interestingly they observed fatigue degradation at stresses lower than the fatigue limit (60% of CSAI) if high load cycles were applied before. To explain this observation, the authors suggested that the energy required to initiate the fatigue process may be higher than the energy required to sustain the subsequent propagation. The concept of initiation in fatigue after impact may seem counter-intuitive. In pristine CFRP material, the fatigue initiation phase usually consists of matrix micro-cracks which are formed and gradually merge into larger-scale damage structures. In fatigue after impact cases instead, the starting point is a largely damaged structure containing delamination and ply matrix cracks, all with sharp notches. The concept of fatigue after impact damage initiation, however, assumes significance if we consider that impact and compression after impact are different stress states. The local stress states at the crack fronts under in-plane loading are different from the ones of out-of-plane impact. It is plausible that a process of initiation takes place in the impact damage as a consequence of the change in loading conditions and that this phenomenon requires additional energy. Another consideration regarding Mitrovic's results is that during the initial overload, it's possible that the impact damage grew, leading to a decrease in residual strength. Consequently, in the subsequent low-load cycles, the effective applied stress could be higher than 60% of CSAI, as a smaller CSAI now normalized the same stress.

Once the fatigue process begins, understanding the involved phenomena and the causes of strength loss is crucial. In most of the previous research, delamination propagation has been appointed as the process responsible for mechanical properties degradation. This attribution was mainly due to failed specimens often presenting signs of unstable sublaminate buckling. Melin et al. [28, 33] compared buckle areal extension with the delaminated area close to the surface of impacted specimens. As the delamination was propagating, the buckled area was observed to overlap with the delamination area and increase at the same rate. This confirmed that there is a relationship in fatigue between the buckling of sublaminates and delamination growth during compression cycling loading. Delamination can be monitored via non-destructive ultrasound inspection (C-scan). C-scan systems work by the attenuation (through-thickness scan) or reflection (pulse-echo scan) of ultrasound waves that travel inside a material and encounter a free surface. A common experimental practice followed in past research involved monitoring delamination using ultrasound inspection at different stages of compression fatigue after impact fatigue (CFAI) to track and describe its growth throughout the fatigue life. Following this practice, one test [34], reported a phase in which no fatigue growth happened outside of the impact delamination projected area followed by the fast and unstable growth of a single delamination. In another experiment [27] no delamination growth was observed in inspections until the failure of the specimen, which still started from the impact damage location. In two tests [35, 36], the initial growth of delamination width was observed, followed by a phase of no apparent growth leading to a third phase of fast and unstable growth that led to failure. In other experiments then, the gradual growth of delamination outside the damaged envelope was observed from the beginning of fatigue life [9, 10]. All the cited tests were conducted on coupons made of quasi-isotropic layups of unidirectional CFRP containing BVID and loaded under cyclic compression. Regarding this discrepancy between observations, Pascoe [37] hypothesized that the phases of no delamination growth that were sometimes observed could be in part attributed to the ultrasonic shadowing effect. Because of this phenomenon, it is not possible using a C-scan to observe any delamination that is positioned in a central depth between larger delaminations. BVID is composed of multiple delaminations situated in different interfaces, some of them shadowed and not visible from the C-scan. It is then possible that, in the portion of fatigue life defined as no-growth phases by previous experiments, delamination was propagating undetected by the C-scan, in the form of growth of shadowed delamination. A second aspect neglected in previous experimental fatigue studies regards delamination growth inside the non-delaminated impact cone. It was observed that below the impact dent, impact damage presents an area with less or no delamination, caused by the out-of-plane compression contact stress (section 1.4). In their CAI test campaign, Bull et al. [21] compared the computed tomography (CT) scans of impacted specimens with the CT scans of impacted specimens loaded in compression to a near-failure load. The loaded specimens showed a growth of delamination below the impact cone, with little delamination growth outside of the external damage area. This observation was performed in a static test, however, it is reasonable to assume that a similar phenomenon may occur in fatigue. Unfortunately, the same investigation was not replicated in fatigue, probably due to the difficulty in performing CT scans in situ during fatigue tests. Additionally, it is hard to observe this phenomenon using ultrasound scans due to the reflection caused by the impact dent's curved surface. It could be that, while no growth was observed in previous tests, some growth of delamination occurred inside the non-delaminated cone.

From a more fundamental point of view, the different results between available tests could be attributed to an applied stress effect. In the experiment by Tuo et al. [36], different maximum compressive loads applied to BVID evidenced a significant difference between low-cycle and high-cycle fatigue. In long-life fatigue (62% CSAI), delamination grew slowly before the onset of faster growth. In short-life fatigue (77% of CSAI), a gradual growth occupying all fatigue life was observed. In all tests in the literature, stress was defined as a fraction of residual strength, and the limitations of this approach have been previously discussed. Residual strength is calculated in different ways among the tests and the impact damage shape varies among the different experiments. Even if in two tests the same fraction of residual CSAI is applied, local areas of the impact damage could experience largely different stress states. For this reason, some of the discrepancies between tests could be attributed to a different stress state of the cracks.

Finally, delamination is not the only damage mode present in impact damage. BVID is also composed of intra-laminar matrix cracks and fiber-marix debonding inside the plies which cannot be detected using a C-scan. These stress singularities are usually not considered, but they can potentially propagate under fatigue. In conclusion, there are two big knowledge gaps to be solved:

- It is unclear what determines the onset of the fatigue process
- Once fatigue damage growth starts, it is unclear how to measure its state

The following section highlights the significance of these knowledge gaps in the context of aeronautical design. It will explain how this lack of understanding represents a limiting factor in the damage-tolerant design of CFRP lightweight structures.

1.6 The 'no growth' concept; fatigue after impact as a limiting factor in CFRP design

Despite the limited understanding of fatigue after impact, aircraft manufacturers and airworthiness regulators managed to provide damage-tolerant design guidelines for CFRP. The **no-growth** approach was introduced for this purpose. The following section explains why this is necessary, by comparing fatigue after impact in CFRP to the simpler case of fatigue of cracks in metallic components.

In the case of a fatigue crack growing in a metallic part, assuming that the part can be inspected visually, a sequence of steps is followed to produce a damage-tolerant design:

1. *Assume an initial damage state;* we can consider this as a minimum crack size. This assumption constitutes the starting point for the DT analysis and is usually done based on knowledge of possible sources of damage and defects.
2. *Establish a critical damage state;* we can consider this as a maximum crack size after which it becomes unsafe to fly. Determining this damage state equals establishing at which crack length the residual strength equals the prescribed strength.
3. *Calculate the growth rate;* we now have a minimum and maximum length for the crack, but how many load cycles will it take to reach the critical damage state? In this stage, the designer has to prove with fracture mechanics calculations and tests that fatigue cracks will exhibit slow, stable, and predictable growth. This evaluation should consider the loading and environmental conditions expected in service.

4. *Provide an inspection window;* having determined minimum length, maximum length, and growth rate, an interval between inspections is provided, considering that multiple chances for detection must occur before reaching the critical state.

The described approach is called 'slow growth' since, in the interval between inspections, fatigue cracks are allowed to grow as long as the growth is 'slow' and there is sufficient room to detect them before they become critical. A visual representation of how the slow growth principle works is given in Figure 1.5.

In the previous sections, the state of the art of impact damage characterization and fatigue after impact has been introduced. If we now try to set up a slow growth procedure for the case of fatigue after impact in CFRP, a series of issues emerge. The first problem concerns damage detectability. BVID, by definition, has a high probability of misdetection. Additionally, BVID fatigue growth occurs internally without increasing the visibility of damage. If we cannot ensure that damage will be detected with a certain level of confidence, we cannot establish the slow growth procedure. Even if systematic ultrasound inspection is performed, and we have sufficient confidence that the damage is detected, additional problems arise. To apply slow growth, airworthiness authorities require evidence of fatigue growth, which should be slow, stable, and predictable from the outset until reaching the critical damage size [7, 8]. However, as explained in the previous section, ultrasound monitoring in compression after impact fatigue tests revealed delamination growth that was often fast and unstable. A third problem concerns the difficulty in identifying the critical damage state. In the tests by Ogasawara [27], no delamination growth was observed in ultrasound inspections until the final failure. In such cases, it is not possible to define a critical damage state if the impact damage appears the same in inspections at both the beginning and end of fatigue life. To state this more fundamentally, it is not sure how the concept of growth, intended as dimensional growth of damage, should be related to strength degradation. In CFRP, we often observe damage modes, like fiber kinking, which produce a little increase in the damage area but have a large effect on the residual stiffness and strength of the structure. *What is lacking is a definition for damage growth or propagation.*

The no-growth approach has been introduced specifically to overcome these kinds of issues. In opposition to slow growth, in the no growth procedure damage is not allowed to grow and produce strength degradation in the interval between inspections. The advantage is that to certify the no growth behavior, manufacturers don't need to provide specific explanations of what will happen in case of fatigue growth. They instead show from testing that the strength of the impacted component will not degrade in operations for a prescribed number of cycles (i.e. the inspection window). The inspection window varies among different impact damage visibility. In the case of a BVID, which has a high chance of misdetection, the inspection window coincides with the full life of the aircraft; hence, there is an ultimate load capability requirement. With more visible damage, the structure is allowed to have an excursion below the ultimate load as long as the damage can be identified in short time. However, in both cases, the residual strength over fatigue cycles remains constant between inspections, in opposition to the slow growth approach (Figure 1.6). From a practical point of view, no growth is achieved by increasing the thickness of the component, with a weight penalty. This is because we lower the stress to the point that the structure always operates below the compression after impact fatigue limit. This represents a limiting factor in the design of many CFRP components of the aircraft exposed

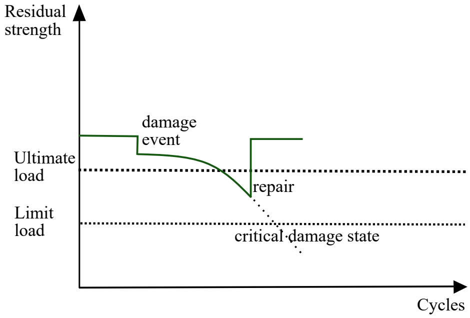

Figure 1.5: Slow growth procedure

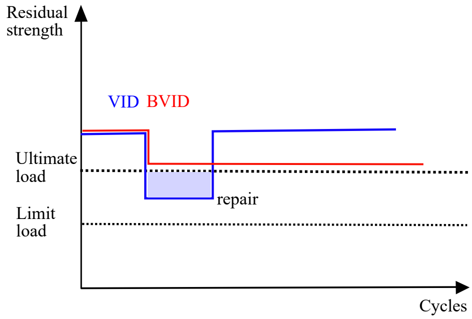

Figure 1.6: No growth procedure for BVID and VID

to impacts.

To summarize, the limitations in the detectability of impact damage, along with the fast and unstable growth behavior observed in fatigue delamination, have led to the introduction of no-growth certification. It must be considered, however, that the current description of the fatigue after impact growth has limitations. Ultrasound inspections can only detect non-shadowed delaminations and exclude many damage modes. An improved description of impact damage and a deeper understanding of the phenomenon of fatigue after impact may explain if there is potential for the application of a smarter certification approach like slow growth, as suggested by the work of Pascoe [37]. The understanding of the phenomena could lead also to a reduction in the number of tests required for certification (for example by efficiently individuating worst case scenarios). This thesis, as will be clarified in the following section, represents a step in providing this fundamental knowledge.

1

1.7 Aim and scope

The primary goal of this thesis is to conduct fundamental research on the phenomenon of CAI fatigue. In the previous sections, it was shown that despite several experiments being performed in the past, knowledge gaps persist in the description of fatigue after impact. These knowledge gaps primarily concern the initiation of fatigue and the characterization of fatigue growth in impacted CFRP material.

Considering this, the decision was made to investigate the following research question:

How can we describe fatigue after impact damage growth in CFRP?

This fundamental question is linked to several sub-questions:

- Which mechanisms are taking place during fatigue after impact damage propagation?
- How can we explain the discrepancies in previous experiments monitoring fatigue after impact damage growth?
- How well do the commonly performed tests represent fatigue after impact in a real structure?
- How generic are the propagation patterns concerning to different applied maximum compressive stress and initial impact damage configurations?

To investigate these questions, different experimental campaigns were conducted, applying various inspection and monitoring techniques. This experimental work was complemented with numerical modeling of simplified impact damage configurations. The following section summarizes the outlines of the thesis.

1.8 Outlines

Chapter 2 combines two types of ultrasound monitoring with digital image correlation to obtain an upgraded description of delamination growth in CFAI tests. Thanks to this observation, it is possible to explain some of the discrepancies observed in previous literature.

In Chapter 3, surrogate impact damage is created using PTFE inserts. Thanks to this surrogate impact damage condition, fatigue propagation of multiple delaminations is monitored, and a comparative study is conducted with CAI fatigue.

In Chapter 4, a numerical model is developed to evaluate the strain energy release rate along multiple delamination fronts. A parametric study is then conducted to explain some pattern observed in delamination growth. Effects of the fixture and initial damage configuration are also studied.

The following chapters adopt acoustic emissions as an additional tool to be combined with ultrasound in the CFAI tests monitoring. Chapter 5 presents preliminary tests that were set up to isolate waveforms deriving from specific damage modes. Strategies to separate acoustic signals originating from different sources and the limitations of the various techniques are also discussed.

Chapter 6 performs a damage accumulation study in quasi-static CAI tests using acoustic emissions to show how different damage mechanisms act at different stress levels in the load range compatible with fatigue load.

In Chapter 7, a novel strategy for damage mode separation via wavelet transform and convolutional neural networks is developed. Using this method, a damage mode repartition study in fatigue after impact tests is performed. The activation of different damage modes at different load levels and in different phases of fatigue life are discussed.

In Chapter 8, the main conclusions and recommendations for future research are presented. Recommendations for CAI fatigue monitoring are also discussed in this chapter.

1

References

[1] Federal Aviation Administration. De havilland dh-106 comet 1 lessons learned. https://www.faa.gov/lessons_learned/transport_airplane/accidents/G-ALYV.

[2] Federal Aviation Administration. Damage tolerance and fatigue evaluation of structure. Advisory circular 25.571-1, 1978.

[3] Federal Aviation Administration. Damage tolerance and fatigue evaluation of structure. Advisory circular 25.571-1D, 2011.

[4] Federal Aviation Administration. Flight airworthiness support technology,airbus technical magazine. Technical report, Airbus, June 2013.

[5] Boeing. 787 dreamliner by design. Accessed on 28-03-2024.

[6] Serge Abrate. Impact on laminated composite materials. *Applied Mechanics Reviews*, 44:155–190, 1991.

[7] Federal Aviation Administration. Composite aircraft structure. Advisory circular 20-107B, 2010.

[8] European Union Aviation Safety Agency. Annex ii - amc 20-29 to ed decision 2010/003/r. Technical report, 2010.

[9] Milan Mitrovic, H. Thomas Hahn, Greg P. Carman, and Peter Shyprykevich. Effect of loading parameters on the fatigue behavior of impact damaged composite laminates. *Composites Science and Technology*, 59:2059–2078, 1999.

[10] G. Clark and T. J. Van Blaricum. Load spectrum modification effects on fatigue of impact-damaged carbon fibre composite coupons. *Composites*, 18:243–251, 1987.

[11] R. Olsson. Mass criterion for wave controlled impact response of composite plates. *Composites Part A: Applied Science and Manufacturing*, 31:879–887, 2000.

[12] T. Mitrevski, I. H. Marshall, and R. Thomson. The influence of impactor shape on the damage to composite laminates. *Composite Structures*, 76:116–122, 2006.

[13] Dahsin Liu. Impact-induced delamination – a view of bending stiffness mismatching. *Journal of COMPOSITE MATERIALS*, 22:674–692, 1988.

[14] G. Clark. Modelling of impact damage in composite laminates. *Composites*, 20:209–214, 1989.

[15] Smith B.T. Hinkley J.A. Srinivasan K., Jackson W.C. Characterization of damage modes in impacted thermoset and thermoplastic composites. *Journal of Reinforced Plastic and Composites, vol 11*, 1992.

[16] J.C.Weidner W.J.Murri D.J.Boll, W.D.Bascom. A microscopy study of impact damage of epoxy-matrix carbon-fibre composites. *Journal of Materials Science*, 21:2667–2677, 1986.

[17] Lorenzo Mencattelli and Silvestre T. Pinho. Realising bio-inspired impact damage-tolerant thin-ply cfrp bouligand structures via promoting diffused sub-critical helicoidal damage. *Composites Science and Technology*, 182:107684, 2019.

[18] G A Schoeppner and S Abrate. Delamination threshold loads for low velocity impact on composite laminates. 31:903–915, 2000.

[19] Derek Hull and Yi Bing Shi. Damage mechanism characterization in composite damage tolerance investigations. *Composite Structures*, 23:99–120, 1993.

[20] Alan Tate Nettles and Luke Scharber. The influence of gi and gii on the compression after impact strength of carbon fiber/epoxy laminates. *Journal of Composite Materials*, 52:991–1003, 2018.

[21] D. J. Bull, S. M. Spearing, and I. Sinclair. Observations of damage development from compression-after-impact experiments using ex situ micro-focus computed tomography. *Composites Science and Technology*, 97:106–114, 2014.

[22] Andrey Chernov Alexander Shanygin Egor Morokov, Vadim Levin. High resolution ply-by-ply ultrasound imaging of impact damage in thick cfrp laminates by high-frequency acoustic microscopy. *Composite Structures*, 256:113102, 2021.

[23] Robin Olsson Peter Hellström Spyros Tsampas Mark Pankow Mark McElroy, Wade Jackson. Interaction of delaminations and matrix cracks in a cfrp plate, part 1: A test method for model validation. *Composites Part A: Applied Science and Manufacturing*, 103:314–326, 2017.

[24] Christophe Bouvet, Bruno Castanié, Matthieu Bizeul, and Jean Jacques Barrau. Low velocity impact modelling in laminate composite panels with discrete interface elements. *International Journal of Solids and Structures*, 46:2809–2821, 2009.

[25] XC Sun and SR Hallett. Barely visible impact damage in scaled composite laminates: Experiments and numerical simulations. *International Journal of Impact Engineering*, 109:178–195, 2017.

[26] Raffael Bogenfeld, Patrik Schmiedel, Naren Kuruvadi, Tobias Wille, and Janko Kreikemeier. An experimental study of the damage growth in composite laminates under tension–fatigue after impact. *Composites Science and Technology*, 191:108082, 2020.

[27] Toshio Ogasawara, Sunao Sugimoto, Hisaya Katoh, and Takashi Ishikawa. Fatigue behavior and lifetime distribution of impact-damaged carbon fiber/toughened epoxy composites under compressive loading. *Advanced Composite Materials*, 22:65–78, 2013.

[28] L. G. Melin, J. Schön, and T. Nyman. Fatigue testing and buckling characteristics of impacted composite specimens. *International Journal of Fatigue*, 24:263–272, 2002.

[29] Yu Feng, Yuting He, Xiangfei Tan, Tao An, and Jie Zheng. Investigation on impact damage evolution under fatigue load and shear-after-impact-fatigue (saif) behaviors of stiffened composite panels. *International Journal of Fatigue*, 100:308–321, 2017.

[30] Glyn Davies and Philip Irving. *Impact, post-impact strength, and post-impact fatigue behavior of polymer composites.* Elsevier Ltd, 2020.

[31] Nobuhide Uda, Kousei Ono, and Kazuo Kunoo. Compression fatigue failure of cfrp laminates with impact damage. *Composites Science and Technology*, 69:2308–2314, 2009.

[32] Alan Arnold Griffith. Vi. the phenomena of rupture and flow in solids. *Philosophical transactions of the royal society of london. Series A, containing papers of a mathematical or physical character*, 221(582-593):163–198, 1921.

[33] L. Gunnar Melin and Joakim Schön. Buckling behaviour and delamination growth in impacted composite specimens under fatigue load: An experimental study. *Composites Science and Technology*, 61:1841–1852, 2001.

[34] Fan Xu, Wenli Liu, and Phil E. Irving. Fatigue life and failure of impact-damaged carbon fibre composites under compressive cyclic loads. *ICCM International Conferences on Composite Materials*, 2017-Augus:20–25, 2017.

[35] A. S. Chen, D. P. Almond, and B. Harris. Impact damage growth in composites under fatigue conditions monitored by acoustography. *International Journal of Fatigue*, 24:257–261, 2002.

[36] Hongliang Tuo, Tao Wu, Zhixian Lu, and Xiaoping Ma. Evaluation of damage evolution of impacted composite laminates under fatigue loadings by infrared thermography and ultrasonic methods. *Polymer Testing*, 93, 1 2021.

[37] John-Alan Pascoe. Slow-growth damage tolerance for fatigue after impact in FRP composites: Why current research won't get us there. *Theoretical and Applied Fracture Mechanics*, 116:103127, 2021.

2

The fatigue after impact delamination growth phenomenon

The common practice of adopting the delamination envelope projected area or width as a metric to describe fatigue growth leads to misinterpretation of results. Experiments conducted as part of this thesis showed that while no growth was happening outside of the projected area, preferential growth of shorter delaminations and delamination growth in the non-delaminated cone were observed. These phenomena however do not exclude the presence of a plateau phase in fatigue delamination growth and they explain only partially the discrepancy in previous literature. Results of this chapter have been previously published in a journal paper [1] and a conference paper [2].

2

2.1 Characterization of delamination growth

Delamination growth is the most noticeable damage propagation phenomenon in compression fatigue after impact. Because it enables the buckling of sublaminates, it can be directly related to compressive strength loss. In the present chapter, a choice was made to investigate and describe impact delamination fatigue growth as a starting point. It should be considered however that other damage modes like intralaminar matrix cracking and fiber failures are likely to act in fatigue after impact. These damage modes could concur in the formation and growth of delamination hence should be integrated in the discussion. This aspect will be discussed in chapter 7 of this thesis where acoustic emissions are used to investigate other damage modes present in CAI fatigue.

As anticipated in the introduction, several experimental studies have provided a description of delamination growth using delamination width or projected area. One test [3], reported a phase in which no fatigue growth happened outside of the impact delamination projected area followed by the fast and unstable growth of a single delamination. In another experiment [4], no delamination growth was observed in inspections until the failure of the specimen. In two tests [5, 6], an initial growth of delamination width was observed, followed by a phase of no apparent growth followed by a third phase of fast and unstable growth which led to failure. Finally, in other experiments, a growth of delamination outside the damaged envelope was observed from the beginning of fatigue life [7, 8]. In the introduction, in an attempt to explain these different behaviors, some hypotheses have been raised:

- Growth in the non-delaminated cone could happen before the growth of large delaminations.
- Short and shadowed delaminations could grow faster and before long delaminations in fatigue.
- The magnitude of the applied stress may dictate whether a delamination growth 'plateau' phase occurs. Elevated stress levels might lead to the absence of a plateau.

In this chapter, the results from a compression after-impact fatigue experiment are presented to test/refute each of these hypotheses. Delamination propagation was studied using a combination of ultrasound through thickness attenuation and pulse-echo scans. In addition to that, digital image correlation (DIC) analysis was used to match the observed delamination growth with the local buckling of the sublaminates. The chapter starts with a methodology section, continues with the results obtained with each inspection technique, and terminates with the general conclusions of the investigation.

2.2 Methodology

2.2.1 Specimen manufacturing

For the CAI fatigue tests, Toray M30SC Deltapreg DT120-200-36 UD, a commercial carbon fiber/epoxy prepreg, was laid up in $[-45, 0, 45, 90]_{4,S}$ orientation. The plies of prepreg were laid up manually in a clean room. Debulking was conducted after the positioning of every four plies to minimize air inclusions at interfaces. The obtained laminate was laid on an aluminum plate, with Marbocote 220 releasing agent, and sealed with a vacuum bag.

The curing process was conducted in an autoclave (figure 2.1a) using the manufacturer's recommended procedure, with a maximum pressure of 6 bar and a curing temperature of 120°C. The bag was kept in vacuum conditions during the entire curing cycle. The curing cycle in the autoclave was applied to large plates (400 × 600 mm) which then were cut into smaller rectangles (figure 2.1c) using a circular diamond blade (figure 2.1b). The final specimens had nominal dimensions of 150 × 100 × 5.15 mm, as specified in the ASTM D7136 standard. Using this methodology, a total of six specimens were manufactured. Table 2.1 shows the properties of a unidirectional laminate after the curing procedure. The laminate properties provided by the manufacturer along a 0-degree direction are an elastic modulus of 145 GPa, unidirectional strengths of 3010 MPa (tensile), and 1020 MPa (compressive). The static fracture toughness in mode I, obtained with standard DCB tests is $611 J/m^2$ [9].

Table 2.1: Unidirectional laminate mechanical properties as provided by the manufacturer

Property	**Test Standard**	**Value**
Tensile Strength (0°)	ASTM D 3039	3010 MPa
Tensile Modulus (0°)	ASTM D 3039	145.0 GPa
Tensile Strength (90°)	ASTM D 3039	39 MPa
Tensile Modulus (90°)	ASTM D 3039	6.4 GPa
Compression Strength (0°)	ASTM D 6641	1020 MPa
Compression Modulus (0°)	ASTM D 6641	133.0 GPa
Compression Strength (90°)	ASTM D 6641	138.0 MPa
Compression Modulus (90°)	ASTM D 6641	8.1 GPa
In-Plane Shear Strength	EN 6031	95.6 MPa
In-Plane Shear Modulus	EN 6031	3.38 GPa
ILSS	EN 2563	77.2 MPa

2.2.2 LVI tests

Impact testing was carried out in accordance with ASTM D7136 [10] using a drop-weight tower, as shown in figure 2.2. The support fixture had a cut-out with dimensions of 125 ± 1 mm in the length direction and 75 ± 1 mm in the width direction. To ensure single impacts, the impact tower was equipped with a catcher activated by optical sensors. A hemispherical impactor with a diameter of 16 mm and a mass of 4.8 kg was utilized. Following ASTM D7136's recommendation of 6.7 J per mm of laminate thickness, a target impact energy of 34 J was employed in the impacts. The impactor was not equipped with a load-displacement measurement system, hence the effective impact energy is not provided.

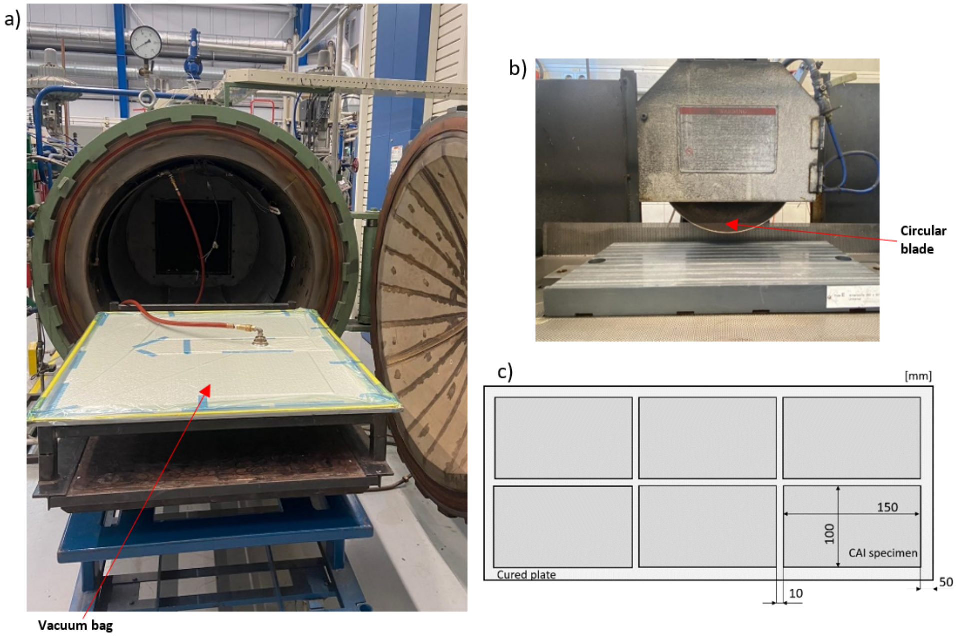

Figure 2.1: Images from the manufacturing of the laminate showing a) the autoclave and the vacuum bag containing CFRP plates, b) the diamond saw used to cut the specimens, c) the scheme of the cuts.

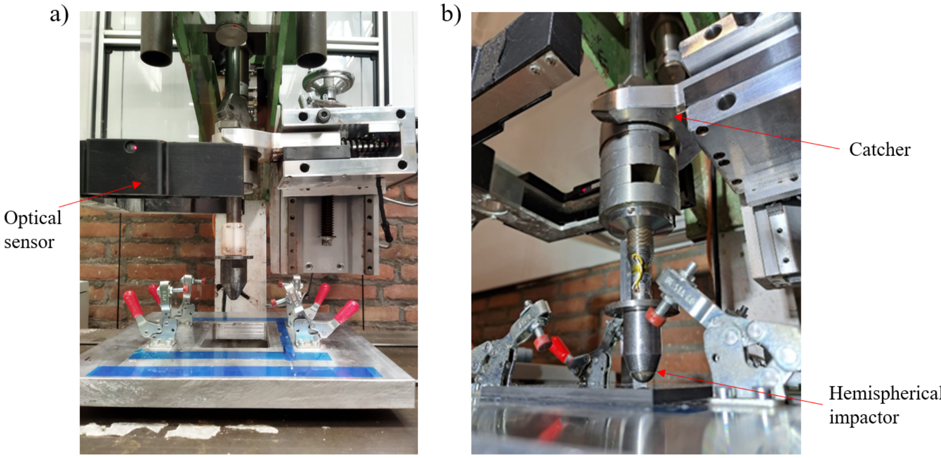

Figure 2.2: Fixture of LVI test showing the hemispherical impactor, the catcher to avoid bounce back triggered by optical sensor

2.2.3 CAI fatigue tests

As there is no standardized method for fatigue CAI testing, the same setup as that normally used for static CAI testing ASTM D7137 [11] was employed in the fatigue tests (figure 2.3). In contrast with the standard fixture, the lateral anti-buckling guides had a flat contact instead of a knife edge. Different specimens were tested at various compression load levels to obtain short-life fatigue and long-life fatigue tests. The results of CAI quasi-static tests (presented in Chapter 6 of this thesis) were used to estimate the residual strength after the impact. Fatigue load levels were then defined as % of CAI residual strength. The main limitation of this approach, explained in the introduction, is that we don't posses the compression after impact strength value of the specific specimen we are going to test in fatigue. Then it is unclear whether static failure and fatigue propagation involve the same processes. Comparing two different tests with a similar applied % of CSAI could result in largely different local stress inside the impact damage. This limitation has to be kept in mind when comparing the present results with others in the literature. Despite the limitations of this approach, it was adopted to provide an initial estimation of the maximum compression load in fatigue to achieve a long and short fatigue life.

Load levels between 70% and 80% of the residual CAI strength were applied in the test. A constant R ratio (R = 10) was kept and, to prevent self-heating of the specimens, a constant frequency of 3 Hz was adopted. The tests were conducted using an MTS hydraulic testing machine equipped with a 250kN load cell (specimens s1, s2) and 100 kN load cell (specimens s3, s4, s5). During the tests, the applied force and the crosshead displacement were recorded.

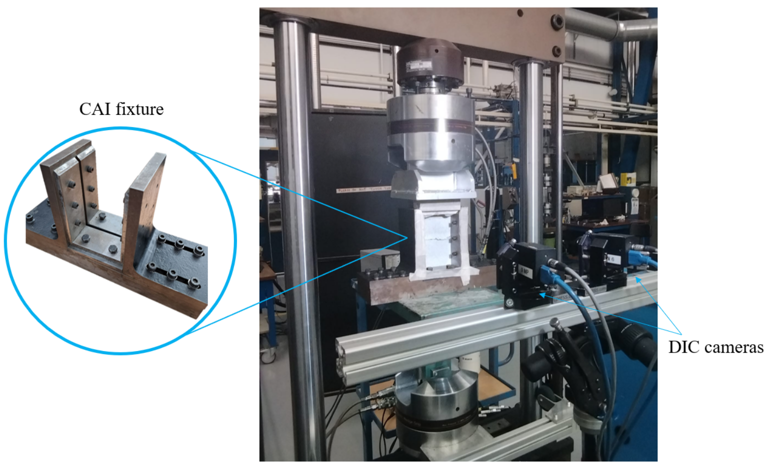

Figure 2.3: CAI fixture with DIC cameras

2.2.4 Digital image correlation

To evaluate the surface displacement and interpolate the surface engineering strains, a three-dimensional digital image correlation (DIC) system was used. Digital Image Correlation (DIC) is a non-contact, optical technique used to measure displacements on the surface of structures, through the analysis of digital images. DIC systems typically involve multiple cameras and specialized software for image analysis. The software tracks patterns or markers on the structure's surface from one image to the next and calculates displacement and deformation information. The speckle pattern on the surface of the specimen was obtained by first spraying a uniform layer of flat white paint on the surface of the specimen. After the first layer dried, black paint with low reflection was sprayed to achieve a black-and-white speckle pattern. The flow of the spray was manually adjusted to achieve the required size and density of speckles. The system adopted in the current experiment consisted of two nine MP "Point Grey" cameras (figure 2.3) with 'Tamron' 25 mm lenses. The speckle pattern images were captured by ViC-Gauge 3D software with an acquisition rate of one frame per second (fps). To obtain a steady picture of the buckled sublaminate, fatigue tests were periodically interrupted and a displacement of 80% of maximum compression was held for 2 seconds. Afterward, the images were processed using 'ViC-3D 8' software to perform a strain analysis.

2.2.5 Ultrasound scan

To assess the size of delaminations, two ultrasound systems were utilized. The first system was a water-tank immersion system operating in through-transmission attenuation mode (figure 2.4.b). This system uses a 5 MHz ultrasound frequency, with a distance of 100 mm between the emitter and receiver. The scanning speed was set at 100 mm/s, resulting in a resolution of 1 mm. The water tank was located near the testing machine, hence the periodical operation of removing the specimen from the fixture, performing the inspection, and replacing the specimen to restart the test took approximately 15 minutes for each inspection. The second system adopted was the pulse-echo Dolphicam 2 system, equipped with a scanning probe operating at 8 MHz. In this case, as shown in figure 2.4.a, the inspection can be performed in-loco without removing the specimen from the fixture. The obtained scans were analyzed in the time of flight mode of the scan. A commercial oil-based gel was applied to the surface of the specimen to maximize the coupling between the surface of the specimen and the inspection probe. The through-thickness attenuation system was selected to avoid the reflection effects that can arise from the top surface of the specimen in the dent region and to enable the detection of delamination growth beneath the impact dent area. The pulse-echo scan, on the other hand, was used to identify the delamination depths by determining the time of flight of reflected signals.

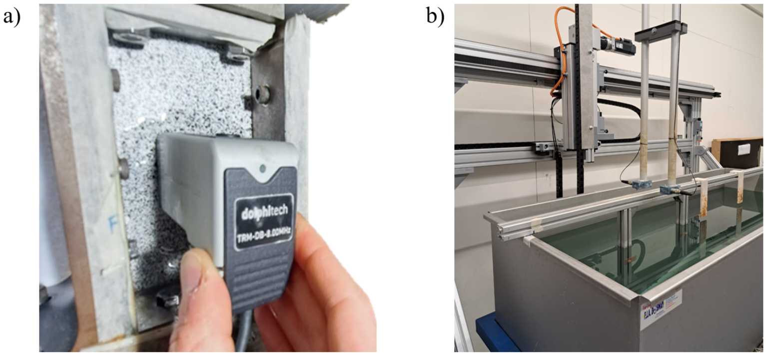

Figure 2.4: Images of the ultrasonic inspections performed showing a) pulse-echo system scanning probe, b) through thickness attenuation water tank

2.3 Results and discussion

2.3.1 LVI tests

The low-velocity impact tests resulted in barely visible impact damages (BVID) characterized by impact dents of < 0.3 mm depth and < 10 mm diameter (figure 2.5). As can be seen from the three-dimensional reconstruction of impact damage, created with the Dolphicam 2 system (figure 2.6.a), the impact damage structure comprises multiple delaminations located in different interfaces. As reported by previous literature, delaminations tend to grow in every interface, bounded by the orientations of the upper and lower plies. Considering this, if the mismatch angle between consecutive plies is kept constant at 45 degrees through the laminate's layup, the delamination envelope will appear like a spiral composed of triangular shapes, all characterized by the same 45-degree angle.

A central area with less attenuation can be observed in the through-thickness transmission scan (figure 2.6.b), indicating that no delamination was formed during the impact in the area below the impact dent. The presence of this feature was discussed in the introduction and can be attributed to the out-of-plane compression originating in the contact between the impactor and the composite plate, which acts as an inhibitor to the delamination propagation. It is important to notice here that, while the non-delaminated region is clearly visible from a through-thickness scan, it is hard to detect this feature using a pulse-echo system. This is because of the echo generated by the curved surface of the impact dent. Results of the impact tests are summarized in table 2.2.

2

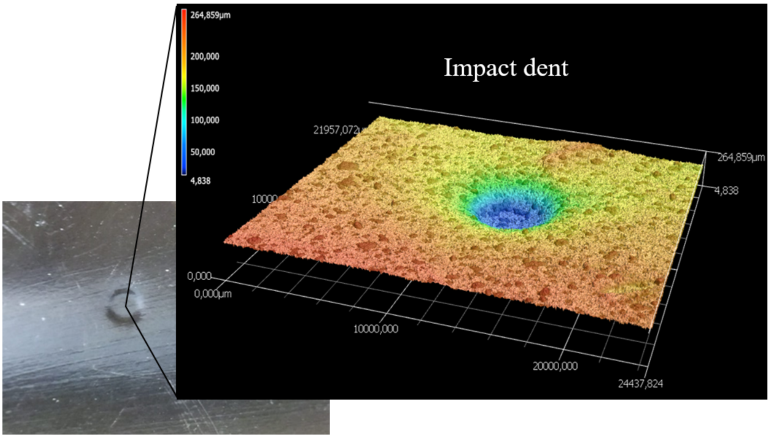

Figure 2.5: Impact dent photo and profile of the dent obtained with optical microscopy showing a dent depth < 0.3 mm

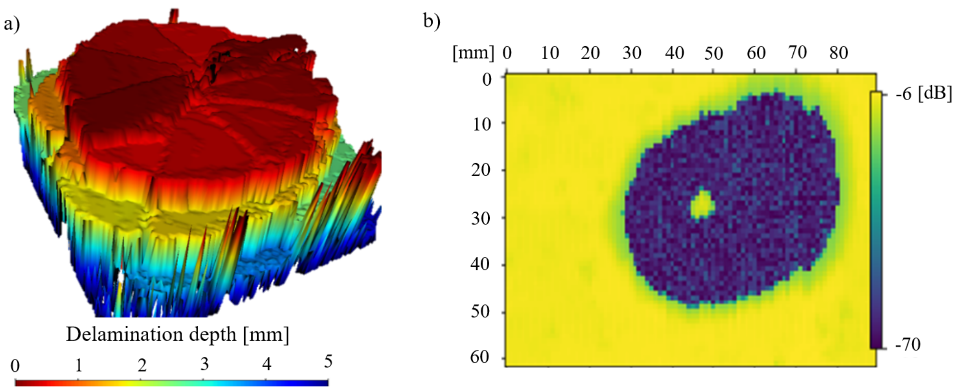

Figure 2.6: Impact damage ultrasound scan obtained with a) pulse-echo and b) through thickness attenuation system

Table 2.2: Low-velocity impact tests data. Delamination width is measured in the perpendicular to the load direction and rounded to the nearest 5 due to limits in measurement resolution

Specimen	Target impact energy	Delamination width
s1	6.7 J/mm	50 mm
s2	6.7 J/mm	50 mm
s3	6.7 J/mm	50 mm
s4	6.7 J/mm	45 mm
s5	6.7 J/mm	45 mm

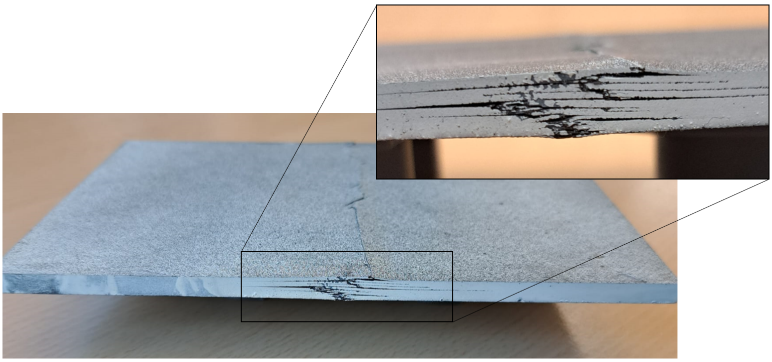

Figure 2.7: Failed specimen in compression fatigue after impact test showing signs of delamination, sublaminate buckling and fiber kinking

2.3.2 CAI fatigue tests

Five specimens were tested for fatigue after impact. Two specimens (s1, s2) were monitored using periodic through-thickness scan inspections. Three specimens (s3, s4, s5) were monitored using periodic pulse-echo scan inspections. The specimens were tested with different load levels to obtain short and long fatigue lives. A scheme of the performed tests can be found in table 2.3. Specimen number 3 (s3) was initially tested at maximum compression stress of 125 MPa but produced no growth after 101,000 cycles; the load was then increased to 145 MPa. At the new load level, the specimen failed after 94,000 cycles. Specimen s5 was initially tested at maximum compression stress of 145 MPa but produced no growth after 179,400 cycles, hence the load was increased to 155 MPa of CAI strength. At the new load level, the specimen failed after 9,600 cycles. The failed specimens show a final fracture that runs in the center of the specimen, perpendicular to the loading direction (figure 2.7). From the side view, it is possible to observe multiple delaminations, local buckling of sublaminates, and fiber kinking.

Table 2.3: Compression after impact fatigue tests data

Specimen	Ultrasound	DIC [y/n]	Max comp load	Life [cycles]
s1	T-T scan	y	115 MPa	200,000
s2	T-T scan	y	145 MPa	3100
s3	E-P scan	y	125 - 145 Mpa	101,000-94,000
s4	E-P scan	y	155 MPa	6,500
s5	E-P scan	y	145 - 155 MPa	179,400-9,600

2.3.3 Attenuation scan - growth in the central cone

In two tested specimens (s1, s2), a through-thickness attenuation scan was used to evaluate growth below the impact contact point.

As explained in previous sections, there is an area below the impact point, with little or no delamination found in the inspections after the LVI test. The results of specimen s1 clearly show how the attenuation in the central area increases over time, prior to any growth in the external area (figure 2.8). Already at 50% of fatigue life, the central area was significantly reduced, until disappearing at 120,000 cycles. This suggests that the delamination propagation first happened in the central area, and only after that, delamination started growing towards the lateral edges.

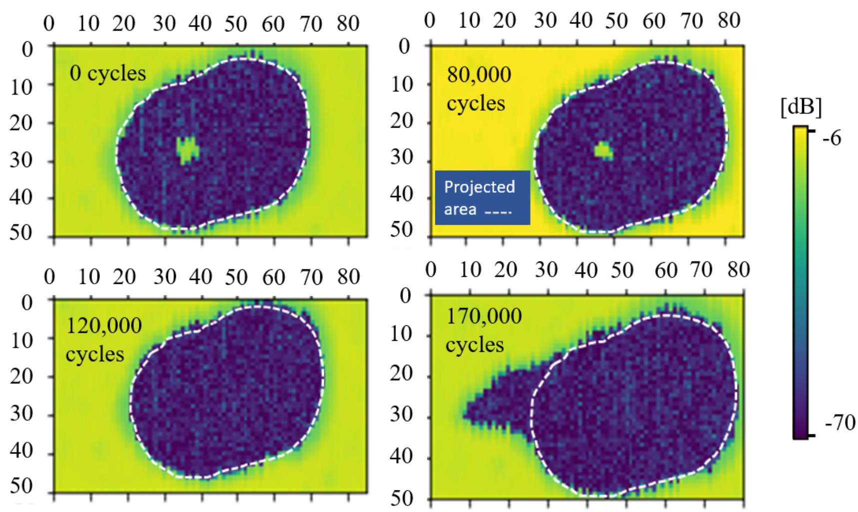

Figure 2.8: through transmission scan monitoring showing growth in the central impact area happening before delamination growth outside of the projected area

The described growth pattern was observed only in the long-life fatigue specimen s1. In the short-life specimen (s2), it was impossible to measure the growth, since all the growth leading to failure happened between two inspections.

This observation confirms a hypothesis raised in the introduction; using delamination width or projected area to describe fatigue growth is not sufficient to capture all the delamination growth since there are delamination growth patterns happening inside the impact damage envelope (figure 2.8). Further investigations should be conducted to assess the relevance of this phenomenon in the fatigue after impact process. Despite being small, delamination growth in the central cone plays a role in the buckling of sublaminates which influences the local stresses and strain energy release rates at delamination external boundaries [12].

It is still not clear, however, if this growth happens systematically and what the relationship is with the geometrical features of the initial impact damage, such as the size of the non-delaminated cone and the shape of delaminations. The impact indentation depth and shape, which was not considered in the present work, is also likely to affect the stress state underneath the indentation and, as a consequence, the growth of delamination in the central cone.

2.3.4 Pulse echo scan - growth of short delaminations

In the second batch of specimens (s3,s4,s5), the pulse echo scan system was utilized to determine the position of delaminations in depth with accuracy.

In the initial stages of fatigue, all the specimens displayed the growth of a single delamination situated close to the impacted face and propagating perpendicular to the loading direction from the impact center towards the lateral edges (figure 2.9). This short delamination grew within the projected delaminated area, hence during the phase that previous studies classified as a plateau phase in delamination growth. It must be noted here that this pattern can only be detected with a pulse-echo system, but it would be invisible to a through-transmission system. This is because it is happening in an area falling inside the overall delamination projection. Even with the pulse-echo system, this growth was observable since it occurred close to the front face and was not shadowed. However, since impact damage consists of multiple delaminations located in almost every interface, it cannot be excluded that faster growth of short delaminations occurred in the central depths during this phase, but was not detected by the c-scan. This consideration reinforces the hypothesis expressed by Pascoe [13], suggesting that the apparent no-growth phase could be a consequence of the inability to measure shadowed growth using ultrasound inspection.

As the delamination continued to grow, the projection of it started to fall outside of the initial impact delaminated area (figure 2.9). Only from this point on, delamination starts to become visible in the through-thickness attenuation and its growth can be appreciated in terms of overall damage width (figure 2.8). At this stage, not only close-to-surface delaminations but also deep delaminations grew in the direction perpendicular to loading. As shown in figure 2.10, signs of delamination migration can be seen in the last scans before failure. Delamination seems to migrate from one interface to the other as it propagates from the impact center to the lateral edges. In all the performed tests, delamination growth happened only in the perpendicular to the loading direction, but no growth was recorded in the parallel to the loading direction throughout the test.

A final interesting observation is shown in figure 2.10, where the final scan before failure (>90 % of fatigue life) is compared in short-life and long-life fatigue specimens (s3,s4,s5). Interestingly, the pattern of delamination growth looks similar regardless of the

2

different applied loads. This suggests that, once the delamination starts to grow in the transverse to the loading direction, a similar propagation pattern is expected in this test for long and short lives.

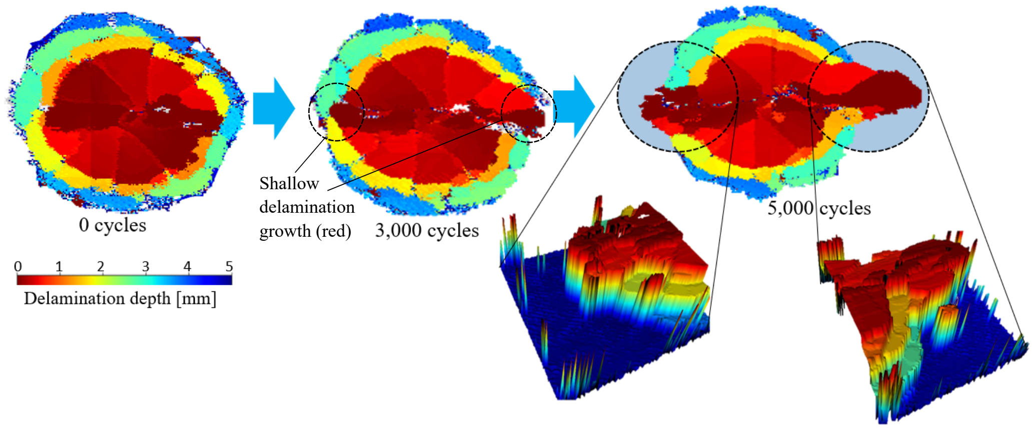

Figure 2.9: Pulse-echo scan monitoring of specimen s4 showing the preferential growth of shorter delamination (in width) happening before the onset of growth outside of the projected area. Initial growth affects mostly shallow delaminations i.e. situated at small depth with respect to the impacted face

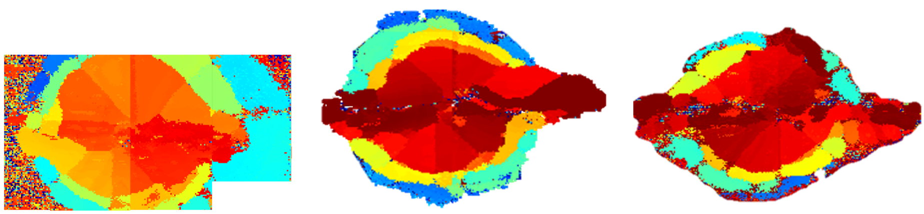

(a) Specimen s3 (b) Specimen s4 (c) Specimen s5

Figure 2.10: Comparison of pulse-echo scans prior to failure (> 90 % of fatigue life) in different specimens with different loads applied and different fatigue lives. Image shows a similar damage envelope before failure, with the extensive growth of delamination of small depths (red colors) in the perpendicular to the loading direction

2.3.5 Digital image correlation

It was shown in the previous section, that propagation of a short shallow delamination happened consistently regardless of the different initial damage and applied load. With shallow it is intended that the ultrasound inspection detected growth at small depths, hence in interfaces situated close to the impacted side of the plate. With short instead, it is intended that the initial growth affected delaminations characterized by a smaller width in the perpendicular to the loading direction. This phenomenon was confirmed by analyzing DIC data and deriving the in-plane compression strain component γ_{yy}.

Figure 2.11, shows the γ_{yy} engineering strain component and compares it with ultrasound inspections at different stages of fatigue life in specimen s4. An elongated shape along the perpendicular to load direction can be individuated. The width of the γ_{yy} concentration area, overlaps the shorter delamination close to the impacted surface seen in the pulse-echo scan in red colors instead of the overall delamination projected width (which is larger). This should not surprise the reader since the presence of delamination determines the loss of out of plane support and the local buckling of the adjacent plies.

As the short delamination propagates, the γ_{yy} concentration elonged shape was observed to propagate at the same rate in the perpendicular to the loading direction. During this phase, intra-ply cracks were also formed in the first ply and were clearly visible from the surface. This led to the gaps observed in the DIC results (figure 2.11) as the formation of these cracks provoked the detachment of DIC paint.

In all the specimens, γ_{yy} concentration showed a propagation compatible with the growth of smaller and shallow delamination in the perpendicular to load direction. This is explained by considering that delamination initially grew in the first interfaces producing a direct effect on the deformation of the first few plies of the laminate. The strain fields of all tested specimens show similar qualitative γ_{yy} profiles evolution through their fatigue life, i.e. growth in the perpendicular to width directions starting form an initial size compatible with impact shallow delamination smaller than the projected impact damage, as shown in the comparative picture (figure 2.13).

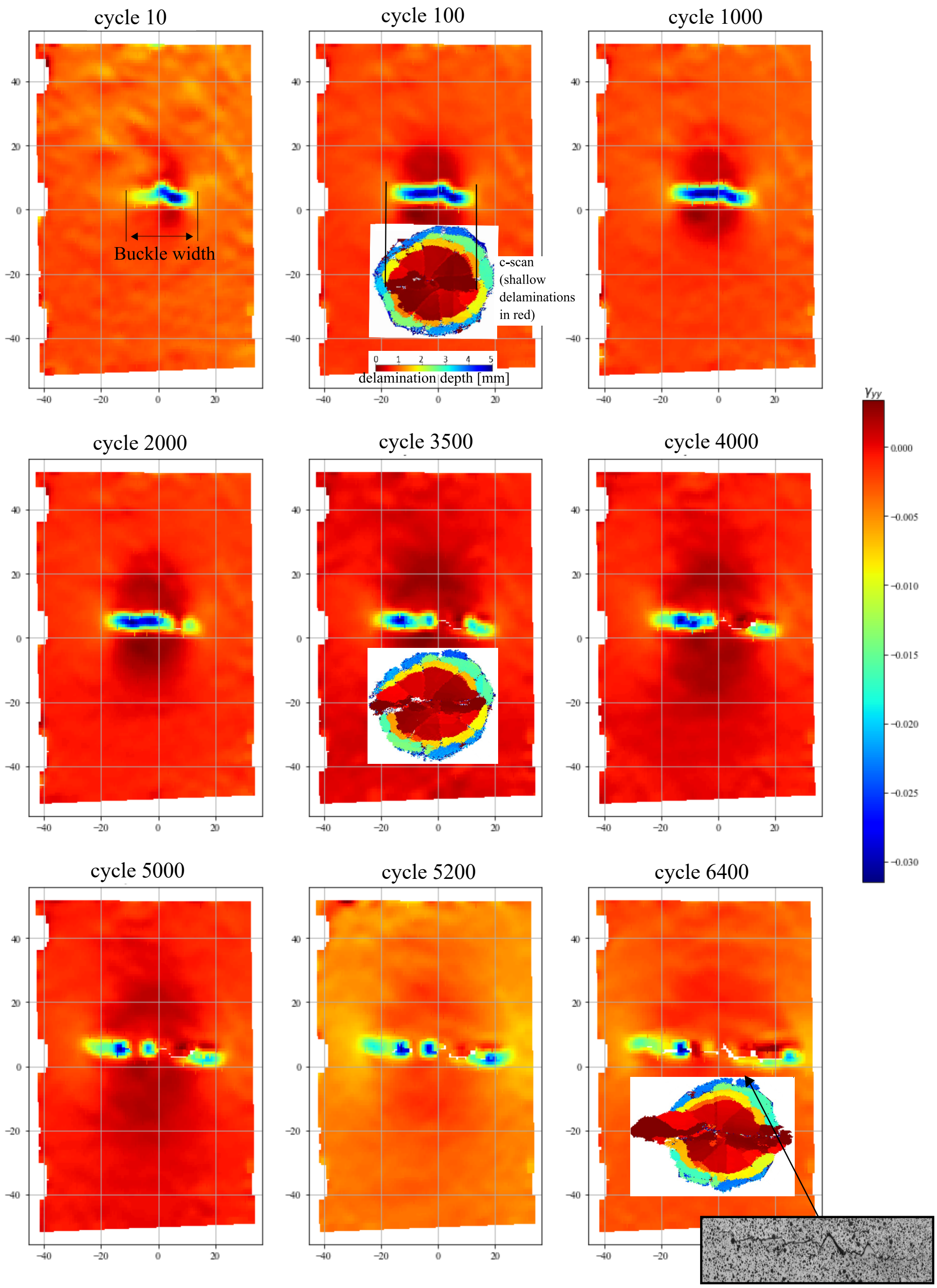

Figure 2.11: DIC results of fatigue propagation showing the γ_{yy} engineering strain in specimen s4. The image on top-center shows how the local buckling width in the perpendicular to the loading direction matches the shallow delamination (red colors in the ultrasounds) and not the larger delaminations

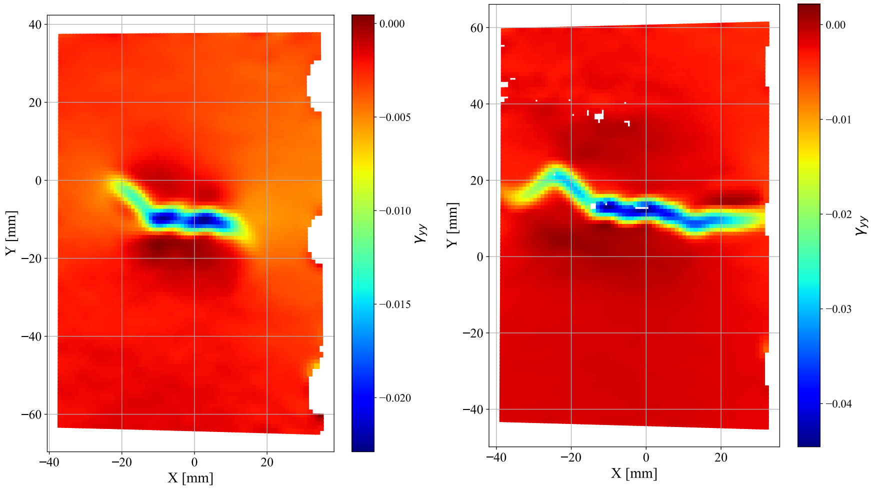

(a) sp 1 at 0% and 90% of fatigue life. Initial projected delamination width (x-direction) = 50 mm

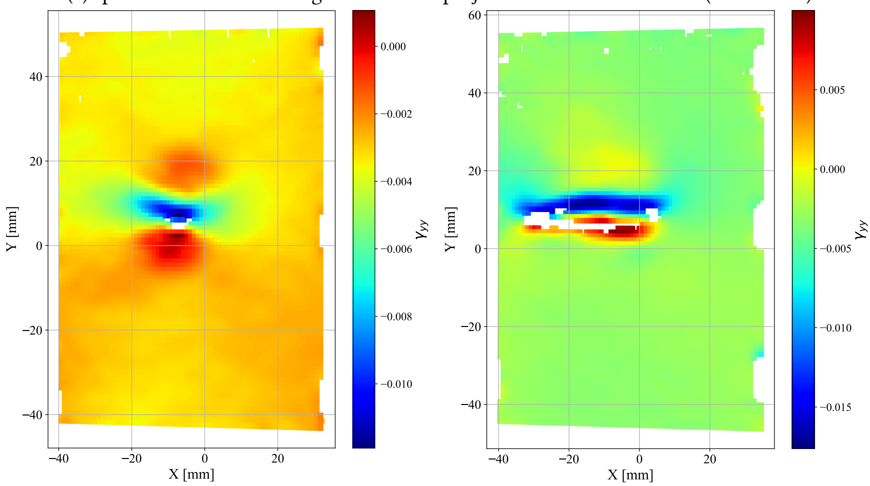

(b) sp 2 at 0% and 90% of fatigue life. Initial projected delamination width (x-direction) = 50 mm

Figure 2.12: Comparison of strain fields at different specimens at the beginning and close to the end of fatigue life. The results show growth of local buckling in the perpendicular to width directions, starting from an initial size smaller than the overall projected width of delamination (in the x-axis direction).

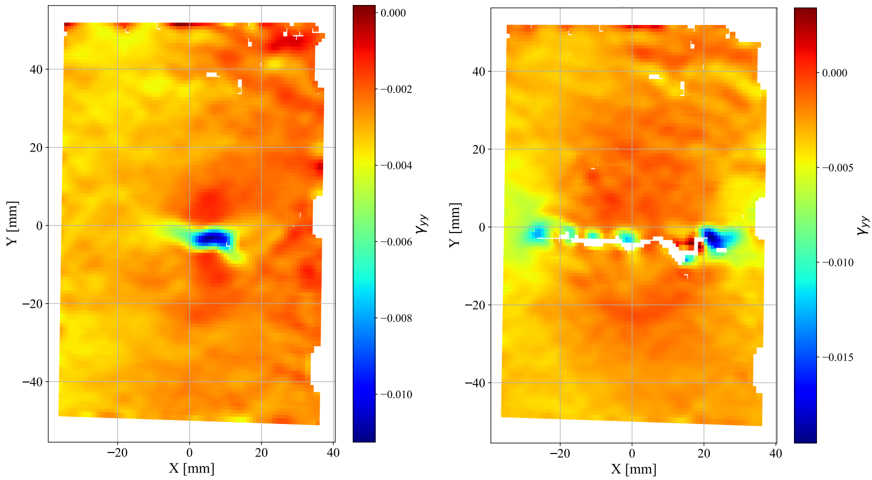

(a) sp 3 at 0% and 90% of fatigue life. Initial projected delamination width (x-direction) = 50 mm

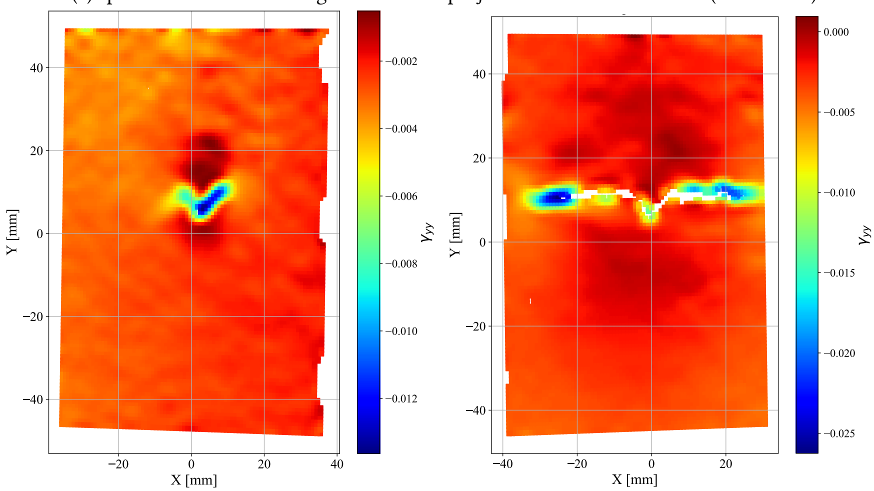

(b) sp 5 at 0% and 90% of fatigue life. Initial projected delamination width (x-direction) = 45 mm

Figure 2.13: Comparison of strain fields at different specimens at the beginning and close to the end of fatigue life. The results show growth of local buckling in the perpendicular to width directions, starting from an initial size smaller than the overall projected width of delamination (in the x-axis direction).

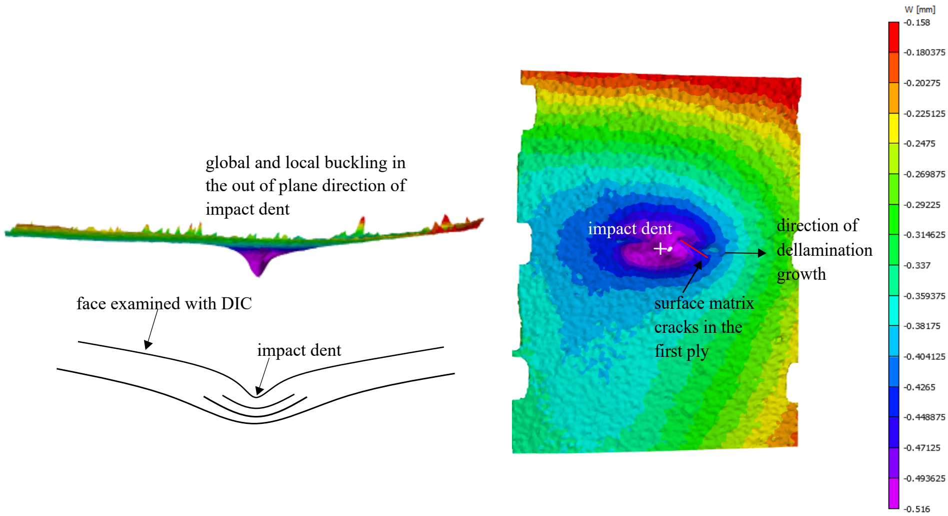

Figure 2.14: Out of plane displacement of loaded specimen s4 derived with DIC analysis. The plot shows the direction of buckling compared to the impact dent. The delamination growth direction and the position of surface cracks is also shown

2.3.6 Mechanisms driving delamination growth: local buckling or intra-ply cracks?

In the previous sections, the initial growth of shallow and short delamination at the onset of fatigue was shown. Two potential mechanisms driving this initial growth can be identified.

The first hypothesis suggests that the growth of short delamination may be propelled by the local buckling of sublaminates, as proposed by previous authors [14, 15]. Results from the preceding section reveal an area of strain accumulation that expands as the delamination progresses. Interestingly, the out-of-plane deformation derived from DIC (Figure 2.14) illustrates that local buckling in the impact area occurred in the same direction as the dent and global buckling. While local buckling indeed expands concurrently with the delamination, it's worth noting that this configuration isn't compatible with significant mode I opening at a delamination tip located near the impact face. Planar delamination fronts in shallow delaminations beneath the impact surface are primarily subjected to mode II opening.

In addition to the presence of local buckling, transverse cracks were also observed in the first ply starting from the impact dent and propagating as the delamination grew (Figure 2.11). These cracks formed at a preferential angle of 45 degrees, parallel to the fiber orientation in the first ply. The growth of shallow delamination observed in the initial stages of fatigue could also be attributed to the formation of these intra-ply cracks, which subsequently migrate within the interface underneath.

Previous literature has linked impact delamination fatigue growth to sublaminate buckling [14, 15], but to the author's knowledge, no known work has proposed a second possible mechanism. It remains unclear how these damage mechanisms are interrelated and what exactly drives the initial growth of delamination.

2.3.7 Fatigue delamination growth threshold

The results presented in the previous sections (2.3.4 and 2.3.3) clearly indicate that the projected area or total width of delamination is *not* a good descriptor for damage propagation. This is because the growth of shorter and shallow delamination was observed. With 'shallow' it is intended that the ultrasound detected growth at small depths, hence in interfaces situated close to the impacted surface. With 'short' instead, it is intended that the initial growth affected delaminations characterized by a smaller width in the perpendicular to the loading direction.

Considering the evolution of delamination that was observed, it was decided to use the width of the delamination that started to grow earlier as a new descriptor for fatigue damage growth. This damage descriptor can be retrieved conversely by using a pulse-echo scan and by performing DIC analysis as shown in section 2.3.5 (figure 2.11). The advantage of DIC in this context is the possibility to use a more populated set of acquisitions throughout the fatigue life. Digital image correlation, unlike ultrasound, does not require stopping the test for a long time to perform inspections and can be automated without a human operator. The surface deformation was therefore used to indirectly reconstruct the propagation of short shallow delamination. It must be noted here that the application of DIC to monitor fatigue after impact damage propagation could only be possible thanks to the preferential growth of shallow delamination.

In Figure 2.15, the trends of buckle width over cycles are reported in short and long-life fatigue specimens. First, it can be appreciated how superior this new metric is in describing fatigue damage propagation. In both long-life (specimen s3) and short-life (specimen s4), the damage envelope width or area fails to capture the initial phase of growth which is instead observed in the buckle width. Interestingly, in the case of specimen s4 (Figure 2.15a), previous studies like the early work by Chen [5] would have identified a plateau phase followed by a fast increase in delaminated area width. If buckle width is monitored instead, gradual growth occupying the entire fatigue life is observed. Some of the discrepancies in previous experiments then, can be justified by an incomplete observation of damage growth, and incorrectly identified plateau phases of damage growth could be caused by the selection of the wrong damage propagation descriptors. However, can all the different observed behaviors be explained with the selection of wrong damage descriptors?

If the same fatigue test is conducted at lower maximum compressive stress, still adopting buckle width as a descriptor of damage propagation (Figure 2.15b), a largely different propagation trend is observed. In specimen s3, a first phase of fast propagation of buckle after the very first cycles was followed by a steady phase in which no apparent growth was observed, followed by a fast growth leading to failure. This indicates that, even adopting more refined damage descriptors, the presence of a plateau phase in fatigue growth like the one observed by previous research *cannot* be excluded. As further evidence, compliance plots during the fatigue life of the same specimens are reported in Figure 2.16. In the case of short life, where delamination growth and buckle extension happened from the beginning of fatigue life, a gradual increase of compliance is observed (Figure 2.16a). In the case of long life instead, there is a central phase of no compliance increase followed by a final increase of compliance. This trend follows the behavior of buckle area increase shown in Figure 2.15b. These results show that different applied stresses can determine different trends in delamination growth. A similar applied stress effect has been reported in the experiment of Tuo et al. [6] by adopting thermography. In the author's opinion, referring to this phenomenon as the 'applied stress effect' is not scientific and does not help the understanding. What we could be observing here is the presence of a threshold for delamination growth. Two scenarios can therefore take place:

- The threshold is exceeded; a gradual propagation starts and occupies all fatigue life.
- The threshold is not exceeded; a phase of transition takes place in which other damage modes may be active first.

This threshold should be defined in terms of the local stress state and not in terms of applied stress. This is because the same applied stress can produce largely different local stress states at the delamination fronts if the impact damage shape is different. It must be noted here that we are not referring to a threshold for no growth or fatigue limit. In this case, fatigue growth and eventually delamination growth will happen. This is a threshold determining if the delamination starts to grow immediately or if there is damage accumulation phase before that. To define precisely this threshold, further investigation has to be conducted since the trigger mechanism for delamination growth is still uncertain (as expressed in section 2.3.6).

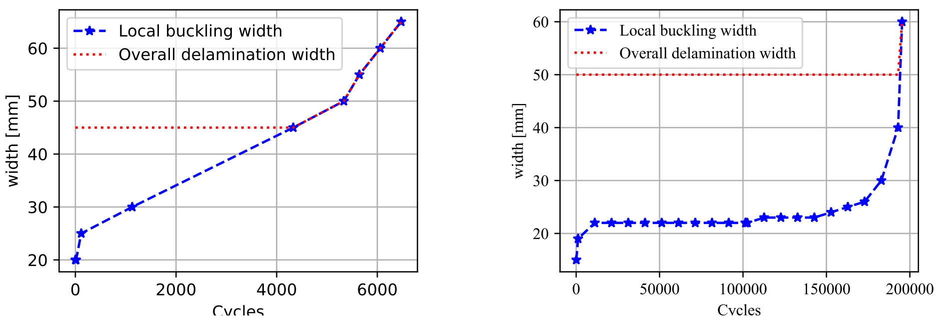

(a) Short fatigue life (specimen s4)

(b) Long fatigue life (specimen s3)

Figure 2.15: Growth of the local buckling width in (a) short and (b) long fatigue lives. The width is defined in the perpendicular to load direction as represented in Figure 2.11

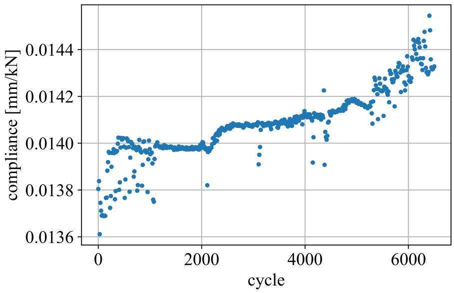

(a) Short fatigue life (specimen s4)

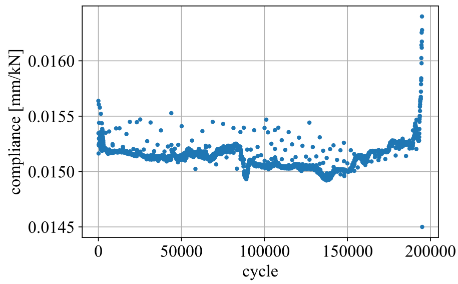

(b) Long fatigue life (specimen s3)

Figure 2.16: Degradation of stiffness in (a) short and (b) long fatigue lives

2.4 Generality of the results

In this chapter, several aspects of delamination propagation have been described, and some previously undocumented phenomena have been observed. How general these results are, however, remains uncertain.

The preferential growth of delamination perpendicular to the loading direction, is a pattern that is consistently found in the literature of CAI fatigue of CFRP [3, 6]. There is the exception of the early work by Mitrovic et al. [7]. In this work, a propagation parallel to the loading direction was observed. The test fixture used in that study however, was different from the ASTM static CAI test fixture [11] and had a much more elongated shape in the loading direction without anti-buckling guides. This confirms that there is a high dependency on the adopted test fixture of the results. Among the tests performed using the ASTM standard fixture, the growth of delamination perpendicular to loading was consistently observed. The ASTM standard text fixture prevents the global buckling of the panel and enforces a local buckling. This has a direct effect on the strain energy release rates at delamination fronts.

Even in cases where the standard CAI fixture was used, some differences are present in the depth position of the delamination growth. In the previous work by Tuo et al. [6] a similar CFRP but with a different layup was tested in CAI fatigue and a growth of delamination close to the opposite to impact face was reported. In contrast, in the present study, the growth of delamination situated in interfaces close to the impacted face was consistently observed. It must be noticed that, in the two works, a different layup was used. This shows that there is a large variability in results caused by different layups, and initial impact damage shape.

2.5 Conclusions

An experimental campaign was conducted to investigate the phenomenon of delamination growth in compression fatigue after impact. Two types of ultrasound scans (through transmission scan and pulse-echo scan) were used to monitor delamination growth. Combining the two systems, an accurate reconstruction of delamination growth was provided, showing similar scans of delamination before failure for both long and short fatigue lives.

The first outcome of this investigation was that the projected delaminated area or impact damage width is *not* a sufficient descriptor for damage growth. The practice of adopting those damage descriptors could have led to many misinterpretations of results in the past. In fact, during a 'no-growth' phase of the projected impact delamination area growth, two other damage accumulation mechanisms were observed:

1. By using the through-thickness transmission scan, it was possible to see the growth in the non-delaminated cone, a phenomenon previously observed only in quasi-static tests.
2. By using an pulse-echo system it was possible to detect the preferential growth of superficial shorter delaminations within the projected delamination impact area.

Although many of the observed features in delamination growth were consistent regardless of the applied load and different initial damage, the dependency on the adopted test fixture, loading conditions, and initial impact damage remains unclear.

In combination with ultrasound monitoring, digital image correlation was analyzed to measure indirectly the growth of surface delamination. Buckling width proved, in this specific case, to be a superior descriptor of damage propagation in fatigue compared to the previous approaches based on the overall projected area. The application of DIC to monitor fatigue after impact damage propagation, however, works effectively only in case of the preferential growth of shallow delamination.

The obtained damage propagation curves indicate that even using a more precise damage descriptor, a plateau phase cannot be excluded. In similar tests, delamination growth was observed for higher applied stress, while for lower stress a slow-fast propagation took place. This suggests that a threshold for the onset of delamination growth may be present. In case the applied stress exceeds the threshold delamination growth starts and occupies all fatigue life. If instead, the applied stress is lower than the threshold, a phase of transition takes place in which other damage modes or shadowed delaminations may be active. To understand what is happening during this phase, the adopted monitoring strategies were not sufficient.

2

References

[1] Davide Biagini, John-Alan Pascoe, and René Alderliesten. Investigating apparent plateau phases in fatigue after impact damage growth in cfrp with ultrasound scan and acoustic emissions. *International Journal of Fatigue*, 177:107957, 2023.

[2] D. Biagini, J.A. Pascoe, and R.C. Alderliesten. Experimental investigation of fatigue after impact damage growth in cfrp. *Procedia Structural Integrity*, 42:343–350, 2022. 23 European Conference on Fracture.

[3] Fan Xu, Wenli Liu, and Phil E. Irving. Fatigue life and failure of impact-damaged carbon fibre composites under compressive cyclic loads. *ICCM International Conferences on Composite Materials*, 2017-Augus:20–25, 2017.

[4] Toshio Ogasawara, Sunao Sugimoto, Hisaya Katoh, and Takashi Ishikawa. Fatigue behavior and lifetime distribution of impact-damaged carbon fiber/toughened epoxy composites under compressive loading. *Advanced Composite Materials*, 22:65–78, 2013.

[5] A. S. Chen, D. P. Almond, and B. Harris. Impact damage growth in composites under fatigue conditions monitored by acoustography. *International Journal of Fatigue*, 24:257–261, 2002.

[6] Hongliang Tuo, Tao Wu, Zhixian Lu, and Xiaoping Ma. Evaluation of damage evolution of impacted composite laminates under fatigue loadings by infrared thermography and ultrasonic methods. *Polymer Testing*, 93, 1 2021.

[7] Milan Mitrovic, H. Thomas Hahn, Greg P. Carman, and Peter Shyprykevich. Effect of loading parameters on the fatigue behavior of impact damaged composite laminates. *Composites Science and Technology*, 59:2059–2078, 1999.

[8] G. Clark and T. J. Van Blaricum. Load spectrum modification effects on fatigue of impact-damaged carbon fibre composite coupons. *Composites*, 18:243–251, 1987.

[9] Lucas Amaral. *Towards fundamental understanding of interlaminar ply delamination growth under mode II and mixed-mode loading*. Dissertation (tu delft), Delft University of Technology, 2018.

[10] Compass ASTM D7136 D7136M-15. Standard test method for measuring the damage resistance of a fiber-reinforced polymer matrix composite to a drop-weight impact event.

[11] Compass ASTM D7137 D7137M-17. Standard test method for compressive residual strength properties of damaged polymer matrix composite plates.

[12] D. J. Bull, S. M. Spearing, and I. Sinclair. Observations of damage development from compression-after-impact experiments using ex situ micro-focus computed tomography. *Composites Science and Technology*, 97:106–114, 2014.

[13] John-Alan Pascoe. Slow-growth damage tolerance for fatigue after impact in FRP composites: Why current research won't get us there. *Theoretical and Applied Fracture Mechanics*, 116:103127, 2021.

[14] L. Gunnar Melin and Joakim Schön. Buckling behaviour and delamination growth in impacted composite specimens under fatigue load: An experimental study. *Composites Science and Technology*, 61:1841–1852, 2001.

[15] L. G. Melin, J. Schön, and T. Nyman. Fatigue testing and buckling characteristics of impacted composite specimens. *International Journal of Fatigue*, 24:263–272, 2002.

3

Surrogate fatigue after impact

PTFE inclusions can be used to produce a surrogate of impact damage and test it in fatigue.

By utilizing this approach, similar and dissimilar growth patterns can be observed, compared to CAI fatigue tests. Similarly to CAI fatigue, in an advanced growth state, the planar growth of multiple delaminations in the perpendicular to load direction happened. The dissimilarities regarded the position in depth of delamination growth and the local buckling profiles.

Despite the limitations, the fatigue growth of multiple planar delaminations was obtained in compression fatigue. The growth of these delaminations, in opposition to fatigue after impact cases, proved to be slow and stable. This suggests that, if the conditions are similar to the surrogate, a slow growth of planar delamination can happen in compression fatigue.

3

3.1 Surrogate impact delamination

The previous chapter provided an updated and advanced description of impact delamination growth in fatigue highlighting some technical challenges associated with the monitoring techniques. The C-scan method is widely used for its capability to provide a precise delamination contour but its interpretation is affected by the shadowing phenomena. On the other hand, DIC offers valuable insights into delamination propagation but provides only indirect information about shallow delaminations affecting the interfaces close to the surfaces. Considering those technical limitations, in a CAI fatigue test, the initial state of impact damage is not completely known since several delamination, located deep in the laminate, are shadowed. This uncertainty worsens in the following growth since many delamination fronts are not visible by the available techniques. In addition to that, intra-ply matrix cracks and occasional fiber failures accompany delamination, making it impractical to decouple the propagation of delamination from these other damage mechanisms.

In this chapter, results are presented from an experiment designed to overcome the previously described issues and gain a better understanding of fatigue after impact delamination growth. A surrogate of impact damage is created by embedding Polytetrafluoroethylene (PTFE) foils in the ply interfaces. PTFE is known for its non-stick properties and its resistance to high temperatures. This means that it's possible to insert thin layers of PTFE in a layup and conduct curing cycles in the autoclave. The PTFE inclusions in the cured laminate detach at low load and produce a free surface inside the material. The resulting component behaves then as if delaminated, since the edges of the PTFE inclusion act as initial sites for cracks running in the ply interfaces.

In the literature some tests have been performed using this strategy [1–4], however, they all adopt a limited number of inclusions. In many cases the shape of the inclusion is simple and the tests are used to validate numerical models [5] in cases which are simpler than fatigue after impact.

In this chapter, an attempt is made to reproduce impact damage as precisely as possible using multiple PTFE inclusions. The inclusions are located in each interface, with accurate alignment, and present variable shapes and sizes to achieve a damaged cone similar to impact damage. In some of the specimens, annular inclusions are used to test the presence of a central non-delaminated area. The test is designed to present the following advantages:

- The initial state of damage is fully known.
- The initial damage does not present shadowed fronts to a c-scan inspection performed on both sides.

The PTFE impact damage surrogates are tested in compression fatigue and delamination propagation is monitored using ultrasound and DIC. Results from the tests are then critically compared to the fatigue after impact scenario.

3.2 Methodology

In the following subsections, the methodology of the experimental campaign is reported. First, the manufacturing procedure is explained paying attention to the PTFE inserts alignment. In the second subsection, the specifics of the performed fatigue tests are provided.

3.2.1 Manufacturing of the surrogate impact damage

The PTFE fatigue tests utilized the same Toray M30SC Deltapreg DT120-200-36 UD prepreg as employed in the Compression After Impact (CAI) tests, described in Chapter 2. The laminate was laid up in a $[-45, 0, 45, 90]_{2,S}$ orientation, resulting in a thickness of 2.6 mm. During the layup process, PTFE inserts as the ones shown in Figure 3.1, were positioned at all interfaces where a mismatch angle between the upper and lower plies existed. This is because in impact damage delamination forms only in the presence of the mismatch angle. Considering this, no PTFE insert was placed in the central interface between two plies of 90-degree orientation. All PTFE inserts were manually aligned and positioned during the layup process thanks to the use of a reference alignment scheme on non-stick paper.

To generate distinct delamination envelopes (see Figure 3.1b) and replicate impact damage structures, diverse shapes of PTFE inserts were employed (Figure 3.1a). Circular PTFE inserts were used in two specimens of class **C**, with the radius gradually increasing from one surface to the other of the laminate. This methodology aimed to emulate the damage cone typically observed in impacted specimens. Additionally, specimens of classes **Ac** and **Anc** were fabricated with annular inserts to mimic the presence of a non-delaminated central area. In the case of **Ac** specimens, the internal area also exhibited a conical envelope (see Figure 3.1b). All the geometries were designed to not have any shadowed delamination front if ultrasound inspection is performed on both sides.

The vacuum bag and curing process was conducted as described in the previous chapter. The curing cycle in the autoclave was applied to one large plate (figure 3.1c) of dimensions 400 × 600 mm which then was cut into six smaller rectangles using a circular diamond blade. The final specimens had nominal dimensions of 150 × 100 × 2.6 mm.

3.2.2 Fatigue test setup

The test was conducted using the fixture of CAI fatigue tests introduced in the previous chapter. An MTS 100 kN uni-axial hydraulic testing machine was used in the force control option. To decide which load to apply, a slow compressive displacement ramp (1 mm/min) was applied to specimen C-1 until the PTFE inserts detached and a buckling snap was observed. The obtained load was then used as maximum compression stress in the following fatigue test. The fatigue load applied was a compressive load of max compression 10.3 MPa, R = 10, and frequency of 3 Hz. In all specimens before starting the fatigue test, a slow ramp until the maximum compressive load was applied before starting the fatigue test. A three-dimensional digital image correlation (DIC) system was used on both sides of the specimen to evaluate the surface displacement. It was decided to apply the system to both surfaces to obtain a more complete view of the sub-laminates buckling. The system adopted in the current experiment consisted of four nine MP "Point Grey" cameras (two per side) with 'Tamron' 25 mm lenses. The speckle pattern images were captured by ViC-Gauge

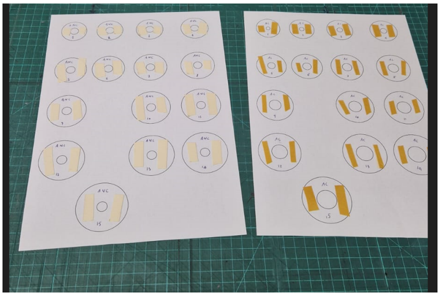

(a) PTFE rings (in figure placed on a sheet of paper) before being located in the prepreg, one per each interface

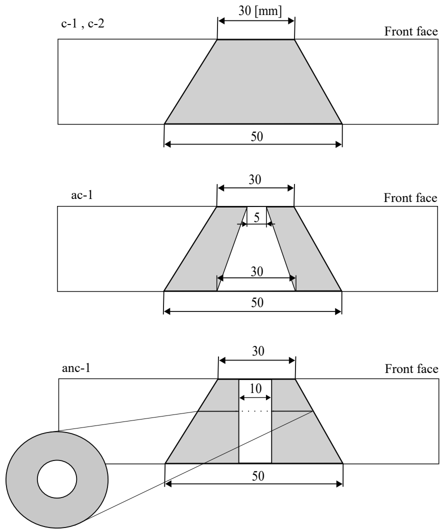

(b) Schematic of the section of the specimens. The grey areas indicate where the PTFE circular or annular inclusions are situated

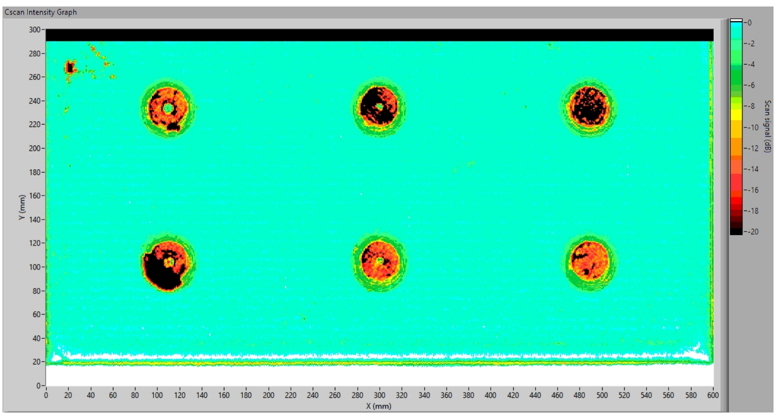

(c) Ultrasound scan of the manufactured plate

Figure 3.1: Manufacturing of specimens with PTFE inserts. The initial geometry doesn't have shadowed PTFE fronts if echo-pulse is performed on top and bottom of the specimens.

3D software with an acquisition rate of one frame per second (fps). The specimens were periodically inspected with a pulse-echo Dolphicam 2 system, equipped with a scanning probe operating at 8 MHz. The obtained scans were analyzed in the time of flight mode of the scan.

3.3 Results and discussion

In the following sections, the results of the experimental campaign are reported and discussed. In the experimental campaign, only specimens C-1, C-2, Ac-1 and Anc-1 were tested. Two specimens (Ac-2 and Anc-2) were manufactured but preserved for future research. First, the stiffness degradation through fatigue life is shown. Then the DIC displacement profiles are presented to discuss buckling shapes. Finally, the propagation of delaminations under fatigue is discussed. The final considerations concern the similarities and differences between the PTFE test and CAI fatigue, and what we can learn form this test.

3.3.1 In-plane compliance increase in fatigue tests

The fatigue test results are listed in table 3.3.1. Specimens C-1 and C-2 exhibited the shortest fatigue life and the highest initial compliance. This can be explained by considering that the overall delamination area was larger in specimens C-1 and C-2. The fatigue life of specimen Anc-1 instead exceeded by far the fatigue life of all the other specimens.

Figure 3.2, shows the compliance increase over the fatigue life in the different specimens. Specimen C-1, in which the detachment of PTFE inclusions and the local buckling snap was obtained before the beginning of the fatigue test, showed a progressive increase in compliance throughout a large part of the fatigue life. A jump in compliance was observed close to the end of fatigue. This specimen was the first one tested in the campaign and in this case, the PTFE had already detached at the beginning of the fatigue test. On the contrary, in the case of specimen C-2 the PTFE inserts did not detach in the loading ramp before the fatigue test and the buckling snap happened in the following fatigue cycles. This can be seen in the compliance plot where the first flat phase (before the snap) was followed by an abrupt increase in compliance (snap). This phenomenon of retarded snap was also observed in specimens Ac-1 and Anc-1.

It is interesting to notice how in all the tested cases, once the PTFE detaches, a gradual increase in compliance is observed for a large part of fatigue life, suggesting the growth of planar delamination. This is confirmed by the ultrasound monitoring, as will be shown in the following sections. In specimen C-1 a second abrupt increase in compliance was observed after 40,000 cycles. The interpretation of the author is that the detachment of some of the PTFE inclusions still sticking together happened in this case.

The final failure in all the specimens showed a fracture similar to fatigue in CAI. The damage progressed in the perpendicular to load direction, starting from the PTFE insert area towards the lateral edges. The failed specimens presented signs of delamination, unstable buckling of sublaminates and fiber kinking. Recalling the results from Chapter 2, in CAI fatigue tests, the presence of a plateau phase was found for long-life fatigue specimens. This plateau phase was identified with delamination monitoring and compliance curves. Interestingly in the surrogate test, this phenomenon was not observed in long-life fatigue tests, since a gradual increase in compliance occupying the majority of fatigue life took place instead.

Table 3.1: Results of fatigue tests

Specimen	Maximum compression stress	Fatigue life
C-1	10.3 MPa	53’000 cycles
C-2	10.3 MPa	73’000 cycles
Ac-1	10.3 MPa	96’000 cycles
Anc-1	10.3 MPa	255’000 cycles

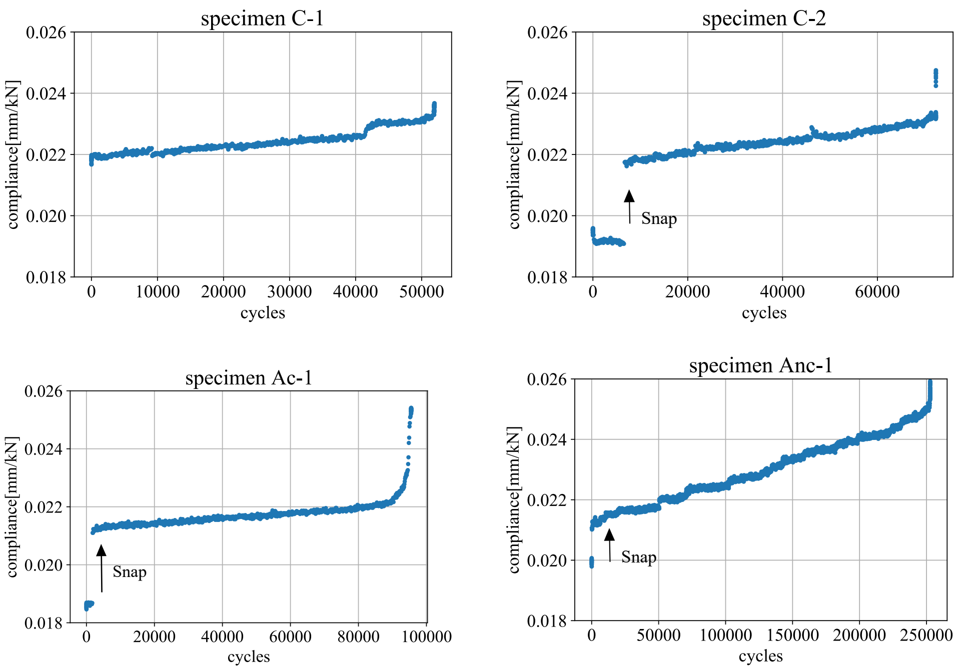

Figure 3.2: Stiffness degradation illustrated through compliance increase in different specimens

3.3.2 Buckling shapes

DIC analysis shows that after the snap, all the specimens deformed with a composition of global and local buckling. In the discussion that follows, the term ’front face’ is used to refer to the side of the laminate closest to which the smaller PTFE inclusions are located (see the PTFE insert structures in Figure 3.1b). This convention is adopted based on typical impact damage observations, where the impacted face, referred to as the front face of the specimen in Chapter 2, is also the one presenting smaller delaminations.

In all specimens, a global buckling deformation towards the front face happened. In the back face instead, local buckling of sublaminates produced an out-of-plane displacement in the opposite direction of global buckling. This scenario is compatible with delamination mode I opening. This is because while the full specimens deformed towards the front face (global buckling), specific regions deformed towards the back face (local buckling) opening the delaminations. Results from the digital image correlation are illustrated in Figure 3.3 and Figure 3.4. In the figures, the surface out-of-plane displacement just after the buckling snap is reported. These pictures were acquired when the specimen where at 90% of the maximum compression loading applied in the fatigue cycle.

In specimens Ac-1 and Anc-1 (figure 3.4), a similar composition of global-local buckling was observed. However, the back face showed two half local buckles indicating the presence of the central non-delaminated cone. The central non-delaminated area in the back face, as expected, was larger in specimen Ac-1 compared to Anc-1.

The snap to the sublaminate buckling, even in case a slow ramp was applied, was a rapid phenomenon provoking the detachment of part of the paint (as can be seen in figure 3.3b). The sublaminate buckling was quite large and generated high shear stresses. This provoked in specimens Ac-1 and Anc-1, two matrix cracks running parallel to the 45-degree fiber orientation (direction of the first ply). Those superficial matrix cracks produced a non-negligible effect on the displacement profile since they acted as boundaries of the local buckles (figure 3.4) .

Recalling results from Chapter 2, one significant difference can be individuated compared to the CAI buckling profiles (Figure 2.14). The global buckling of the PTFE specimens happened towards the front face and was in contrast with the CAI specimens which deformed in the direction of the back face. One possible explanation for this difference could be the action of the impact dent, a pattern that is present in impact damage but was not reproduced in the surrogate test. Impact dent acts as an initial perturbation and is likely to induce a global deformation towards the back face in CAI specimens.

Although the overall direction of out-of-plane displacement was different, in both the CAI and PTFE tests, the local buckling assumed an elliptical shape. The local buckling shape was elongated in the direction perpendicular to loading and expanded as the delamination propagated in fatigue.

One last difference between CAI fatigue and the PTFE test buckling modes has to be highlighted. In the impacted specimen front face, the local buckling out-of-plane displacement had the same direction as global buckling and impact dent (Figure 2.14). For this reason, in the case of CAI fatigue tests, the front face did not present out-of-plane displacements compatible with mode I opening of delamination (at least in the shallow layers underneath the front face). In the case of PTFE tests instead, the local buckling at the back face had an opposite out-of-plane direction compared to global buckling. This configuration allows for a mode I opening at the delamination fronts.

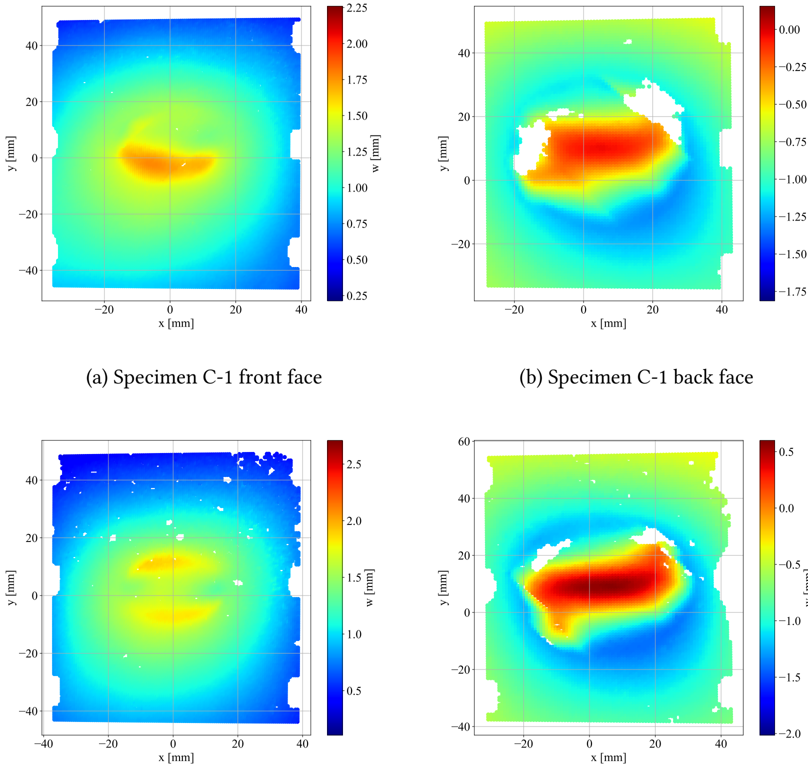

(a) Specimen C-1 front face

(b) Specimen C-1 back face

(c) Specimen C-2 front face

(d) Specimen C-2 back face

Figure 3.3: Out of plane displacement in specimens C-1 and C-2 derived with DIC. In the back face of the specimens (right sides figures) a positive out-of-plane displacement area (in red) surrounded by a negative out-of-plane displacement area (in blue) denotes the presence of local buckling having opposite out-of-plane displacement compared to the global buckling.

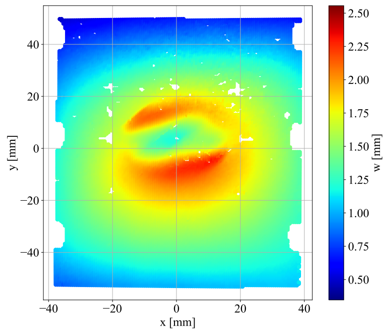

(a) Specimen Ac-1 front face

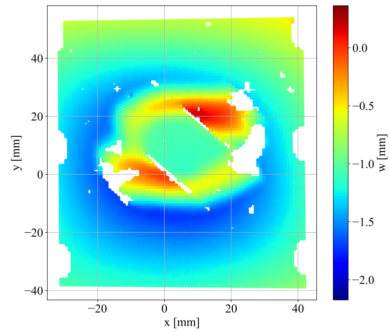

(b) Specimen Ac-1 back face

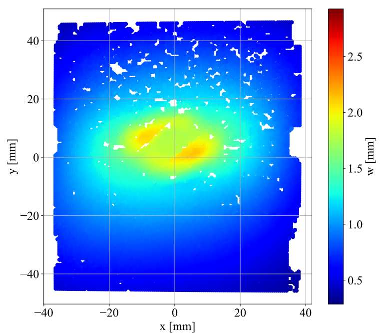

(c) Specimen Anc-1 front face

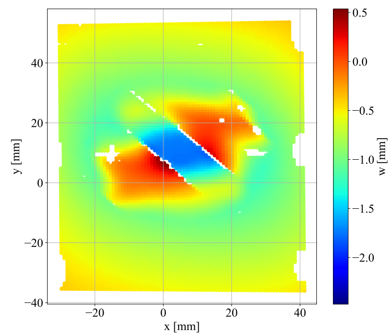

(d) Specimen Anc-1 back face

Figure 3.4: Out of plane displacement in specimens Ac-1 and Anc-1 derived with DIC. In the back face (right side figures) a positive out-of-plane displacement (in red) area surrounded by a negative displacement area (in blue) denotes the presence of local buckling having opposite out-of-plane displacement compared to the global buckling. A double/shape local buckling can be seen in both cases, caused by the presence of a central non-delaminated zone.

3.3.3 ULTRASOUND INSPECTION

After the buckling snap, the specimens exhibited a significant out-of-plane deformation which resulted in a difficult acquisition of the ultrasound scans. In all specimens, a preferential growth of delamination in the perpendicular to load direction was observed (Figures 3.5 and 3.6). This agrees with the observation performed in CAI fatigue tests, where delamination preferentially grew in the perpendicular to load direction. In all the specimens, the growth of delamination was gradual and occupied the majority of fatigue life. No plateau phase was observed even in the case of long fatigue life. This presence of gradual growth of delamination was confirmed by the compliance plots showing a gradual deterioration of stiffness (figure 3.2). This observation is in contrast with the CAI fatigue results shown in the previous chapter, where a phase of transition with little growth was observed followed by a delamination propagation occupying a small window towards the end of fatigue life.

In specimens C-1 and C-2, the simultaneous growth of delamination at multiple interfaces and depth positions happened (Figure 3.5). In specimen Ac-1, multiple delamination grew preferentially towards the right side of the specimen (from top) with extensive propagation both in shallow and deep depths (Figure 3.6). Finally, specimen Anc-1 showed the preferential growth of delamination situated close to the back of the specimen, with very little propagation at shallow depths (Figure 3.6). The growth of delamination from multiple interfaces confirms that the detachment of the PTFE insert was obtained in multiple interfaces at the same time at least in specimens C-1, C-2 and Ac-1.

Specimens Ac-1 and Anc-1 were designed to have a central area with no delamination similar to the one observed in impact tests. The goal was to monitor and document the growth in the non-delaminated cone in a simpler case with no shadowing of delamination and no impact-dent reflection issues. The central area, however, was challenging to monitor with pulse-echo scan due to the high buckling deformations and the presence of surface cracks. Because of this, in specimen Ac-1, it's unclear if this phenomenon happened in some interfaces with the resolution of the performed scans (Figure 3.6). It's quite clear that this growth didn't happen in shallow delaminations since the sublaminate kept a two-half buckle deformation through the entire fatigue life as shown in the DIC analysis. Specimen Anc-1 didn't show signs of a complete delamination growth in the non-delaminated central area. In fact, the scan performed from the front face shows the reflection of the back face in the central area at more than 90% of fatigue life (Figure 3.6) proving the absence of delamination. This observation is in contrast with the CAI fatigue results of the previous chapter, where the preferential growth in the non-delaminated central area was observed before the growth in the undamaged cone (Figure 2.8). Specimen Anc-1 instead, didn't show a complete growth in the central cone

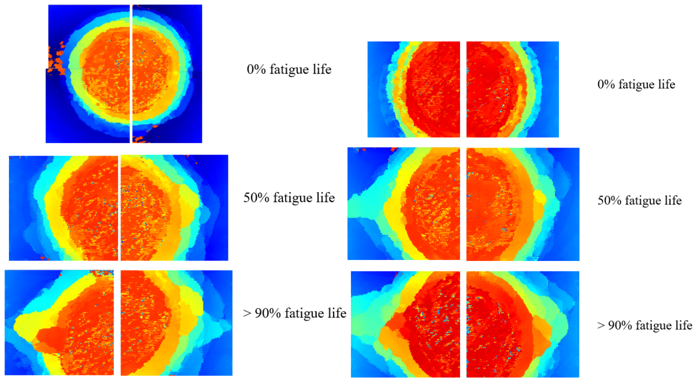

(a) specimen C-1, front face (b) specimen C-2, front face

Figure 3.5: Ultrasound scan at different stages of fatigue life in specimen C-1 and C-2. The results show the propagation of several delaminations at multiple depth locations, all in the perpendicular to the loading direction

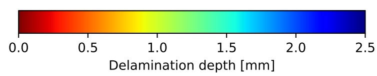

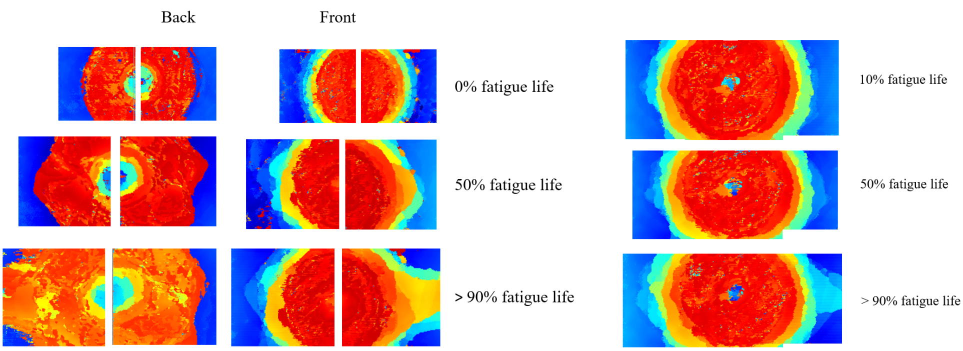

(a) specimen Ac-1 (b) specimen Anc-1, front face

Figure 3.6: Ultrasound scan at different stages of fatigue life in specimen Ac-1 and Anc-1. The results show the propagation of several delaminations at multiple depth locations in the case of specimen Ac-1 and the propagation of delaminations close to the back face in specimen Anc-1. Growth happened in the perpendicular to the loading direction.

Specimen Anc-1 exhibited distinct behavior compared to the other specimens when analyzing the combination of Ultrasound monitoring, DIC, and compliance curves. Firstly, its geometry differed; the central non-delaminated area had a consistent radius throughout the thickness. In contrast, in specimen Ac-1, PTFE inclusions presented a varying radius to form a central non-delaminated cone, while specimens C-1 and C-2 had circular PTFE inclusions without such a central cone. Consequently, this led to a unique local buckling deformation, even when compared to the more similar case of specimen Ac-1 (Figure 3.4). Following the buckling snap, both specimen Ac-1 and specimen Anc-1 displayed local buckling with an out-of-plane deformation opposite to the global buckling. While the entire specimens deformed towards the front face (global buckling), specific regions deformed towards the back face (local buckling). In specimen Anc-1, however, the maximum amplitude of displacement related to global buckling was situated in the central non-delaminated area, whereas in specimen Ac-1, it was in the external area surrounding the local buckle. This distinct configuration resulted in a different growth pattern in specimen Anc-1, where preferential delamination growth close to the back face was observed. In all other specimens, delamination grew simultaneously at multiple interfaces and depth positions. This different behavior led to a longer lifespan and a different increase in compliance during fatigue (Figure 3.2). In specimen Anc-1, compliance reached a higher value compared to all other tested specimens before triggering instability and failure and was characterized by a higher increase in axial compliance per cycle.

3.3.4 Fatigue delamination growth; comparison between CFAI and PTFE test

A comparison between the delamination growth patterns in CAI and in the PTFE tests is now presented. The first difference between the PTFE and CAI fatigue tests concerns the trends in the evolution of fatigue damage growth. In short-life CAI fatigue, it was observed that progressive growth of delamination was accompanied by progressive loss of axial stiffness. In long-life fatigue, a phase of no delamination growth and no axial stiffness degradation was followed by a phase of increase in delamination and loss of axial stiffness. This led the author to propose a threshold for the growth of CAI delamination which was regulating the presence of a plateau phase. In the surrogate test instead, this phenomenon was not observed and both short-life and long-life fatigue tests showed a gradual growth of delamination and increase in compliance.

Though seemingly inconsistent, this result aligns with the concept of the delamination growth threshold introduced in Chapter 2. In the case of PTFE tests, the load was selected to achieve a buckling snap and detachment of the PTFE inclusions. The snap was a fast and dynamic phenomenon that determined the initial growth of delamination by a small amount. For instance, in specimen C-2, where the snap was not immediate (see Figure 3.2), compliance remained constant before the snap, followed by a gradual increase. This observation parallels what happens in CAI long-life fatigue tests, where a first phase characterized by little stiffness degradation preceded the onset of delamination growth.

In all tests, delamination consistently grew perpendicular to the loading axis. This happened despite all the differences between the surrogate and the impact damage. In both CAI tests and PTFE tests, this growth was accompanied by the expansion of an oval local buckling shape. In the author's opinion, this macroscopic aspect of delamination growth, which was captured in the PTFE test, is likely to be dependent on the similarity in loading condition and fixture between the surrogate and the impact test.

While in CAI fatigue tests delamination grew initially from shallow depths, in PTFE instead, the growth started at different interfaces of the laminates both in larger and smaller delaminations. To explain those differences, it must be considered that, although an effort was made to reproduce the impact damage situation, several differences persisted and could not be avoided due to the limitations in the manufacturing process. The adopted shapes (circular and annular), did not perfectly represent the double triangular shape and transverse cracks usually observed in impact damage (Figure (1.4)). The specimen with the PTFE insert also missed the initial impact dent acting as an initial imperfection and determining the global buckling direction.

An additional difference concerns the growth in the central non delaminated cone. In the CAI fatigue tests presented in Chapter 2, delamination growth in the central cone took place. In the surrogate tests instead, this phenomenon did not happen in specimen Anc-1, while in specimen Ac-1 was not observable due to the lack of resolution of the inspection. Regarding this discrepant growth pattern between the surrogate and the CFAI test, some considerations can be made. In CAI fatigue tests, even if the central area presented no delaminations after the impact, other types of undetected damage cannot be excluded. This differs from the PTFE tests, in which the central area was purposely manufactured to have no damage. A second aspect is that in the CFAI test, an impact dent was present in the central area, a feature not represented in the surrogate tests. Finally, delamination internal fronts differ in the two cases, as in the surrogate tests they appear circular, whereas in the compression after impact tests they exhibit triangular shapes and straight internal fronts (see Figure 1.4). While all these differences could potentially be responsible for the lack of growth in the central cone in the surrogate tests, it's challenging to pinpoint a single determining factor.

Once the delamination started growing, however, the ultrasound inspection of advanced CAI and PTFE surrogates fatigue showed a similar phenomenon i.e. the growth of multiple planar delaminations in the perpendicular to load direction.

Having established that in the PTFE tests the threshold for delamination growth was immediately exceeded after the buckling snap, there is still one difference to be discussed. While in CAI fatigue once the delamination started to grow it occupied a restricted window of time and led to the collapse in a few cycles, in the PTFE tests the growth occupied many more cycles and propagated by a larger amount reaching the lateral edges of the specimens. In other words in CAI fatigue tests delamination growth, once started, was unstable and rapid while in PTFE was more stable, slow and reached a larger dimension.

To explain why delamination propagated by a larger amount, we must consider how compression-induced collapse in laminate structures occurs. According to current research, compression after impact static failure is caused by the interaction of various failure phenomena like the unstable delamination propagation concurring with buckling of sublaminates [6], ply level fiber kinking in areas of compressive stress concentration [7], deepening of the impact dent under compression loading increasing bending stresses, reduced stiffness in the impact damage area causing stress concentration at the impact sides, asymmetries in the deformation under compression.

Due to the constraints in manufacturing, the PTFE inclusions test was characterized by circular or annular delamination shapes, which didn't reproduce exactly the impact damage. The laminate also had a lower thickness. This insert configuration resulted in a local buckling producing significant mode I opening at the delamination fronts, and relatively low applied compressive stresses compared to CAI fatigue tests. A a result of that in PTFE tests, while the delamination was growing at a constant rate in fatigue, the ply level stress wasn't high enough to trigger kinking and collapse. In the case of CAI fatigue instead, the growth happened at a higher compressive stress level. It is likely that in this case, a smaller amount of growth was necessary to trigger instabilities like compression kinking at the ply level and the collapse of the specimen. In PTFE tests, besides propagating a larger amount, delamination growth was also slower. Related to this, a difference that was noted is that in the surrogate tests, large mode one openings were present at shallow delamination fronts, and were absent in CFAI test.

In the author's opinion, the observation of a slow stable delamination growth in the surrogate PTFE tests has a consequence on the damage tolerance design of CFRP structures. In the introduction section 1, it was explained that, since in CAI fatigue designers cannot prove a slow stable, and predictable growth, the no-growth design approach is adopted. The results presented in Chapter 2, seem to indicate that there is no room for the application of slow growth. In fact, in the long/life CFAI test, for a large period of time the growth could not be measured. Once the growth started, it happened in a fast and unstable manner, leading to failure in a short time. If only this result is considered, it could be concluded that 'slow' and 'stable' growth never happens in fatigue after impact of CFRP.

Thanks to the PTFE surrogate tests, however, it was observed how, under certain conditions, a slow stable growth of multiple planar deaminations is possible in compression fatigue loading. The main differences between the impacted case and the surrogates were a lower ply level axial stress and a buckling mode allowing for larger mode I opening at delamination fronts, together with some differences in the initial damage configurations reported in the previous sections. Despite the initial differences, once delamination growth started it looked similar to the CAI case. In both cases, the growth of multiple planar delaminations in the transverse direction was observed. However, in the surrogate tests, the growth was a slow and gradual propagation. Although the observation of slow growth derives from a surrogate test, it represents a damage propagation scenario that in principle cannot be excluded in CAI fatigue of some applications.

There were differences in the initial damage state, like the initial shape of delaminations, the presence of transverse shear matrix cracks and the lack of impact indentation. In an advanced state of delamination propagation however in both cases the growth of multiple delaminations towards the lateral edges of the specimen under the action of compression fatigue was observed. Why would delamination grow slowly and progressively in this case while fast and unstable in the CAI coupon tests? Besides the differences in the initial configuration, two big differences were present relevant during the propagation, namely a larger mode I opening at delamination fronts and a lower compressive stress within the plies. These conditions cannot be excluded a priori in a post-impact scenario of a structure that is different from standard CAI specimen. Results from CAI coupon tests cannot be generalized for many reasons, for example, the out of plane bending is limited by the lateral guides. There is also intrinsic variability of initial impact damage shape. Different damage envelopes and local buckling configurations are possible maybe promoting more mode I. With this, the author is not claiming that an actual impact damage will behave as the surrogate. Slow growth behavior however should not be excluded based on coupon tests since: a) there is an experimental case of slow growth in compression buckling-driven delamination fatigue propagation b) there is a big difference between the coupon test and many structures hence a larger mode I contribution and different ply-level stresses are in principle possible in CAI cases.

For example, it is unclear if, in the hypothetical case of an aeronautical panel larger than the CAI specimen (100x150 mm) and with different layup and thickness and constraints producing local buckling with large mode one opening, a slow or a fast unstable propagation has to be expected. To determine this, further investigation has to be performed, focusing on the differences between the surrogate PTFE test presented in this Chapter and the CFAI tests of Chapter 2.

3.4 Conclusions

A surrogate impact delamination envelope was manufactured using PTFE inserts and tested under fatigue. The manufacturing approach resulted in a satisfactory alignment of PTFE inserts which detached in fatigue and produced local buckling. The test revealed that the edges of the PTFE inserts constituted an initiation site for delamination growth. As expected in compression loading, a local buckling matching the area of initial PTFE inserts was observed after the snap. From a macroscopic preliminary analysis, the fatigue progression and final failure looked similar to CAI fatigue. Delamination and local buckles progressed the perpendicular to load direction.

A more detailed analysis, however, revealed some qualitative differences compared to the CAI fatigue. Those differences were mainly the position in depth of delamination growth, different local buckling configurations compatible with large mode I opening at delamination fronts and lower ply stress in the surrogate compared to the CAI tests in Chapter 2.

Despite the limitations, the fatigue growth of multiple planar delaminations was obtained in fatigue in conditions similar to CAI tests. The growth of those delaminations, in opposition to fatigue after impact cases, proved to be slow and stable. The PTFE test results suggest that it is possible to observe a slow growth of multiple planar delaminations in compression fatigue. This represents a damage propagation scenario that is possible in fatigue after impact, i.e. the propagation of multiple delaminations in compression fatigue with large mode I opening. The potential for a slow growth behavior also in certain cases of CAI fatigue cannot be excluded. Further investigations are needed to explain what determines the onset of a slow and stable delamination propagation in the surrogate test with PTFE inclusions reported in this chapter and on the contrary a fast unstable behavior in the CAI fatigue coupon tests reported in chapter 2. This further investigation should also consider cases representative of real structures like larger panels with smaller impact damage.

REFERENCES

[1] Wenran Gong, Jinlong Chen, and Eann A Patterson. Buckling and delamination growth behaviour of delaminated composite panels subject to four-point bending. *Composite Structures*, 138:122–133, 2016.

[2] Javier Paz, Antonio Raimondo, and Chiara Bisagni. Experimental study of post-buckled single-stringer composite specimens under fatigue loads with different load levels and load ratios. *Composites Part B: Engineering*, 255:110606, 2023.

[3] RJ Chester and G Clark. Modelling of impact damage features in graphite/epoxy laminates. In *Damage Detection in Composite Materials*. ASTM International, 1992.

[4] Moustafa Kinawy. *Static and fatigue propagation of buckle-driven delaminations under bending and compressive loads*. PhD thesis, University of Bath, 2011.

[5] A. Raimondo, S.A. Doesburg, and C. Bisagni. Numerical study of quasi-static and fatigue delamination growth in a post-buckled composite stiffened panel. *Composites Part B: Engineering*, 182:107589, 2020.

[6] D. J. Bull, S. M. Spearing, and I. Sinclair. Observations of damage development from compression-after-impact experiments using ex situ micro-focus computed tomography. *Composites Science and Technology*, 97:106–114, 2014.

[7] Alan Tate Nettles and Luke Scharber. The influence of gi and gii on the compression after impact strength of carbon fiber/epoxy laminates. *Journal of Composite Materials*, 52(8):991–1003, 2018.

4

Understanding aspects of impact delamination growth

By analyzing the strain energy release rate profiles it is possible to study the effects on CFAI delamination growth of adopting different fixtures, different loading, and different impact damage configurations.

A hypothesis is formulated suggesting that delaminations in CAI fatigue tests may grow in the transverse direction due to the influence of unidirectional loading and the formation of an elliptical buckle.

Furthermore, the analysis suggests that a more enhanced global buckling promotes the growth of a single delamination. Finally, the inward growth in the non-delaminated impact cone may depend on the size of the non-delaminated central area generated during the impact.

4.1 Understanding impact delamination fatigue

In the previous chapters, fatigue after impact was investigated in detail, focusing in particular on the growth of planar delamination. In Chapter 2 an updated and advanced description of CFAI delamination growth was provided, highlighting some technical challenges associated with the monitoring techniques. In Chapter 3 instead, PTFE inclusions were used to produce a surrogate of impact damage and test it in fatigue. This test allowed to study planar delamination growth in a more controlled test. Interestingly it was observed that, under certain conditions, slow growth of planar delamination is happening. It's still unclear however how dependent the obtained delamination growth patterns are on the boundary conditions of the test and different configurations of impact damage. In other words how general are the results? Are the tests representative of real structures? What differences could we expect if the geometry of impact damage is changed?

A model was developed to study the effect of different initial damage configurations in different loading and constraint scenarios. For this reason, a numerical approach was selected to respect two requirements:

- parametrized initial damage geometry
- low computational cost

To study the sensitivity of CAI fatigue on the different loading and impact damage configurations, multiple analyses are necessary. Modeling fatigue damage propagation in CFRP is a complex problem and requires significant computational resources. In addition to that, the CAI fatigue problem is characterized by multiple crack fronts. After exploring the possible approaches (cohesive elements and VCCT) it was decided to not perform crack propagation simulations because they are too computationally expensive and not suited to perform a parametric study with multiple damage configurations. It was also observed that analyzing a full delamination propagation was not strictly necessary to answer the questions under investigation.

Instead of analyzing damage propagation then, a criterion based on strain energy release rate profiles was used to evaluate the most probable starting point of delamination propagation. This was done by virtual crack closure technique (VCCT) analysis with suppressed propagation. The model was validated using the PTFE test results presented in the previous chapter. After validation, the effect of different boundary conditions and different initial delamination shapes was investigated. Before presenting and discussing the result of the analysis, in the following section concepts of the theory of fracture mechanics and the VCCT are introduced to provide a theoretical background to the reader.

4.2 Energy approach to fracture

The propagation of a crack implies generating a free surface in a solid material. In this process, energy is used to break molecular bonds. The required energy can be expressed with surface energy multiplied by the newly created surface area. This is sufficient in the case of linear elastic behavior of brittle materials. In case of significant plastic crack tip deformation instead, an energy surplus has to be added. This is usually expressed as an additional term to the required energy to open the unit area of the crack [1].

Consequent to crack propagation, the potential elastic energy stored in the material decreases. This is because, as the crack grows the strain redistributes, releasing strain energy from the portion of material left behind the advancing crack.

Considering the above, the energy balance in a mechanical system composed of a material loaded with external work undergoing a crack increment of length da, with fixed grips and quasi-static loading conditions, can be expressed as follows [2].

4

$$\frac{dF}{da} - \frac{dU}{da} = \frac{dW}{da} + \frac{dE_k}{da} \tag{4.1}$$

In this equation, F is the external work, U is the strain energy, W is the surface energy and E_k is the kinetic energy. The present work deals with the case of brittle materials, hence the term W includes the surface energy without the plasticity term. The kinetic energy is also supposed not to vary as the crack extends. Considering this, the energy balance can be written as:

$$G = \frac{d(F-U)}{da} = \frac{dW}{da} \tag{4.2}$$

The left term of the equation containing the external work and strain release is usually expressed with a single term G, the strain energy release rate (SERR). The SERR is in fact the *total decrease in potential energy per unit area of new crack*.

Griffith stated his famous stability criterion from this energy balance [3]. If G exceeds a threshold value, which is material dependent and defined in the right term of equation 4.2, then an unstable growth of crack happens. This value is usually defined as fracture toughness or G_c, and the necessary condition for growth is $G \geq G_c$.

Deriving the value of G_c experimentally is challenging since complex stress states are possible at the crack tip. For simplification, three special cases have been adopted in the past to describe the fracture behavior (figure 4.1). Mode I fracture involves crack opening induced by tensile loading. Mode II fracture entails sliding caused by in-plane shear load. Mode III fracture refers to tearing caused by out-of-plane shear load. Specific tests can be designed to derive the G_c in the different opening modes. In many cases, however, the crack tip undergoes a complex 3d stress state and fractures often involve a combination of these modes.

Linear elastic fracture mechanics (LEFM) theory was created to deal with quasi-static fracture, but some concepts were later applied to fatigue problems. Interestingly, in the case of fatigue, growth is observed for $G \leq G_c$. To estimate the growth rate Paris et al. [4–6] proposed the relationship:

$$\frac{da}{dN} = C\Delta K^n \tag{4.3}$$

relating the crack growth $\frac{da}{dN}$ to the stress intensity factor range $\Delta K = K_{max} - K_{min}$, locally defined at the crack tip, using a power law with constant C and exponent n. Thanks to the contributions by Irving [7], it is known that the stress intensity factor K can be related to the strain energy release rate G in the following way:

$$\begin{cases} G = \frac{K^2}{E} & \text{if plane stress} \\ G = \frac{K^2(1-\upsilon^2)}{E} & \text{if plane strain} \end{cases} \tag{4.4}$$

With E representing Young's modulus and υ the Poisson ratio. This means that the Paris relationship can be conversely written using the stress intensity factor range (ΔK) or similitude parameters derived from the SERR. The discussion about which similitude parameter should be adopted for estimating crack growth rate, although interesting, is out of the scope of the present work. Further information can be found in the work by Pascoe [8].

Going back to the original definition, SERR was defined as the total decrease in potential energy per unit crack area created, assuming quasi-static loading and fixed grips. In the case of multiple 2D delaminations under compression like impact damage, if a mesoscale analysis is performed, different SERR values are expected along the crack fronts. This is because the stress states at the delamination fronts vary depending on the buckling configuration which depends on fiber orientation and initial damage geometry. For example, local buckling could cause one delamination to have an enhanced mode I opening while closing other delaminations. Having high values of the maximum SERR in fatigue in a specific area of the delamination front, surrounded by low SERR indicates that a crack is more likely to grow where the high SERR is, assuming that the resistance opposed by the material is similar. One limitation of this approach is that it does not consider that different fiber orientations of upper and lower ply result in different micro-scale fracture mechanisms and on a different resistance opposed to delamination propagation. However, as will be shown later, in the case of quasi-isotropic laminates under compression, with delamination situated in each interface, a simple meso-scale analysis provides an intuitive insight into some aspects of delamination propagation in fatigue.

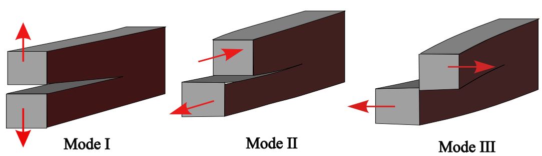

Figure 4.1: Schematic of the fracture modes

4.3 The virtual crack closure technique

In the previous section the importance of the SERR value was discussed. However, how to determine the SERR in practice, especially in the case of a 2D complex crack front like the ones presented in the previous chapters?

The components of the energy release rate can be numerically obtained using the virtual crack closure technique (VCCT) introduced by Rybicki and Kanninen [9]. In VCCT, the energy release rate is determined by evaluating the energy per unit area required to close a small increment of crack length. The individual components of the energy release rate can be calculated using the following equations:

$$G_I = \frac{1}{2b\,da} F_y \left(v - v' \right) \tag{4.5}$$

$$G_{II} = \frac{1}{2b\,da} F_x \left(u - u' \right) \tag{4.6}$$

where b is the width, da is the increment in crack length, F_X and F_y are the nodal force components at an intact node, and u,u',v,v' are the nodal displacement components in the second run after the nodes are released. If the mesh is fine enough, good estimates can be obtained by using the separations u,u',v,v' at the first debonded nodes of the same solution (figure 4.2). The VCCT can be easily extended to three dimensions and has been implemented in commercial FE software.

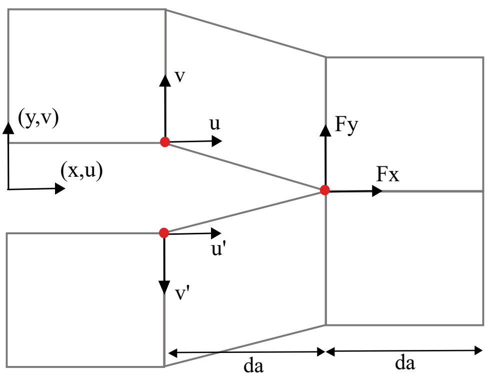

Figure 4.2: The VCCT technique schematic

4.4 Modelling approach

To study different delamination configurations in CFRP an Abaqus CAE parametric model was created via Python scripts. This allowed in the subsequent analysis to insert a desired layup, initial delamination geometry and boundary condition and generate multiple models in a short time. The structure of the model is summarized in figure 4.3.

The individual plies are represented using SC8R shell elements, which are 8-node quadrilateral in-plane general-purpose continuum shells with reduced integration and hourglass control, incorporating finite membrane strains. Each ply within the laminate is treated as a distinct part, employing shell elements with anisotropic properties specific to each ply. The mesh for each ply consists of a single element per thickness.

In the assembly, all plies are stacked together, and interaction properties are assigned to distinct regions. Outside the region of interest, a tie constraint is enforced between adjacent surfaces of different plies, facilitated by coincident nodes in the mesh. This tie constraint is implemented since no delamination is expected in that area.

To obtain a circular delamination, the VCCT interaction is imposed in an area that includes the desired crack front. Then a circular set of nodes, having the radius of delamination is defined as a disconnected area of the VCCT. In this way, the crack front is defined.

In the central area, the plies are delaminated and can be considered as separate entities. They still have to respect a non-penetration condition. This is imposed by applying a normal interaction between adjacent surfaces.

The same modeling strategy is adopted in case of the presence of a central non-delaminated area and annular delamination. The only difference is that now a circular area of tie constraint is added in the center of the interface. Dynamic implicit solver of Abaqus CAE was used, with full-Newton increment. Non-linear geometry option was imposed.

The goal of the model is to observe the effect of specific features of impact damage on the initial growth of delamination. In this case, there is no interest in simulating the propagation of cracks, this would only increase the computational time. To suppress propagation, a high G_{th} can be imposed (in this case 6000 J/m^2). The described model is used to analyze the stress state at the maximum compression fatigue load, derive the SERR at the delamination front at this applied load (G_{max}), and compare it in the different interfaces of the model.

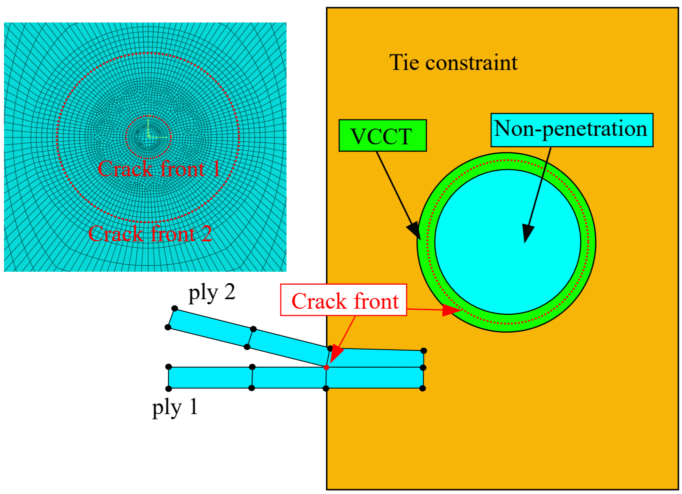

Figure 4.3: Scheme of the modeling approach adopted for the interfaces between plies and mesh in case of circular and annular delamination

4.5 Validation of the results

The numerical model was validated using the PTFE inclusion test whose results were presented in Chapter 3. The geometry of specimens C-1 and C-2 (shown in the previous methodology section of Chapter 3) were reproduced and simulated using the numerical model. Similar max to min in plane y displacement in the back surface of the specimen were used to compare the test with the simulation. With back face is intended the face where the larger delaminations are (which would be the opposite to impact face in a real impact damage cone). This choice was made because in both test and simulation, this surface was the relevant one to be compared. In both the simulations and numerical model the overall out of plane deformation of the specimen pointed towards the front face, while locally in the center a positive out of plane displacement was present in the opposite direction pointing towards the back face. This is visible from figure 4.4. The shape of this central area matches. Of course this only give indication of the first ply next to the back face and not about the buckling of all the sublaminates. It is interesting to observe that both in simulation and numerical plots, there is an asymmetry of the central local buckle, which can be explained considering that the first ply in the layup had a 45-degree orientation.

The strain energy release rate profiles at the maximum compression load in fatigue are shown in Figure 4.5. This three-dimensional plot illustrates the distribution of strain energy release rates across various interfaces within the layup. The x and y coordinates of the plot align with the specimen axis, where x = 0 and y = 0 represent the central coordinates of the specimen, and the y-axis indicates the loading direction. The interfaces are superimposed on each other, with the back face of the laminate placed at the top for enhanced visibility. In accordance with the previous chapter showing the experimental results, with the back face, we refer to the interface containing the larger PTFE circles. This arrangement aids in distinguishing variations in strain energy release rates in different interfaces at the same time. The results from figure 4.5 clearly indicate that the higher strain energy release rates occur in the transverse direction (perpendicular to the load). This happens both for mode I and mode II. The maximum strain energy release rates are observed in the last two interfaces close to the back face and gradually decrease progressing towards the front face. This observation can be justified by observing that the buckling of sublaminates regarded mostly the plies close to the back face both in experiments and numerical results. The maximum strain energy release rates observed match the location in which delamination growth was observed using ultrasound in specimens C-1 and C-2 (Chapter 3). This suggests that the adopted method can provide valuable indications on the location in which delamination growth is more likely to start.

4

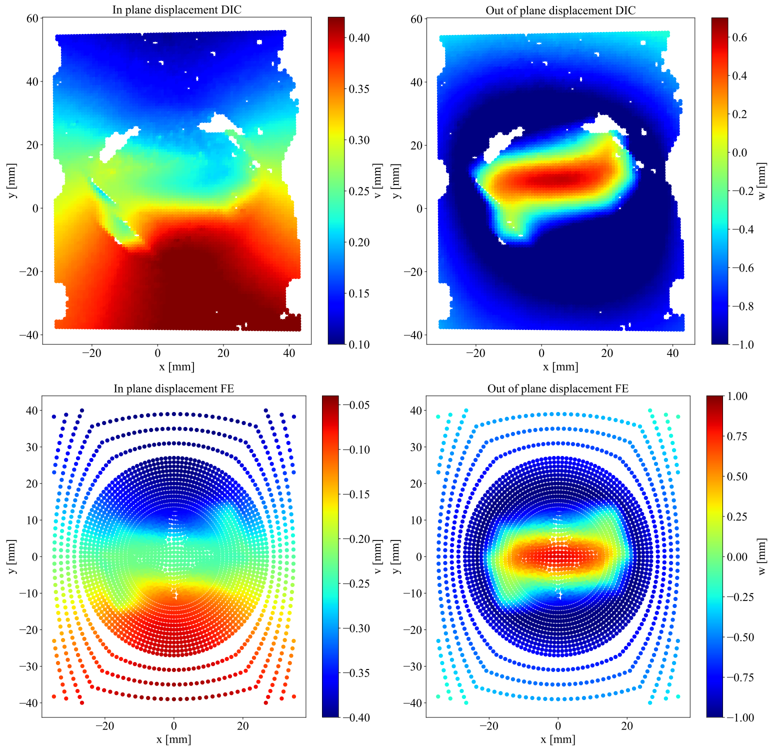

Figure 4.4: Comparison of DIC surface displacement in specimen c-2 (top images) and FE simulations (bottom images). Left side of the figure compares in-plane displacement while right side of the image compares out of plane displacements.

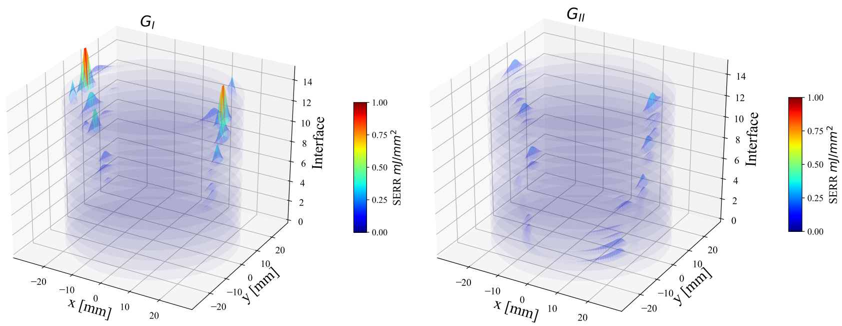

Figure 4.5: Distribution of strain energy release rates G_{max} across various interfaces within the layup. Each circular surface in transparent blue, represents a VCCT interaction zone (Figure 4.3) modelling one interface. The x and y coordinates of the plot align with the specimen axis, where x = 0 and y = 0 represent the central coordinates of the specimen, and the y-axis indicates the loading direction. The interfaces are superimposed on each other, with the back face of the laminate (where larger delaminations are) placed at the top for enhanced visibility.

4.6 Growth of delamination perpendicular to loading; effect of loading direction

The numerical analysis presented in the previous section provides insight into a pattern commonly observed in CAI fatigue tests. In Chapter 2, CFAI delamination was noted to propagate perpendicular to the loading axis. This identical pattern recurred in Chapter 3 during the PTFE inclusion test. In both CFAI and PTFE tests, an elliptical buckling shape expanded perpendicular to the loading direction as delamination progressed.

To explain this phenomenon, the analysis representing the geometry of the PTFE test, whose results were validated in the previous section, can be utilized. Figure 4.6 shows the interface where the highest SERR are present. A buckling elongated perpendicular to the load can be observed in the upper ply adjacent to the interface. The values of the Strain Energy Release Rate ($G_I + G_{II}$) are higher when the delamination front (red dots) overlaps the local buckling limits. This phenomenon can be easily explained in the case of mode I, since SERR is maximum if the buckling front coincides with the delamination front and the opening displacement is maximum. Quite interestingly maximum SERR values in mode II are also observed where the delamination front coincided with local buckling fronts. This happens also in all other interfaces of the laminate.

The test analyzed does not exactly represent the situation of impact damage, since many differences are present between the PTFE surrogate tests and the CFAI test, as discussed in Chapter 3. In impact cases, delamination tends to have a circular projected area since during impact, damage spreads equally in all directions from the impact point. Also in case of impact damage, the subsequent loading is unidirectional and forces an oval buckling shape elongated perpendicular to the load direction. Given that the buckling is elongated perpendicular to the loading direction, the maximum SERR values are likely to be located at the lateral edges of the delamination, like in case of Figure 4.6. Thus, transverse growth in CFAI tests can be justified with a similar reasoning. Previous chapters have shown that as the delamination propagates, the buckle elongates in the transverse direction and becomes more oval. This indicates that as the delamination grows perpendicular to the load direction, the described phenomenon becomes increasingly pronounced. Indeed, as a consequence of the change in buckling shape, the area of overlap between the delamination front and the buckling front becomes narrower as the crack grows in the transverse direction.

The buckling front coinciding with the delamination front was previously used by Melin et al. [10, 11] to explain the initial growth of short delaminations in fatigue after impact. However, this hypothesis was not supported by numerical evidence and was not used to explain the growth perpendicular to the loading direction. The explanation proposed here clarifies why growth in the CAI standard test fixture always occurs perpendicular to the load direction and suggests that this pattern of delamination growth could change if a multi-directional loading were applied.

It must be noted here that although supported by the preliminary numerical analysis, this hypothesis has to be further validated. In fact, as introduced in Chapter2, buckling is not the only possible mechanism triggering delamination growth. Transverse cracks in superficial plies could trigger the propagation of delaminations in adjacent interfaces.

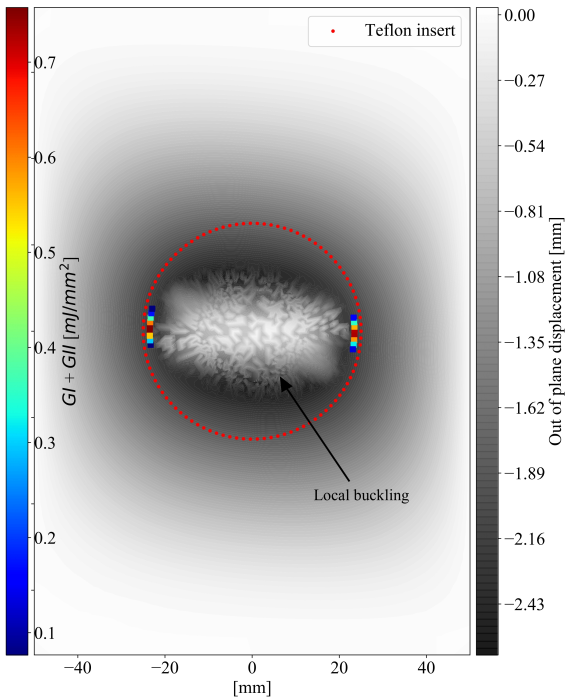

Figure 4.6: Buckling area matching SERR profiles. In color, the maximum SERR G_{max} values in the penultimate interface (where the higher values were observed). In the gray scale, the magnitude of out of plane displacement of the upper ply to this specific interface shows an elliptical local buckle. The red dotted circle represents the initial PTFE inclusion, i.e. delamination front in the model. Maximum SERR is where the buckling front and delamination front coincide.

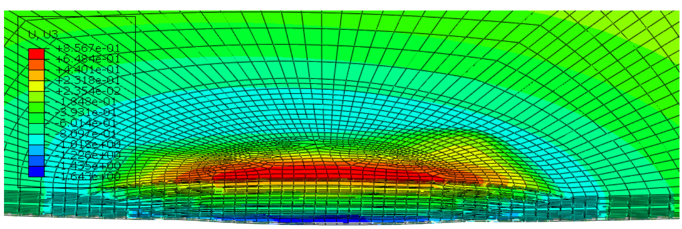

Figure 4.7: A cut section of the deformed laminate is shown. The section is cut in the x direction (perpendicular to loading) from the center point. It shows the sub laminates opening in the out of plane direction. The back face is placed on top in the figure to better show the larger delaminations.

4.7 Effect of global buckling configuration; is the test representing real structures?

In CAI static tests [12], a setup that forces the local buckling is adopted. This setup was also adopted in the majority of fatigue after-impact tests available in the literature. In many applications, however, like larger panels subjected to small impact damage, a more pronounced global buckling is likely to happen. This fact made the community often question the scalability of compression after impact tests. In fact, the ASTM standard [12] for static CAI tests clearly states that the test is not meant to be scalable. To certify large structures, full-scale tests are often required. To investigate how sensitive the fatigue propagation of impact delamination is to the buckling configuration, two scenarios are compared.

In addition to the result presented in the previous section, a simulation without lateral edges has been conducted to represent a situation of enhanced global buckling. As shown in figure 4.9, the removal of lateral edges produces a global buckling generating larger overall out-of-plane displacements, but still, a portion of local buckling of sub-laminates can be observed.

Figure 4.8 presents the SERR profiles in the two conditions. Interestingly, the transverse direction is where the highest values are observed also in case no anti-buckling lateral guide is used. This should not surprise the reader, since the local buckling, even if small, is still present and elongated in the transverse to the loading direction. Interestingly, in the case of no anti-buckling guide, the SERR values are higher in one single interface. In case the anti-buckling guide is active and the global buckling is restricted, higher values of SERR are observed in multiple interfaces internal to the laminate.

This observation has important implications. According to this result, a structure with circular planar delaminations located in multiple interfaces, in case of large global buckling is more likely to promote the growth of a delamination placed in a single interface. This is because of the particular configuration of global and local buckling that promotes the opening of one single interface in case of free buckling and of multiple interfaces in case of restrained global buckling.

It must be noted that the presented approach has some limitations. As anticipated, the initial damage examined has some differences compared to the CAI fatigue case, which is the presence of the dent, the complex shape of individual delaminations not exactly represented and transverse matrix cracks not present in the model. A second aspect is that only the initial stress states of impact damage are used in the current investigation, meaning that the growth of delamination is not evaluated. As one delamination propagates, the buckling profile is likely to change, changing the SERR values in other delaminations as well. This effect is not considered.

Despite the limitations, this study case can be used to represent, to some extent, a possible configuration of impact damage. If the analysis is considered as such, it reveals one mechanism that has to be investigated before scaling the results of CAI fatigue tests. The results suggest that single delamination is more likely to grow in more enhanced global buckling conditions.

This also has important implications for ultrasound inspection interpretation. As

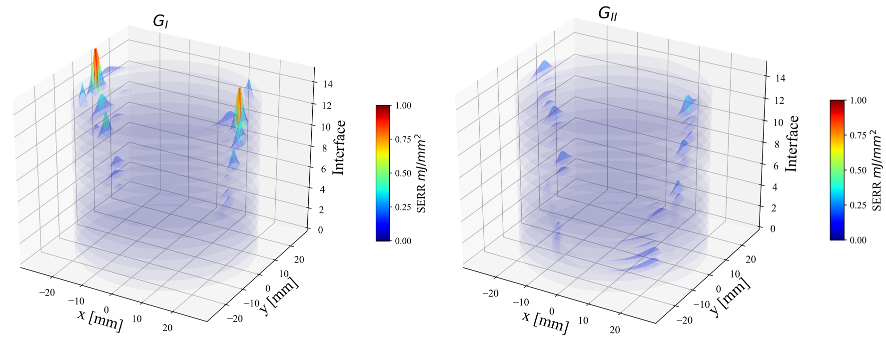

(a) Anti-buckling guide

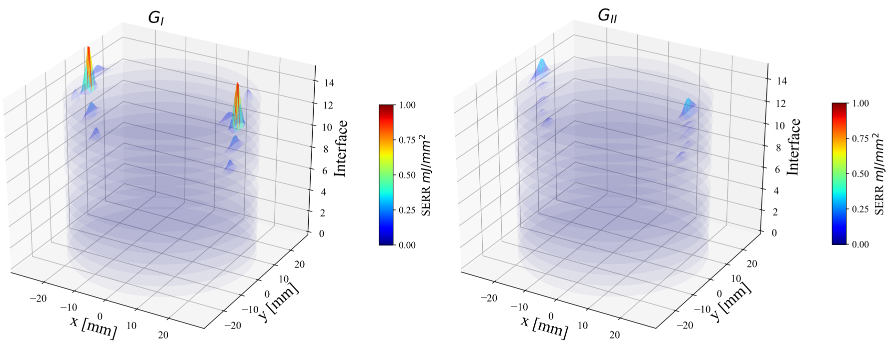

(b) No anti-buckling guide

Figure 4.8: Distribution of strain energy release rates G_{max} across various interfaces within the layup. Each circular surface in transparent blue represents a VCCT interaction zone (Figure 4.3) modeling one interface. The x and y coordinates of the plot align with the specimen axis, where x = 0 and y = 0 represent the central coordinates of the specimen, and the y-axis indicates the loading direction. The side with larger delamination is placed on top for enhanced visibility.

previously explained, the current inspection procedures evaluate the propagation of the delamination projected area. In the case of multiple delaminations or single delamination growth, the same increase of projected area corresponds to a largely different increase in the total delaminated area.

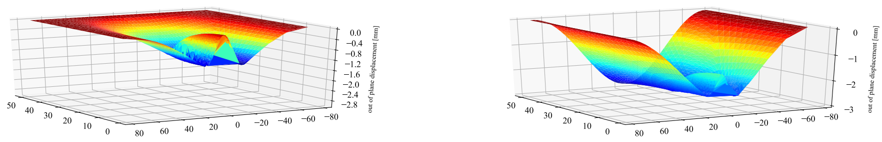

(a) simulation with anti-buckling guide

(b) simulation without anti-buckling guide

Figure 4.9: FE out of plane displacement with and without restrained buckling

4.8 Effect of the size of the central non-delaminated area

In the previous chapters, the presence of a central non-delaminated cone in Barely Visible Impact Damage (BVID) was shown with ultrasound inspections. As explained in the introduction of this thesis, this central non-delaminated cone can be attributed to the out-of-plane compression stress originating during contact with the impactor, which prevents the growth of delamination in this specific area. The preferential initial growth of delamination in this area was observed using a through-thickness transmission scan in CAI fatigue tests and was reported in Chapter 2. A PTFE inclusion test was conducted to observe this feature in more detail. However, this phenomenon was not observed, likely due to fundamental differences between impact delamination and the surrogate (Chapter 3).

At this point, one may think that studying the influence of this central area on fatigue growth is purely academic. However, the presence of this central cone affects the local buckling of the laminate, as suggested by Bull et al. [13]. Since the presence of the central non-delaminated area is linked to contact stress, different impact conditions would likely cause different sizes of the central non-delaminated area. In the study by Mitevsky et al. [14], different impactor radii were adopted in the impact test, and the resulting damage was compared. In this case, it was not possible to detect a central non-delaminated area due to the presence of the impact dent and the deflections of ultrasounds from the curved surface. However, decreasing the impact radius resulted in a reduced impact dent size, proving a different distribution of contact stresses during impact. Since the non-delaminated central cone is linked to the contact stress, in principle, a range of sizes of this central non-delaminated area is possible if the impactor geometrical parameters are changed.

To investigate this issue, a parametric analysis was conducted, comparing annular delamination envelopes with different internal radii. The geometry of the delamination envelope and specimens is the same as specimen Anc-1 (Chapter 3), except for the internal radius of the non-delaminated area. Three values are used: $r = 2$ mm, $r = 5$ mm, $r = 7$ mm. Figures 4.12, 4.11, 4.10 show the SERR profiles in the different cases. Accumulation of mode I SERR in the internal fronts was not observed in any of the cases. Interestingly, mode II SERR in the internal front of the annular delamination seems to become more relevant as the radius of the central non-delaminated cone decreases. This suggests that smaller non-delaminated central areas may have a higher chance of experiencing delamination growth. Even if growth was not observed in the central area in the PTFE test, it is possible that utilizing a smaller internal radius would make it possible to observe inward growth in the PTFE surrogate tests.

It must be noted that the presented analysis has some limitations. The damage represented differs from impact damage in several ways. First, the impact dent is not modeled. Second, the complex shape of irregular delamination edges is not represented. Finally, transverse matrix cracks, which often bound impact delamination, are not present in the model. In the author's view, these effects must be carefully considered before translating the results from this analysis to actual fatigue after impact tests.

Having considered the above limitations, this investigation still provides insight into an effect that was not investigated or highlighted by previous research. The size of the central non-delaminated area may influence how delamination propagates in fatigue. In the LVI test standard [15], a hemispherical impactor of a fixed radius is prescribed. In fatigue after-impact experiments from the literature, this approach was often followed as well. However, in real structures, various sources of impact are possible, all resulting in different damage and different internal radii. The proposed numerical investigation suggests a mechanism in which the impactor radius may influence the internal non-delaminated area which then may change the way delamination grows in fatigue.

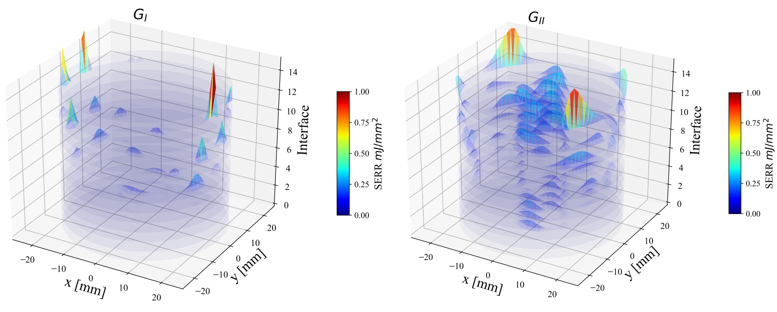

(a) Mode I SERR (b) Mode II SERR

Figure 4.10: G_{max} profile in case internal non-delaminated area radius = 7 mm. Each circular surface in transparent blue represents a VCCT interaction zone (Figure 4.3) modeling one interface. The x and y coordinates of the plot align with the specimen axis, where x = 0 and y = 0 represent the central coordinates of the specimen, and the y-axis indicates the loading direction. The side with larger delamination is placed on top for enhanced visibility.

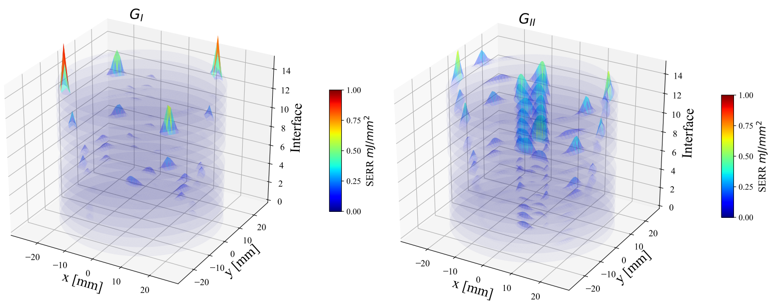

(a) Mode I SERR (b) Mode II SERR

Figure 4.11: G_{max} profile in case internal non-delaminated area radius = 5 mm. Each circular surface in transparent blue represents a VCCT interaction zone (Figure 4.3) modeling one interface. The x and y coordinates of the plot align with the specimen axis, where x = 0 and y = 0 represent the central coordinates of the specimen, and the y-axis indicates the loading direction. The side with larger delamination is placed on top for enhanced visibility.

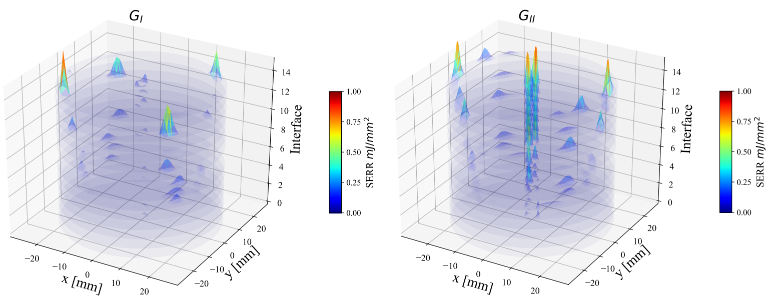

(a) Mode I SERR (b) Mode II SERR

Figure 4.12: G_{max} profile in case internal non-delaminated area radius = 2 mm. Each circular surface in transparent blue represents a VCCT interaction zone (Figure 4.3) modeling one interface. The x and y coordinates of the plot align with the specimen axis, where x = 0 and y = 0 represent the central coordinates of the specimen, and the y-axis indicates the loading direction. The side with larger delamination is placed on top for enhanced visibility.

4.9 Conclusions

A VCCT analysis with suppressed propagation was performed to investigate some aspects of delamination propagation. The model was validated using the PTFE inclusion test results presented in the previous chapter. The modeling approach captured the local buckling shape satisfactorily and provided a valuable indication of the starting point of delamination propagation in the PTFE surrogate tests. An investigation was then conducted analyzing different configurations of initial delamination and boundary conditions.

Based on the results of this investigation, it was hypothesized that the transverse growth of delamination in fatigue after impact could be caused by the overlapping of the local buckling front and delamination front in specific areas of the damage. Since the buckling front in CAI fatigue tests tends to be elliptically elongated in the transverse to the loading direction, as long as unidirectional loading is applied to a delamination envelope that can be approximated by a circle, growth is likely to start in the perpendicular to the load orientation.

Then an analysis was conducted to observe the effect of constraining global buckling on the same simplified impact damage representation. It was found that a state with global buckling without restrictions promotes the increase of SERR in a single interface. On the contrary, suppressed global buckling and enhanced local buckling produce high SERR in multiple interfaces of the same damage geometry. This observation has important implications since in many applications global buckling is not restrained.

Finally, it was observed that in the case of a central non-delaminated circular area, a reduction in the size of this area increases the mode *II* strain energy release rates in the internal front. This indicates that a smaller central non-delaminated area is more likely to face delamination growth compared to a large one. Being the radius of internal delamination linked to contact stress distribution, the results suggest a dependency between different impactor geometry and different patterns of delamination growth in fatigue.

References

[1] Egon Orowan. Fracture and strength of solids. *Reports on progress in physics*, 12(1):185, 1949.

[2] George R Irwin and JA Kies. Critical energy rate analysis of fracture strength. *Spie Milestone series MS*, 137:136–141, 1997.

[3] Alan Arnold Griffith. Vi. the phenomena of rupture and flow in solids. *Philosophical transactions of the royal society of london. Series A, containing papers of a mathematical or physical character*, 221(582-593):163–198, 1921.

[4] PC Paris, MP Gomez, and WE Anderson. A rational analytical theory of fatigue, the trend in engineering. *U. of Washington, Seattle, Wa*, 13(1), 1961.

[5] Paul Paris and Fazil Erdogan. A critical analysis of crack propagation laws. 1963.

[6] PC Paris. The fracture mechanics approach to fatigue, fatigue—an interdisciplinary approach, proceedings of the 10th sagamore army materials research conference, 1964.

4

[7] George R Irwin. Analysis of stresses and strains near the end of a crack traversing a plate. 1957.

[8] J A Pascoe, R C Alderliesten, and R Benedictus. Methods for the prediction of fatigue delamination growth in composites and adhesive bonds–a critical review. *Engineering Fracture Mechanics*, 112:72–96, 2013.

[9] Edmund F Rybicki and Melvin F Kanninen. A finite element calculation of stress intensity factors by a modified crack closure integral. *Engineering fracture mechanics*, 9(4):931–938, 1977.

[10] L. Gunnar Melin and Joakim Schön. Buckling behaviour and delamination growth in impacted composite specimens under fatigue load: An experimental study. *Composites Science and Technology*, 61:1841–1852, 2001.

[11] L. G. Melin, J. Schön, and T. Nyman. Fatigue testing and buckling characteristics of impacted composite specimens. *International Journal of Fatigue*, 24:263–272, 2002.

[12] Compass ASTM D7137 D7137M-17. Standard test method for compressive residual strength properties of damaged polymer matrix composite plates.

[13] D. J. Bull, S. M. Spearing, and I. Sinclair. Observations of damage development from compression-after-impact experiments using ex situ micro-focus computed tomography. *Composites Science and Technology*, 97:106–114, 2014.

[14] T. Mitrevski, I. H. Marshall, and R. Thomson. The influence of impactor shape on the damage to composite laminates. *Composite Structures*, 76:116–122, 2006.

[15] Compass ASTM D7136 D7136M-15. Standard test method for measuring the damage resistance of a fiber-reinforced polymer matrix composite to a drop-weight impact event.

5

Acoustic Emission damage mode separation

An experimental methodology to separate acoustic emission waveforms originating from specific damage modes occurring in compression after impact has been applied.

The continuum wavelet analysis of acoustic emission showed the presence of four waveform types, which were associated with matrix cracking, fiber-matrix debonding, a combination of matrix cracking and fiber-matrix debonding, and fiber failure.

Results show the impossibility of separating a delamination-type signal with the adopted method. It furthermore shows how the traditional damage descriptors fail to describe some of the individuated waveforms. Results of this chapter have been previously published in a journal article [1].

5.1 Acoustic emission monitoring

The research presented in the previous chapters has highlighted some critical areas, in the understanding of CAI fatigue. In Chapter 2, a combination of ultrasound scans and digital image correlation was used to monitor fatigue after impact in CFRP. Due to known limitations in the adopted monitoring strategies, however, a partial description of damage propagation was provided. Besides delamination, all other damage modes were excluded from the analysis. Even among delaminations, growth in shadowed areas was not detectable. Finally, no real-time information was available since the test had to be stopped to perform inspections. This technological gap becomes relevant especially if the compliance and delamination propagation observed in the CAI long-life fatigue test (Figures 2.16b) is considered. In this test, there was an initial phase in which no compliance degradation and no delamination growth was observed. What was happening during this phase? To investigate this matter, the remaining chapters of the manuscript focus on **acoustic emission** (AE) monitoring, a technique that allows sensing the formation of damage in real-time.

Acoustic emission (AE) monitoring is a passive, non-destructive technique used in structural health monitoring (SHM). When a sudden stress redistribution occurs inside a material, like in the case of the propagation of a crack, stress waves are generated. Elastic waves propagate inside the material, starting from the source location and eventually reaching the surface. In acoustic emission monitoring, surface vibrations are monitored using piezo-electric sensors, capable of detecting surface vibrations and converting them into signals. These signals are then usually magnified using pre-amplifiers. Signal analysis of the acoustic emission was performed with two main aims [2]: damage diagnostic, meaning the detailed characterization of damage, and damage prognostic which aims to estimate the remaining useful life and residual strength of the damaged structure. One interesting aspect of acoustic emissions is the capability to distinguish the different source mechanisms by analyzing the characteristics of the recorded signal. This becomes relevant in the case of composite materials, where multiple damage modes can be distinguished using this technique. Compared to delamination growth monitoring presented in the previous chapters, AE has two important advantages:

- real-time acquisition, i.e. no need to stop the test to perform the inspection;
- capability to detect other damage modes besides delamination, all without shadowing effect;

For this reason, it was decided to apply this technique to the monitoring of CAI fatigue, and in particular to separate damage modes and monitor their presence in fatigue after impact. This chapter focuses on the task of damage mode identification in CFRP by using acoustic emission activity. First, an introduction to the state of the art of acoustic emission signal analysis and the different strategies for damage mode separation is provided. Then an experimental campaign designed to isolate acoustic signals and associate them with the different damage modes is presented.

5.2 ACOUSTIC EMISSION WAVEFORM DESCRIPTORS

AE signals in CFRP usually appear as a burst of duration ~ 1 ms, releasing power in a frequency band between 10–1000 kHz. In many acquisition systems, an amplitude threshold is set (figure 5.1). Only the waveforms that exceed the threshold are saved and analyzed. To describe and characterize the waveforms, a series of parameters are usually derived. Those parameters are commonly called descriptors since they are meant to describe the signal. Descriptors can be derived in the time domain and the frequency domain.

The most used descriptors are listed in table 5.1 and shown visually in figure 5.1. Among the time domain descriptors peak amplitude, rise time, counts, duration, and energy (table 5.1) have often been used. If a fast Fourier transform (FFT) is performed, information can be extracted also in the frequency domain. Commonly adopted frequency-based descriptors are peak frequency, centroid frequency, average peak frequency, and partial powers (table 5.1).

The idea behind using AE descriptors in damage mode separation is that similar signals have a similar set of descriptors, hence descriptors can be used to create groups of similar signals. For this reason, as will be shown in the following sections, various sets of descriptors have been used as features for the clustering and classification of signals. Before that, in the next section, the wavelet transform is introduced as a superior tool for signal analysis.

	Descriptor	**Definition**
Time domain	Rise time (RT)	interval between the first threshold trespassing and the maximum amplitude [μs]
	Counts (C)	number of times the signal crosses the threshold in the increasing direction
	Max amplitude (A)	peak amplitude of the waveform
	Counts to peak (CP)	counts before maximum amplitude
	Duration (D)	interval between the first and last threshold trespassing [μs]
	Energy (E)	$\int_{-\infty}^{+\infty} \lvert x(t)\rvert^2 \, dt$; energy of the signal $x(t)$
Frequency domain	Peak frequency (Pf)	highest magnitude in the frequency distribution derived with Fourier transform [kHz]
	Centroid frequency (Cf)	$\sum_{n=0}^{N-1} \frac{f(n)x(n)}{x(n)}$; weighted arithmetic mean [kHz] of the frequencies where $f(n)$ indicate frequencies and $x(n)$ spectrum amplitudes
	Average peak frequency (AvgPf)	$\sqrt{Pf \cdot Cf}$ measured in [kHz]
	Partial Power (PPw)	power carried by different bands of the frequency spectrum derived using Fourier transform

Table 5.1: Frequently used acoustic emissions descriptors

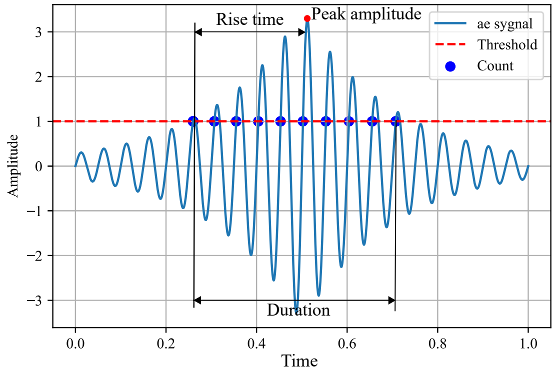

5

Figure 5.1: Schematic of acoustic emission waveform and some time-domain descriptors

5.3 Wavelet transform

The word 'wavelet' was coined to indicate *'small'* waves, meaning wave functions that are non-zero only in a limited portion of the domain. From a mathematical perspective, a mother wavelet is a function $\phi(t)$ respecting the following conditions:

$$\int_{-\infty}^{+\infty} \phi(t)^2 dt = 1 \tag{5.1}$$

$$\int_{-\infty}^{+\infty} |\phi(t)| dt < +\infty \tag{5.2}$$

$$\int_{-\infty}^{+\infty} \phi(t) dt = 0 \tag{5.3}$$

To explain why did this particular class of functions became interesting for signal processing, the analysis of a signal containing two distinct predominant frequencies of 2 Hz and 5 Hz, active in different portions of the time domain, is shown in figure 5.2.

If a standard Fourier transform was applied to the example signal, a spectrum of the predominant frequencies would be obtained. The result would show, in this case, two frequency peaks respectively at 5 Hz and 2 Hz. But what if we were not only interested in the frequency peaks? What if we also want to know when these frequencies were active? In the example case, we want a transformation capable of showing that the higher-frequency block is active in the signal before the lower-frequency block.

For this purpose, a wavelet transform can be used. Among the many possible functions respecting equations 5.1,5.2 and 5.3, the Morlet wavelet is selected for this example. Morlet wavelets are sinusoidal functions bounded by a Gaussian envelope (figure 5.2). The wavelet transform (WT) of a signal $x(t)$ is defined as:

$$X_{a,\tau} = \frac{1}{\sqrt{a}} \int_{t=-\infty}^{t=+\infty} x(t)\phi^*(\frac{t-\tau}{a})dt \tag{5.4}$$

where $\phi(t)$ is the mother wavelet function (previously introduced), a is the dilation variable (or scale factor), τ is the time translation variable, and $*$ represents the conjugate operation (in the case of complex functions). As the values of a and τ are changed, the mother wavelet is convoluted over frequency and time. Compared to the Fourier transform then, wavelets are convoluted also over time. The result of the transformation is a signal that has higher values in the portions of the period where the original signal frequency matches a specific kernel frequency. When this procedure is repeated for multiple frequencies, the result is a time-frequency coefficient matrix.

In the example case, the coefficient of high frequency (5 Hz) and lower frequency (2 Hz), are high in the time where they were more active in the original signal (figure 5.2). In this example, we just showed a time-frequency analysis, which is particularly useful in the case of non-stationary signals. In fact, the example signal analyzed in figure 5.2 was chosen to resemble the burst-decay signals normally recorded in acoustic emission monitoring. For the sake of the explanation, the convolution of a real-valued Morlet wavelet was shown. The reader should consider however that in many cases, and similar to what is done in Fourier transform, to avoid phase dependency and extract power and phase, complex-valued wavelet functions are used. In this case, the basic concept does not change, and the transformation is performed like in the complex Fourier transform. Wavelet

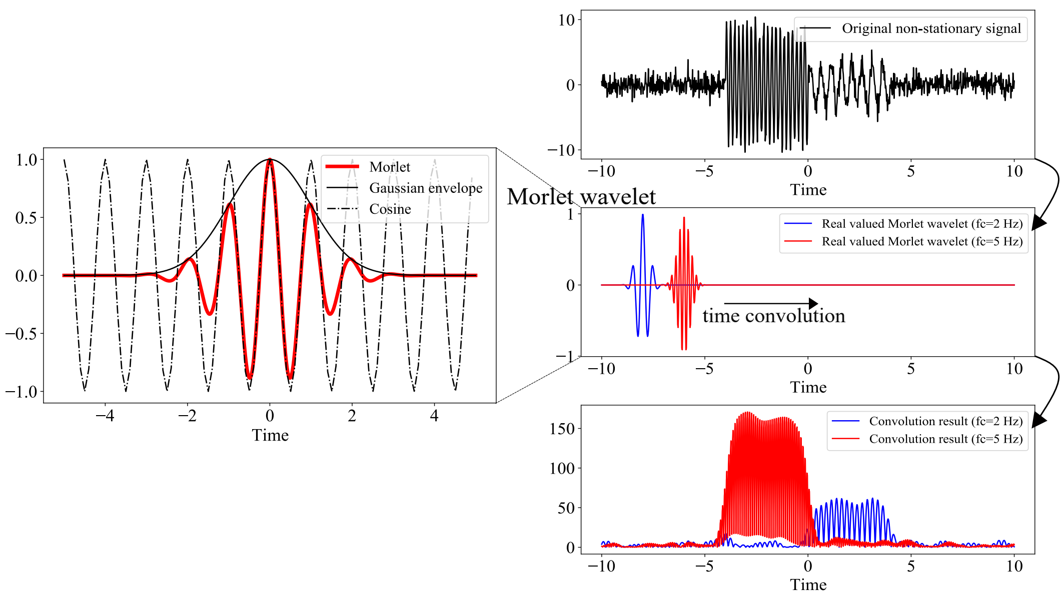

Figure 5.2: Morlet wavelets convolution visually explained

transforms are not the only tool available to perform time-frequency resolution. Short-time Fourier transforms (STFT) operate a Fourier transform in partitions of the domain. Partitioning the domain into smaller parts, however, comes with the price of losing high-frequency information. Compared to the STFT, a wavelet transform provides an adapted time-frequency resolution. This is because the dilation of the mother wavelet, achieved by varying the scale parameter a, determines that short-time windows are analyzed for high frequencies while longer-time windows are analyzed for low frequencies.

Based on the number of scales analyzed, wavelet transformations can be divided into continuous and discrete. If the number of scales is high, X_a is called a continuous wavelet transformation. This class of wavelets provides an extremely clear picture both in frequency and time domain but is computationally expensive and hence difficult to apply to large data.

To reduce the computational cost, a discrete wavelet transformation can be used instead, by analyzing a reduced number of scales and avoiding redundant information. Wavelet packet transforms (WPT) are discrete wavelet transforms that allow to decompose the signal into components covering equal frequency sub-bands. This is achieved by decomposing the original signal into a low-frequency component (approximation) and a high-frequency component (detail). This operation is repeated multiple times until reaching the desired decomposition level. Given a decomposition tree like the one shown in figure 5.3, the frequency range covered by each component can be determined by knowing the decomposition level j, the component number n, and the sampling frequency f_s of the original signal.

$$f_{range} = \left[\frac{nf_s}{2^{j+1}}, \frac{(n+1)f_s}{2^{j+1}}\right], n = 0, 1, ..., 2^j - 1 \tag{5.5}$$

The energy of the wavelet packet component at level j is the energy of the transformed signal. In the case of a discrete signal, it can be calculated with the summation over the time domain T of the signal squared.

$$E_n^j = \sum_{t=0}^{t=T} \left[X_n^j(t)\right]^2 \tag{5.6}$$

The introduced concepts are essential to the signal analysis of acoustic emission and will be used in the following sections. However, some theoretical aspects of wavelets are not explained for conciseness. For the mathematical and theoretical background of wavelets and more details about their various applications, the reader is referred to Refs. [3–5].

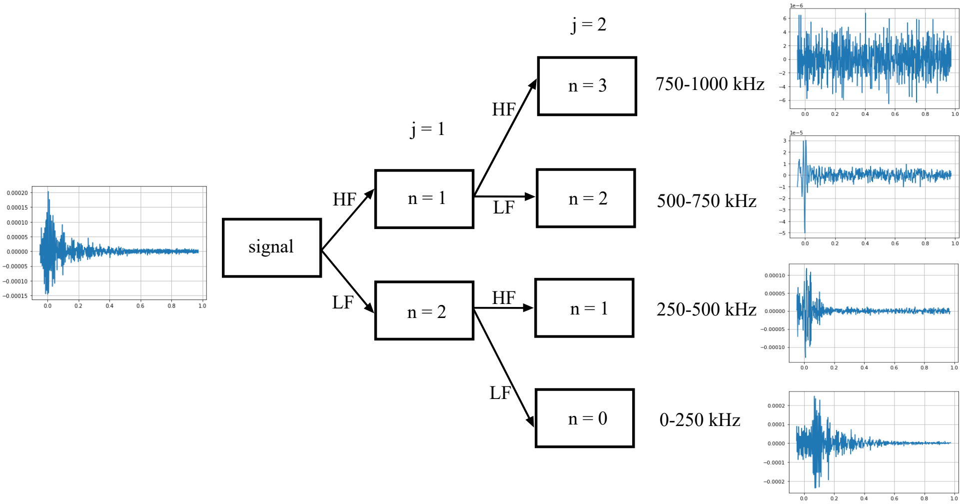

Figure 5.3: Wavelet packet level 2 decomposition tree of an acoustic emission waveform. An acoustic signal (left side) goes through successive filtering which decomposes the signal in high-frequency (HF) detail components and low-frequency (LF) approximation components.

5.4 Damage mode identification using AE

Damage mode identification using AE is based on the assumption that different source mechanisms produce different elastic waves which result in different acoustic signals. With signal analysis, it is possible to evaluate the similarity between different waveforms. Combining signal analysis with inspection techniques and knowledge about fracture in CFRP, groups of signals can then be associated with specific damage modes.

Behind this simple concept lay several complications, and damage mode separation using AE is still an open research problem. This is because the recorded acoustic signals are not only influenced by the source mechanisms but also by wave propagation effects. Due to attenuation, the signal parameters vary if the source-to-sensor distance and characteristics of the media of propagation are changed. Because of that, there is a high dependency of the recorded signals on the type of test performed, position of the sensors, layup, and thickness of the composite material. It is difficult to compare waveforms generated by the same damage modes but recorded in different tests. Concerning this aspect, modeling of acoustic wave propagation in CFRP [6] suggests that frequency parameters are less sensitive to the source to sensor propagation and for this reason, they are preferable for damage mode identification.

To establish a ground truth in acoustic emission interpretation, previous researchers performed simplified tests to find an empirical relation between damage modes and recorded acoustic waveforms. The work by De Groot et al. [7] is an example of this experimental procedure. In this series of tests, unidirectional CFRP was loaded in different conditions to determine the frequency content of different damage modes. Tensile tests of 90° blocks were used to isolate matrix cracks, DCB, and shear tests were performed for matrix-fiber debonding while 0° and 10° tensile tests were useful to isolate fiber pullout and fiber fracture. Matrix cracking was found to occupy lower frequencies, while fiber failure was assigned to relatively high frequencies. In this early investigation, it was evident how certain damage modes, like debonding and pullout, are hard to isolate. It was also observed how the same damage modes can produce signals with different characteristics if the type of test is changed. Similar preliminary tests have been performed by various authors [8, 9]. In all results, there seems to be a clear distinction in the frequency parameters at least between damage modes affecting the matrix and damage affecting the fibers.

Despite the limitations and the questions still open, preliminary tests from the literature show that it is possible to separate at least some of the damage modes using signal analysis. Composite material failure is usually composed of thousands of damage events. Because of this additional challenge, data analysis strategies have been adopted to identify large numbers of signals in complex tests. In the review by Saeedifar and Zarouchas [2] methodologies for damage mode identification were divided into four main classes:

5

- **Manual separation** a single feature like peak frequency [7, 10]; amplitude or AE energy [11] is chosen to individuate groups of similar waveforms and associate them to damage modes. The main advantage of this approach is its simplicity. however, it's not always possible to find a single feature able to separate properly different damage mechanisms.

- **Supervised classification**; selected waveforms representative of specific damage modes are used to train a classification algorithm. The features of the algorithm are composed of a set of waveform descriptors [12–14]. The disadvantage of this method is that a ground truth has to be established through preliminary testing or modeling. Once this knowledge is available, however, the results are more reliable than in other methods.

- **Unsupervised clustering**; an optimal number of clusters is estimated with no a priori knowledge about the damage modes. The clusters are formed with different algorithms using multiple waveform descriptors as features [15–19]. The main advantage of this approach is that no prior knowledge is required about expected damage modes. The disadvantage of the method is that without ground truth, the interpretation of the results has to be validated through other inspection techniques.

- **Signal analysis using wavelets**; specific wavelet packet components are associated to different damage modes [20–22]. This approach is particularly useful in case multiple damage events reach sensors almost simultaneously. The main limitation is that, in some cases, different damage modes can release energy in the same frequency band.

Although numerous studies have performed damage mode separation in CFRP materials, little attention has been given to compression after impact tests. Experiments have been conducted to separate damage modes in glass fiber reinforced polymers (GFRP) [23]. Arumugan et al. [24] performed quasi-static CAI tests on cross-ply CFRP and provided a damage mode separation purely based on peak frequency. More recently Saeedifaar et al.

[25] compared different unsupervised clustering algorithms to separate damage modes in CAI of woven CFRP using only peak frequency as a feature. This study dealt with woven cross-ply CFRP, hence the damage modes may differ from layups of unidirectional plies of CFRP. There is a lack of literature regarding the study of damage accumulation and final failure in CAI quasi-static and fatigue tests in laminates of unidirectional plies of CFRP. The few existing studies did not target specifically the separation of damage modes.

The present chapter aims to identify the damage modes present in the CAI test using acoustic emissions. To do this, quasi-static compression tests are conducted to correlate waveforms to damage modes. Because of the known dependency of waveforms on the test fixture and loading conditions, the preliminary tests were chosen to isolate damage modes but also to be as similar as possible to the CAI setup.

5.5 Experimetal methodology

5.5.1 Preliminary tests design

The following preliminary tests were conducted to correlate acoustic waveforms to damage modes:

- block 90° test; a rectangular specimen of dimensions 135 × 100 × 3.8 mm and layup $[90]_{24}$ was tested to isolate pure matrix cracking. Compression was applied at a loading rate of 1 mm/min while reproducing the boundary conditions of ASTM D7137. Two AE sensors were placed on the opposite surface of a speckle pattern for DIC image acquisition.

- block 0° test; a rectangular specimen of dimensions 110 × 85 × 1.8 mm and layup $[0]_{12}$ was tested to isolate fiber failure and fiber-matrix debonding. Compression was applied reproducing the boundary conditions of ASTM D7137 at a loading rate of 1 mm/min. One AE sensor was located on the opposite surface of a speckle pattern for DIC image acquisition.

- PTFE inclusion test; a rectangular specimen of dimensions 120 × 90 × 2.5 mm and layup $[-45, 0, 45, 90]_2$, was tested in compression. A circular PTFE insert of diameter 50 mm was located in the center of the 0//45 interface (second interface from the surface) to trigger sub-laminate buckling and delamination. A speckle pattern for DIC acquisition was applied on the face closest to the PTFE insert, to better capture the local buckling. Two AE sensors were placed on the opposite surface of a speckle pattern for DIC image acquisition. A compression loading rate of $1mm/min$ was applied while reproducing the boundary conditions of ASTM D7137.

Material and curing processes were the same as described in chapter 2.

5.5.2 Acoustic emission apparatus

AE signals were recorded by using sensors placed on one side of the specimen. The used AE sensor was the AE1045SVS900M, a broadband single-crystal piezoelectric transducer with an operational frequency range of 100–900 kHz supplied by Vallen Systeme GmbH. In addition, an external 34 dB pre-amplifier was used to amplify the recorded signals. To reduce noise, an acquisition threshold was set to 45 dB. The AE data was collected with a sampling frequency of 2 MHz by the AMSY-6 Vallen, 4-channel AE system. Ultrasound gel was applied to improve the coupling between the AE sensor and the specimen's surface. The two sensors were kept in position using plastic sensor holders glued to the surface of the specimen (figure 5.4). The performance of the AE system was validated before each test by conducting a standard pencil lead break procedure.

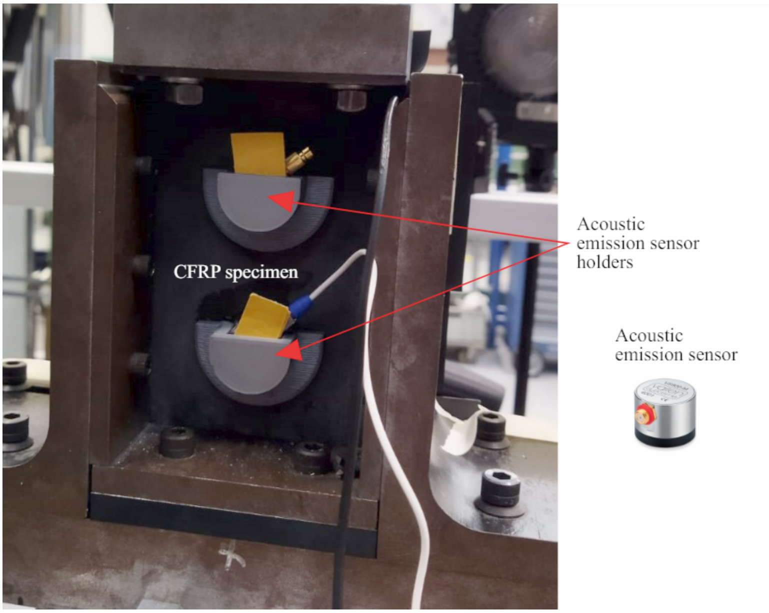

Figure 5.4: CAI fatigue setup showing the AE sensors located inside the 3d printed sensor holders, which are glued to the surface of the CFRP rectangular specimen

5.6 Results, identification of damage modes

The recorded AE waveforms were analyzed using a Morlet continuous wavelet using the open-source tool PyWavelet [26]. The transformed AE data was visualized using scalograms. In the color plots shown in figure 5.5, the absolute value of continuous Morlet wavelet coefficients is plotted in the time-frequency scale. Horizontal sub-plots are the original signals aligned in the time domain. Vertical sub-plots are the Fourier spectrum of the signals aligned in the frequency domain. Four main waveform types could be identified, as shown in table 5.2:

- Type a) The spectrum is characterized by low frequency (100–200 kHz) and long duration. It was present in tests [0], [90] and PTFE, but was dominant in the [90] test. For this reason, this waveform was associated with pure matrix cracking. A different tensile campaign also associated matrix cracking with low-frequency events [27] and numerical modeling of AE [6] confirms this assumption.

- Type b) The spectrum is characterized by an intermediate frequency (250–400 kHz) and by a shorter duration. This type of waveform was present in the [0] test and PTFE test and rarer, (but still present) in the [90] test. This waveform was associated with fiber matrix-debonding. In a previous experimental tensile campaign debonding was also associated with intermediate frequency events [27] and numerical modeling of AE [6] seems to confirm this assumption.
- Type c) The signal appears to be a combination of waveform types a and b. It was the predominant signal in the [0] test and PTFE-test, especially close to final failure, and less frequent in the [90] test. The author hypothesizes that this waveform could be the result of a combination of fiber-matrix debonding and matrix cracking. A possible explanation for this phenomenon could be that, in some cases, debonding triggers matrix cracking. This could explain the apparent superposition of waveforms a and b, if the two signals arrive at the sensor almost at the same time. It must be stressed that this is a hypothesis made by the author and further investigation is needed to test this hypothesis.
- Type d) The spectrum is characterized by several local peaks, some of them at high frequencies (450–600 kHz). This waveform was absent in the [90] test. In the [0] test and PTFE-test, it appeared only at relatively high stress. Considering this, waveform type-d was associated with fiber failure. A previous tensile campaign associated fiber failure with high-frequency events [27] and numerical modeling of AE source [6] seems to confirm this assumption.

Some works in literature [24, 28], clustered 'delamination-type' AE signals based on frequency or time domain descriptors. However, in the wavelet analysis performed in the current research, no new predominant waveform was observed in test PTFE at the onset of delamination propagation (evaluated from the DIC images) compared to the [0] test and [90] test, where no delamination occurred. For this reason, no specific waveform was associated with delamination propagation. This could be explained by considering that the microstructural damage modes composing delamination are still pure matrix cracking and fiber-matrix debonding, which were present also in the other tests performed.

Table 5.2: Detected types of waveform in preliminary tests

Waveform	**[90] test**	**[0] test**	**PTFE test**	**Freq. [kHz]**	**Damage mode**
a	Predominant	Present	Present	100-200	Matrix cracking
b	Rare	Present	Present	300-450	Debonding
c	Rare	Present	Present	100-450	Matrix cracking + Debonding
d	Absent	Present at high stress	Present at high stress	400-600	Fiber failure

5

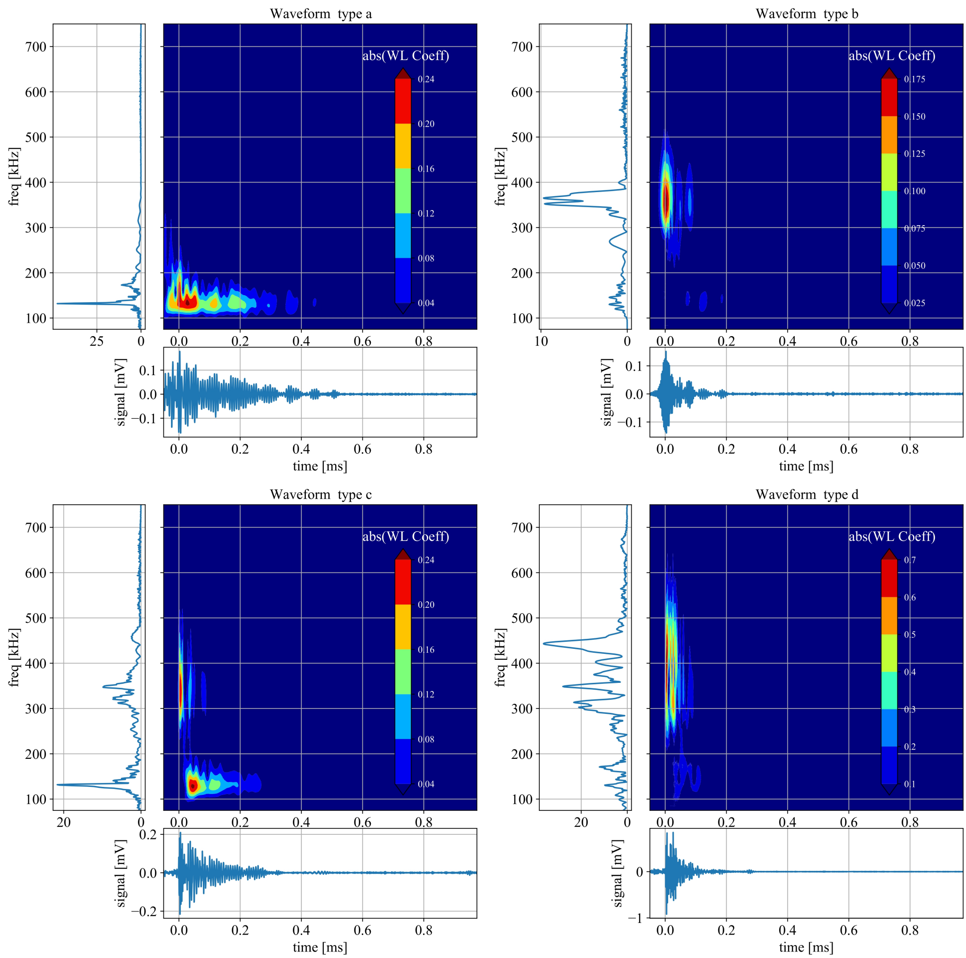

Figure 5.5: Wavelet transform of the different types of waveforms. The color plot represents the coefficient derived from the Morlet wavelet transform. The vertical subplots show the frequency spectrum derived from the Fourier transform. The horizontal subplots show the original signal

5.7 Signal descriptors problem

In section 5.2, the concept of acoustic wave descriptors has been introduced. In the last section then, typical waveforms associated to damage modes have been individuated. At this point, a critical aspect relating to the clustering and classification of these waveforms is discussed. In particular, this section shows why, in certain cases, signal descriptors are not fit to perform clustering and classification of acoustic signals.

To prove this, K-means clustering was implemented to divide the acoustic emission recorded in the preliminary tests into four clusters. The adopted clustering algorithm is rather simple and in literature far more complex algorithms have been adopted. However, the limitations that are observed, are dependent on the adoption of signal descriptors as features more than the clustering algorithm itself, hence they can be expected also in more complex algorithms.

The clustering was performed starting from different sets of features (for descriptors definition refer to Table 5.1):

1. **time domain descriptors**: maximum amplitude, rise time, duration, counts, energy
2. **frequency domain descriptors**: peak frequency, centroid frequency, weighted peak frequency, partial powers
3. **time-frequency domain descriptors**: all the above

Waveforms from the preliminary tests were analyzed to derive the different descriptors. The descriptors were then normalized and used as features in the k-means algorithm. This approach was followed using only time-domain descriptors (case 1), only frequency-domain descriptors (case 2), and both time and frequency-domain descriptors (case 3). Once the clusters were created and the acoustic events were assigned to the clusters, the Euclidean distance of each event from the respective clustering centroid was calculated. This is because ideally, the more an acoustic event is located close to its cluster centroid, the more it can be considered to be representative of that specific cluster. Events more representative of each cluster were then selected. These events were picked from an area close to the centroid, where the 10% of closest members were situated. This was done because, if the clustering works correctly, these events should have the highest level of similarity between each other and should represent the same damage mode. To verify this and to evaluate their level of similarity, their continuum wavelet transform scalograms were then compared in figures 5.6, 5.8 and 5.8. In all the figures, color plots represent scalograms obtained by applying the Morlet continuum transform.

Figure 5.6 shows two nearby events individuated using clustering based on time domain descriptors. In this case, the time domain descriptors were similar and located the signals in the same cluster. Although similar counts, duration, and peak amplitude were present, the scalogram shows a very different frequency spectrum. In this case, a frequency analysis would place the two signals in different clusters since the first waveform (on the left) has a nonnegligible spectrum component at a higher frequency.

Figure 5.7 instead, shows two nearby events individuated using clustering based purely on frequency domain descriptors. The two waves are characterized by similar spectrum and partial powers, as can be seen in the vertical plots on the side of the scalograms, representing the Fourier spectrum. By looking at the scalogram it can be seen how in the first case a single waveform is present, while the second case is characterized by a composition of two waveforms the first having low frequency while the second having a higher frequency contribution. This shows how a frequency-based description fails in case event superposition takes place.

Figure 5.8 finally, shows two nearby events individuated using clustering based both on frequency and time domain descriptors. The results show how, in the case of more complex events superposition, even combined time and frequency descriptors can give misleading information. For example in the case shown in Figure 5.8 similar distribution of partial power, the same peak frequency, and similar duration amplitude and rise time characterized acoustic events having largely different scalograms. This caused the clustering algorithm to locate them in the proximity of the same cluster centroid.

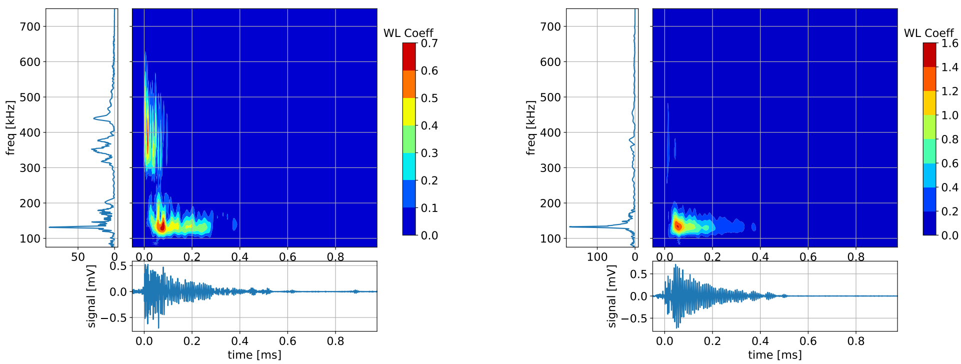

Figure 5.6: The scalogram derived with Morlet wavelets is plotted in two signals located in the proximity of the same cluster centroid with the clustering based on time-domain descriptors. Although the signals in the time domain appear similar (horizontal subplots) large differences can be found in The frequency domain (vertical subplots) and in the wavelet coefficient.

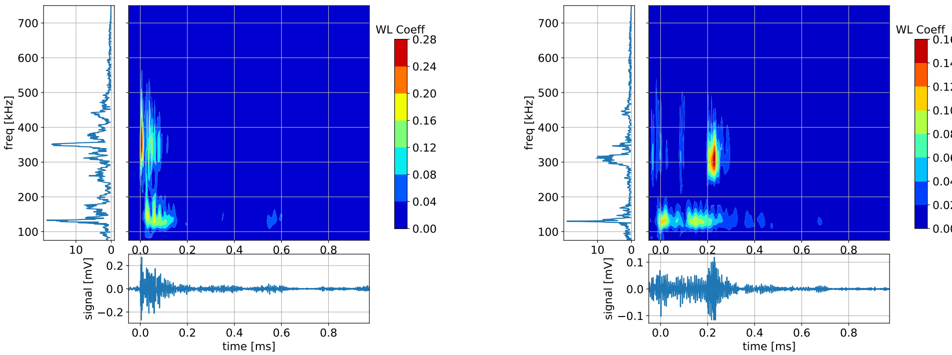

Figure 5.7: The scalogram derived with Morlet wavelets is plotted in two signals located in the proximity of the same cluster centroid with the clustering based on frequency-domain descriptors. Although the frequency spectrum is similar (vertical plots on the left), the wavelet plot reveals that in the second signal, a higher frequency event reaches the sensor after low frequency.

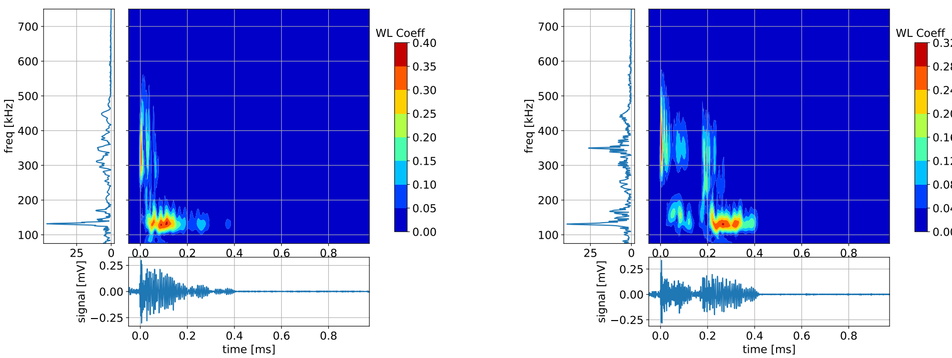

Figure 5.8: The scalogram derived with Morlet wavelets is plotted in two signals located in the proximity of the same cluster centroid with the clustering based on time-frequency domain descriptors. The frequency spectrum is similar (vertical subplots), and descriptors in the time domain (horizontal subplots) like rise time, peak amplitude, and duration are similar. However, wavelet plots show largely different scalograms.

5.8 Conclusions

In conclusion, an experimental methodology was implemented to isolate acoustic waveforms corresponding to the damage modes present in CAI tests. Through AE monitoring of quasi-static compression test of different layups ($[0]_{12}$, $[90]_{24}$ and $[-45, 0, 45, 90]_2$ with PTFE insert), four distinct waveform types were individuated and associated with matrix cracking, fiber-matrix debonding, their combination, and fiber failure.

Interestingly, despite delamination propagation was introduced artificially using a PTFE insert, no new waveform type emerged, indicating that at the microscale, the observed damage modes remain consistent with matrix cracking and fiber-matrix debonding. This suggests that AE cannot differentiate between delamination and matrix cracking or fiber-matrix debonding during a CAI test, at least using the analysis methods employed in the current research.

The application of k-means clustering showed that traditional descriptors, relying on time and frequency domain data, don't always separate the waveforms isolated in the preliminary tests. In particular, in the case of acoustic signals superposition, similar descriptors are assigned to signals that have obviously different time-frequency scalograms. Conversely, continuum wavelet scalograms provided better quality information and, in the case of superposition of signals, different events could be distinguished visually. This suggests that wavelet transforms potentially offer upgraded information for AE waveform clustering and classification purposes.

References

[1] Davide Biagini, John-Alan Pascoe, and René Alderliesten. Investigation of compression after impact failure in carbon fiber reinforced polymers using acoustic emission. *Journal of Composite Materials*, 57(10):1819–1832, 2023.

[2] Milad Saeedifar and Dimitrios Zarouchas. Damage characterization of laminated composites using acoustic emission: A review. *Composites Part B: Engineering*, 195:108039, 2020.

[3] Ingrid Daubechies. The wavelet transform, time-frequency localization and signal analysis. *IEEE transactions on information theory*, 36(5):961–1005, 1990.

[4] Matthias Holschneider, Richard Kronland-Martinet, Jean Morlet, and Ph Tchamitchian. A real-time algorithm for signal analysis with the help of the wavelet transform. In *Wavelets: Time-Frequency Methods and Phase Space Proceedings of the International Conference, Marseille, France, December 14–18, 1987*, pages 286–297. Springer, 1990.

[5] C Saritha, V Sukanya, and Y Narasimha Murthy. Ecg signal analysis using wavelet transforms. *Bulg. J. Phys*, 35(1):68–77, 2008.

[6] Markus GR Sause and S Horn. Simulation of acoustic emission in planar carbon fiber reinforced plastic specimens. *Journal of Nondestructive Evaluation*, 29:123–142, 2010.

[7] Peter J De Groot, Peter AM Wijnen, and Roger BF Janssen. Real-time frequency determination of acoustic emission for different fracture mechanisms in carbon/epoxy composites. *Composites science and technology*, 55(4):405–412, 1995.

[8] R Gutkin, CJ Green, S Vangrattanachai, ST Pinho, P Robinson, and PT Curtis. On acoustic emission for failure investigation in cfrp: Pattern recognition and peak frequency analyses. *Mechanical systems and signal processing*, 25(4):1393–1407, 2011.

[9] Reza Mohammadi, Mehdi Ahmadi Najafabadi, Milad Saeedifar, Jalal Yousefi, and Giangiacomo Minak. Correlation of acoustic emission with finite element predicted damages in open-hole tensile laminated composites. *Composites Part B: Engineering*, 108:427–435, 2017.

[10] Mohamad Fotouhi, Putu Suwarta, Meisam Jalalvand, Gergely Czel, and Michael R Wisnom. Detection of fibre fracture and ply fragmentation in thin-ply ud carbon/glass hybrid laminates using acoustic emission. *Composites Part A: Applied Science and Manufacturing*, 86:66–76, 2016.

[11] Masood Nikbakht, Jalal Yousefi, Hossein Hosseini-Toudeshky, and Giangiacomo Minak. Delamination evaluation of composite laminates with different interface fiber orientations using acoustic emission features and micro visualization. *Composites Part B: Engineering*, 113:185–196, 2017.

[12] John P. McCrory, Safaa Kh. Al-Jumaili, Davide Crivelli, Matthew R. Pearson, Mark J. Eaton, Carol A. Featherston, Mario Guagliano, Karen M. Holford, and Rhys Pullin. Damage classification in carbon fibre composites using acoustic emission: A comparison of three techniques. *Composites Part B: Engineering*, 68:424–430, 2015.

[13] TH Loutas and V Kostopoulos. Health monitoring of carbon/carbon, woven reinforced composites. damage assessment by using advanced signal processing techniques. part i: Acoustic emission monitoring and damage mechanisms evolution. *Composites science and technology*, 69(2):265–272, 2009.

[14] Milad Saeedifar, Mohamed Nasr Saleh, Sofia Teixeira De Freitas, and Dimitrios Zarouchas. Damage characterization of adhesively-bonded bi-material joints using acoustic emission. *Composites Part B: Engineering*, 176:107356, 2019.

[15] Walid Roundi, Abderrahim El Mahi, Abdellah El Gharad, and Jean-Luc Rebiere. Acoustic emission monitoring of damage progression in glass/epoxy composites during static and fatigue tensile tests. *Applied Acoustics*, 132:124–134, 2018.

[16] Mariem Ben Ameur, Abderrahim El Mahi, Jean-Luc Rebiere, Isabelle Gimenez, Moez Beyaoui, Moez Abdennadher, and Mohamed Haddar. Investigation and identification of damage mechanisms of unidirectional carbon/flax hybrid composites using acoustic emission. *Engineering Fracture Mechanics*, 216:106511, 2019.

[17] El Hadi Saidane, Daniel Scida, Marie-José Pac, and Rezak Ayad. Mode-i interlaminar fracture toughness of flax, glass and hybrid flax-glass fibre woven composites: Failure mechanism evaluation using acoustic emission analysis. *Polymer Testing*, 75:246–253, 2019.

[18] Isa Emami Tabrizi, Adnan Kefal, Jamal Seyyed Monfared Zanjani, Cagdas Akalin, and Mehmet Yildiz. Experimental and numerical investigation on fracture behavior of glass/carbon fiber hybrid composites using acoustic emission method and refined zigzag theory. *Composite structures*, 223:110971, 2019.

[19] Mondher Haggui, Abderrahim El Mahi, Zouhaier Jendli, Ali Akrout, and Mohamed Haddar. Static and fatigue characterization of flax fiber reinforced thermoplastic composites by acoustic emission. *Applied acoustics*, 147:100–110, 2019.

[20] Mohamad Fotouhi, Parinaz Belalpour Dastjerdi, and Mehdi Ahmadi. Acoustic emission based method to characterize glass/epoxy composite damages during 3-point bending test. *Int J Mater Sci*, 4(1):22–30, 2014.

[21] Mohamad Fotouhi, Milad Saeedifar, Seyedali Sadeghi, Mehdi Ahmadi Najafabadi, and Giangiacomo Minak. Investigation of the damage mechanisms for mode i delamination growth in foam core sandwich composites using acoustic emission. *Structural Health Monitoring*, 14(3):265–280, 2015.

[22] Ramin Khamedi, Saeed Abdi, Amir Ghorbani, Amir Ghiami, and Seckin Erden. Damage characterization of carbon/epoxy composites using acoustic emission signals wavelet analysis. *Composite Interfaces*, 2019.

[23] J Jefferson Andrew, V Arumugam, K Saravanakumar, Hom Nath Dhakal, and C Santulli. Compression after impact strength of repaired gfrp composite laminates under repeated impact loading. *Composite structures*, 133:911–920, 2015.

[24] V Arumugam, A Adhithya Plato Sidharth, and C Santulli. Characterization of failure modes in compression-after impact of glass–epoxy composite laminates using acoustic emission monitoring. *Journal of the Brazilian Society of Mechanical Sciences and Engineering*, 37:1445–1455, 2015.

[25] Milad Saeedifar, Mohamed Nasr Saleh, Hassan M El-Dessouky, Sofia Teixeira De Freitas, and Dimitrios Zarouchas. Damage assessment of ncf, 2d and 3d woven composites under compression after multiple-impact using acoustic emission. *Composites Part A: Applied Science and Manufacturing*, 132:105833, 2020.

[26] Gregory Lee, Ralf Gommers, Filip Waselewski, Kai Wohlfahrt, and Aaron O'Leary. Pywavelets: A python package for wavelet analysis. *Journal of Open Source Software*, 4(36):1237, 2019.

[27] Abida Satour, Silvio Montrésor, Mourad Bentahar, and F Boubenider. Wavelet based clustering of acoustic emission hits to characterize damage mechanisms in composites. *Journal of Nondestructive Evaluation*, 39:1–11, 2020.

[28] Milad Saeedifar, Mehdi Ahmadi Najafabadi, Dimitrios Zarouchas, Hossein Hosseini Toudeshky, and Meisam Jalalvand. Clustering of interlaminar and intralaminar damages in laminated composites under indentation loading using acoustic emission. *Composites Part B: Engineering*, 144:206–219, 2018.

6

Acoustic Emission analysis of static CAI

Acoustic emission analysis was used to gain insight into the damage mechanisms occurring during quasi-static CAI tests.

In quasi-static tests, it was possible to identify different phases of the damage accumulation at different load levels. This suggests that, even with cyclic loading, different types of fatigue damage propagation can be expected depending on the maximum amplitude and activated damage modes.

In the quasi-static CAI tests, the onset of unstable damage accumulation was triggered by an intermediate frequency acoustic event, associated with a combination of debonding and matrix cracking, occurring at 80% of failure displacement. This phenomenon was linked to the concept of threshold for delamination growth under fatigue introduced in Chapter 2.

Results of the following chapter have been previously published in a journal article [1].

6.1 AE in static CAI

In the previous chapter, acoustic emission monitoring and damage mode identification were introduced. In the current chapter, acoustic emission monitoring and analysis are applied to quasi-static Compression After Impact (CAI) tests. Even though the main aim of this thesis is to enhance the comprehension of fatigue after impact, it was decided to dedicate one chapter to the study of quasi-static CAI tests because our understanding of quasi-static failure in compression after impact is also incomplete.

Previous research targeted the experimental investigation of the CAI failure in the presence of BVID [2–5]. Thanks to these valuable contributions, it was possible to identify two predominant failure modes present in CAI, namely: unstable delamination propagation triggered by local buckling of sub laminates [3, 4] and fiber kinking in areas of stress concentration [2]. Despite this extensive research, due to the difficulty in observing the damage state which progresses rapidly and internal to the structure, two major knowledge gaps are still present.

The first knowledge gap concerns the damage accumulation process. As the applied compression stress is increased in CAI quasi static tests, local stress concentrates in the geometrical singularities of impact damage, potentially leading to the propagation of the preexisting impact damage. Arumugam et al. [6] observed AE activity associated with the formation of damage from a relatively low stress in CAI tests. Bull et al. [7] stopped a CAI test at near failure stress and, by performing computed tomography scans, observed that consistent delamination propagation already took place. These observations all indicate that damage propagation starts before the 'CAI ultimate strength'. It is still unclear, however, which damage modes are active during this first phase, what is the interaction between them and what is their effect on the strength degradation.

The second knowledge gap concerns final failure. Once the critical load is reached, damage propagates extremely fast. There was experimental evidence of unstable delamination propagation concurrent to buckling [3], and fiber kinking in the areas of compressive stress concentrations at the original contours of impact delamination [8]. Although there is a knowledge of the general failure mechanisms, there is no consensus about the trigger mechanisms to the final failure. It is also unclear how the interaction between the damage modes is regulated by the pre-existing impact damage geometry shape [9] or by the properties of the resin [10].

This chapter aims to apply advanced acoustic signal processing techniques to gain a better understanding of the processes of damage accumulation and final failure in CAI quasi-static tests. In particular, the goal is to identify the relative contribution of different damage modes during different stages of the process. Although the investigation presented here concerns static failures, the results, as will be seen, are interesting for the investigation of the fatigue after impact process.

6.2 Methodology

6.2.1 Experiments

Toray M30SC – Deltapreg DT120-200-36 UD was manually laid up in a $[-45, 0, 45, 90]_{4,s}$ laminate for the static CAI tests. Curing was conducted in an autoclave following the procedure suggested by the manufacturer and explained in chapter 2. The curing temperature was 120 °C while the maximum pressure was 6 bar. Three CAI specimens of dimensions 150x100x5.15 mm were manufactured as indicated by the ASTM D7136 standard.

Impact testing was conducted using a drop-weight tower according to ASTM D7136 [11]. The support fixture has a cut-out of 125 ± 1 mm in length and 75 ± 1 mm in width. The impact tower was equipped with a catcher triggered by optical sensors to obtain single impacts (chapter 2). A hemispherical impactor with a diameter of 16 mm and a mass of 4.8 kg was used. A target impact energy of 34 J (6.7 J per mm thickness of the laminate) was used in all the impacts. This condition can be classified as low-velocity impact (LVI) and produced a dent depth < 2 mm (BVID). After the impact, the size of the delamination was checked with ultrasound inspection.

CAI testing was conducted according to ASTM D7137 [12]. In contrast with the standard fixture, the lateral anti-buckling guides had a flat contact instead of a knife edge. The test setup is shown in Figure 2.3 of Chapter 2. Specimens were loaded in compression, in a displacement-controlled mode, with a crosshead displacement of 1 mm/min. The crosshead displacement and the applied force were recorded using a 250 kN load-cell MTS hydraulic testing machine. Digital Image Correlation (DIC) was used on the impacted side of the specimen while the AE sensors were placed on the backside.

6

6.2.2 Acoustic Emissions

During CAI tests, the AE events of specimens were captured using two AE sensors positioned on the back side of the specimen. The AE sensor utilized was the AE1045SVS900 M from Vallen Systeme GmbH, known for its broadband single-crystal piezoelectric transducer capabilities, operating within the frequency range of 100–900 kHz. Additionally, an external 34 dB pre-amplifier was employed to boost the recorded signals. To mitigate noise effect, a 45 dB acquisition threshold was set. Although this level may exclude some microscale damage event, it was observed that, below 45dB amplitude, events were recorded also in the unloaded specimen. This threshold value was then considered to be a good compromise for filtering. The AE data was gathered at a sampling frequency of 2 MHz by the AMSY-6 Vallen, a 4-channel AE system. Ultrasound gel was utilized to enhance the coupling between the AE sensor and the specimen's surface. Plastic sensor holders glued to the non-impacted surface of the specimen maintained the position of the two sensors. Prior to each test, the performance of the AE system was verified through a standard pencil lead break procedure.

Acoustic signals recorded during the test are always affected by noise. In addition to that, some sources are not related to the formation of damage, like the friction between crack surfaces or signals generated by the test contact with the fixture. Signals coming from damage are assumed to be burst-type signals rising and decaying in a very short time, while friction is assumed to be a more 'continuous' type of signal. As a consequence, if wavelet transform is applied, signals caused by damage are expected to have high coefficients concentrated in specific times and frequencies. On the other side, friction signals are expected to have lower coefficients occupying a larger time window. Finally, noise is expected to have low wavelet coefficients randomly distributed in the time-frequency domain.

Considering the above, a filtering strategy composed of three stages was adopted. First, a maximum amplitude threshold for the acquisition was set to 45 dB. The analysis of the waveforms recorded with this setting revealed a low frequency (60 kHz) continuous-type signal which I associated with friction. Considering this, a high pass filter allowing only frequencies > 70 kHz was applied. Then, a four-level wavelet packet transform was applied using Daubechies 32 wavelets. To isolate damage from the background friction and noise, a hard threshold is imposed by setting to zero the WL coefficients lower than 10% of the maximum coefficient.

6.3 Damage accumulation study

The study of the damage accumulation process, is focused on three questions inspired by the work of Saeedifar et al. [13]:

1. How is the acoustic energy released when mechanical work is applied? Answering this question provides the relationship between the formation of internal damage, responsible for the acoustic activity, and the degradation of the global stiffness and integrity of the material.

2. What is the relationship between high-energy acoustic events and low-energy acoustic events? Assuming that large-scale damage generates higher energy acoustic events, analyzing question 2 can show how predominant is the microscale and macroscale damage throughout the test.

3. In which proportion are damage modes active during the test? By separating the different damage modes present in CAI test, it is possible to evaluate, thresholds for their activation in case they are present.

These three aspects combined provide an accurate description of the damage accumulation phase happening in the CAI test. The three questions will be individually discussed in the following subsections.

6.3.1 Sentry function

To answer question 1, the sentry function is used. The sentry function S was introduced by Minak and Zucchelli [14] as the logarithm of the ratio between the strain energy E_u and the cumulative acoustic energy E_a as a function of the applied displacement d:

$$S(d) = ln\left(\frac{E_u(d)}{E_a(d)}\right) \tag{6.1}$$

As the applied compression displacement increases linearly, different trends can be expected in the sentry function (figure 6.1). An increasing trend (s1) corresponds to a strain energy storing phase where mostly micro-damage is formed, as proved by the limited acoustic energy released. A sudden drop (s2) corresponds to a fast release of acoustic energy and possibly a drop in stiffness, this was associated in the past with the coalescence of micro-damage leading to macro damage [13]. It is important to remark that the sentry function depends both on acoustic activity and strain energy. A sudden drop in sentry function (s2) could be due to an increased acoustic activity without a stiffness drop. A constant trend (s3) is a state of equilibrium between the storage of strain energy and the acoustic emissions activity. An increase after a drop (s4) suggests that the previous event did not cancel the capability of the material to store strain energy. Finally, a decreasing trend (s5) is an indication of extensive damage propagation.

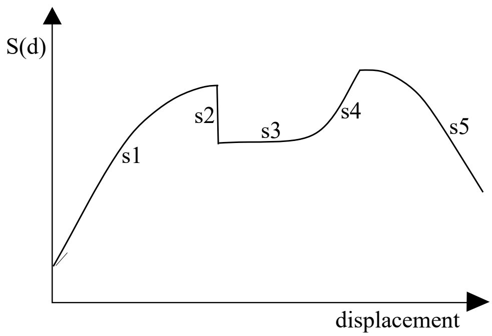

Figure 6.1: Sentry function/displacement plot. The possible trends that can be found in actual tests are shown

6.3.2 Energy b value

To answer question 2, a variation of the Gutenberg-Richter formula is adopted. The Gutenberg-Richter formula was introduced in seismology as the power law relating the intensity of a seismic event and its frequency of occurrence. On a logarithmic scale, this relationship is well approximated by a linear relationship.

$$log_{10}(N_M) = -b \cdot M + a \tag{6.2}$$

Where N_M is the number of events with magnitude $\leq M, M$ is the Richter magnitude value, while a and b are respectively the intercept and slope of the linear relationship. In the following analysis, the equation is modified for acoustic emissions, and instead of magnitude, acoustic energy is used as suggested by Sagasta et al. [15]:

$$log_{10}(N_{\overline{E}})|_d = -b \cdot log_{10}(\overline{E}) + a \tag{6.3}$$

Where $N_{\overline{E}}$ is the number of events with energy $\leq \overline{E}$. As in the case of seismic events, in a log-log scale, a linear relationship well fits the results for AE data. The value of slope b can be seen as an indication of how frequent high-energy acoustic events are compared to low-energy events. As the compression displacement is increased in the test, an increasing number of AE hits is recorded and different trends can be expected in the b value (figure 6.2). In the case of a decreasing trend (b1) acoustic emission activity has the form of accumulation of a large number of low-energy events, this can be associated with the predominance of micro-scale damage. In the case of a sudden increment (b2), there is a fast release of acoustic energy in the form of high-energy hits, this can be seen as an indication of a rapid and unstable damage event. If a constant trend (b3) is observed as acoustic activity continues, an equilibrium is present between high-energy hits and low-energy hits occurrence, suggesting that the nature of damage propagation is not changing over time. Finally, a gradually increasing trend (b4), suggests an acoustic emission activity shifting towards high-energy events. This could be an indication of a damage propagation passing from small-scale damage to larger scale damage events. It is important to remark that the b value is a 'cumulative' quantity that takes into account all the previous acoustic events and that the relationship is expressed in a log scale. A constant value of b does not mean that high and low-energy events are added at the same rate. It means that new events occur following the frequency of occurrence that characterized the test until that point.

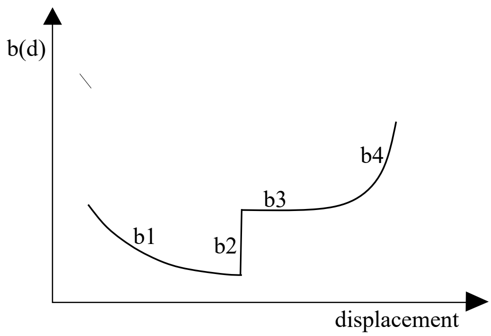

Figure 6.2: b-value/displacement plot. The possible trends that can be found in actual tests are shown

6.3.3 Wavelet packet components cumulative ratio

To answer question 3, the wavelet components cumulative ratio is proposed. In the previous chapter, a series of tests were conducted to isolate waveforms originating from different damage modes. The predominance of low frequency was associated with matrix cracks, the intermediate frequency was associated to debonding while the higher frequency was associated with fiber failure. Considering this, the wavelet packet components cumulative ratio is adopted in the present study as indicator of the relative contribution of different damage modes. Like in the case of the Sentry function and b-value, this ratio is written as a function of the displacement d applied during the test.

Wavelet packets were introduced in Chapter 5, section 5.3. Consider now the definition of wavelet packet component n at level j presented in eq.5.5 and figure 5.3 of Chapter 5. In short, level j indicated the level of decomposition (in how many frequency sub-components is the original signal divided), while n indicated the component i.e. the frequency sub-band under exam.

As the test progresses and the applied displacement d increases, an increasing amount of acoustic events is recorded. For a defined level of displacement d (i.e. moment of the test), we now define $SE_n(\overline{d})$ as the cumulative sum of component n of all the waveforms recorded at displacement values $\leq \overline{d}$ (i.e. prior to this point of the test):

$$SE_n(\overline{d}) = \sum_{d=0}^{\overline{d}} E_n^d \tag{6.4}$$

The cumulative ratio of wavelet component 'n' then is the previously defined sum $SE_n(\overline{d})$ normalized by the sum of all the i components of level j of the same waveforms recorded until this moment of the test (for $d \leq \overline{d}$).

$$R_n(\overline{d}) = \frac{SE_n(\overline{d})}{\sum_{i=0}^{j-1} SE_i(\overline{d})} \tag{6.5}$$

The defined cumulative ratio $R_n(\overline{d})$, expresses how predominant is a certain wavelet component, i.e. frequency band, compared to the others, as a function of the applied displacement (as the test progresses). The wavelet packet decomposition is performed using the Python tool PyWavelet [16]. The selected wavelet is Daubechies 32 at the decomposition level 4. Following the results of the preliminary tests in Chapter 5, components 2-3 (62.5-187.5 kHz) are associated with matrix cracking, components 4-5-6 (187.5-375 kHz) are associated with fiber-matrix debonding, and components 7-8-9 (375 - 625 kHz) are associated with fiber failure. The limitation of this methodology is the partial overlap in frequencies between some of the damage modes. For example, although fiber failure has majour contribution in the high frequency components, low frequency components are also observed in this case. Regardless of this limitation, the proposed approach can be used to show qualitative trends in the damage mode repartition since it expresses the relative influence of the different frequency sub-bands as the test progresses.

6

6.4 LVI RESULTS

Impact tests resulted in BVID (impact dent <2 mm) comprising multiple delaminations at different interfaces. In Figure 6.3 the C-scan after impact of the three specimens is shown. As can be seen in figure 6.3, a large variation in delamination size is present, especially between specimen two and the remaining specimens.

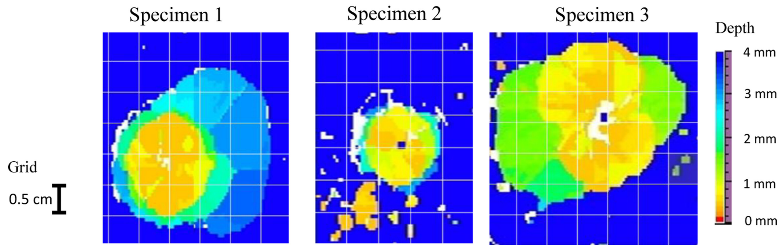

Figure 6.3: Close-up C-scan images of the impacted specimens, showing multiple delaminations at different depths. The images are cropped to show the full delamination; the impact contact point was always in the center of the specimen

6.5 CAI results

There is good agreement in load-displacement curves between the three CAI tests (Figure 6.4 (a1–a3)). The specimens showed a constant stiffness until final failure. Only in specimen two, a small drop in force is observed before failure. In all tests, the lateral guides successfully prevented the global buckling, and local buckling happening in correspondence of impact damage was observed. In all three specimens, final failure occurred from the impact location towards the lateral edges, which is acceptable according to the ASTM D713723 standard [12].

Figure 6.4 collects the results of the damage accumulation study in the three CAI quasi-static tests. In the first row of plots, the force-displacement and the cumulative acoustic energy is plotted. The second row shows the b value and sentry function while the third row shows the wavelet packet components' cumulative ratio (defined in the previous section).

As can be seen in Figure 6.4 (a1–a3), acoustic events happened from the beginning of the test. In fact the red curves, representing the cumulative energy, show non-zero values from the beginning of all tests. This early release of acoustic energy can be explained by the presence of partially damaged substructures that fail at a relatively low compression load in the CAI test. Following the red curves of acoustic emission cumulative energy, in all three specimens, there is a phase of accumulation of damage, where the cumulative AE energy appears to be linear in the logarithmic scale. After that, all tests show a sudden increase in cumulative AE energy, starting after 80% of CAI failure displacement, suggesting that an unstable mechanism could be triggering a new phase of damage propagation (Figure 6.4 (a1–a3)). It is noteworthy that this event was not accompanied by a noticeable drop in stiffness in any of the specimens. Combining all the plots in Figure 6.4 three phases can be individuated in damage accumulation, namely damage stabilization, stable damage accumulation, and unstable damage accumulation.

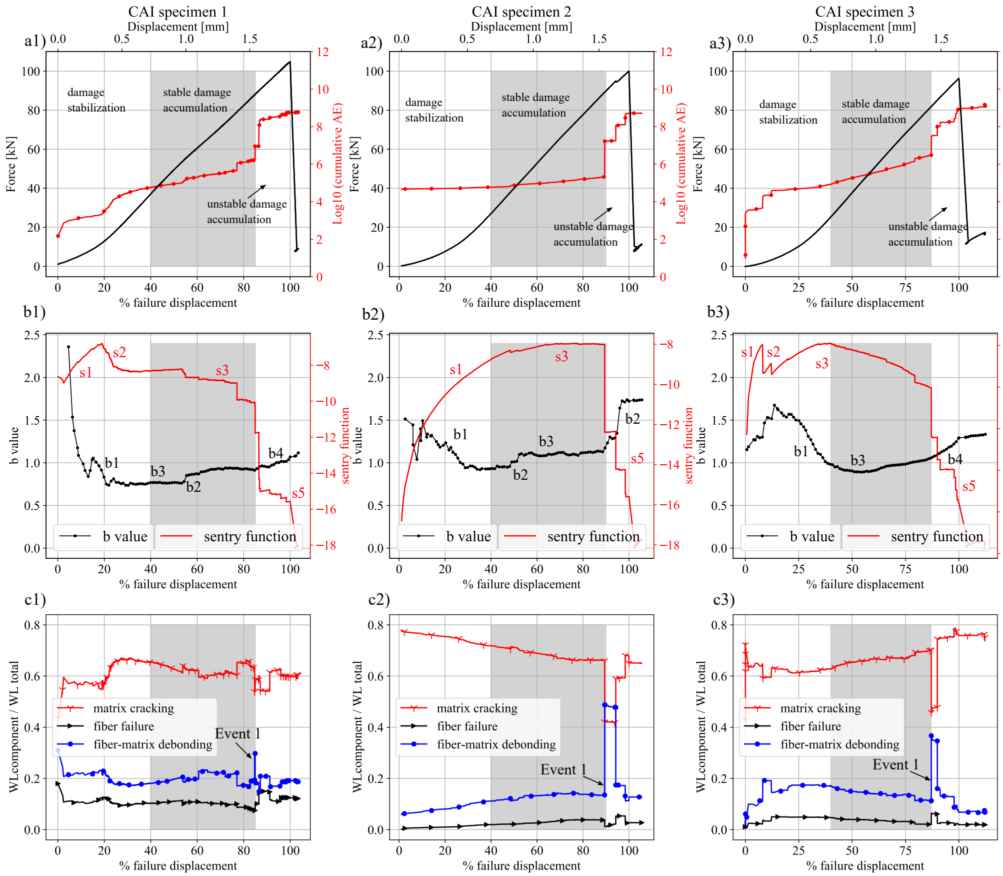

Figure 6.4: damage accumulation study in the three CAI quasi-static tests, each column of plots representing one specimen. In the first row of plots, the force-displacement and the acoustic emission cumulative signal energy (Table 5.2) are plotted. The three phases of damage accumulation are also labeled in the first row of plots. In the second row, the b value and sentry function are shown, pointing out the different trends in the b value (as described in Section 6.3.2 and Figure 6.2) and in the Sentry function (as described in Section 6.3.1 and Figure 6.1). In the third row the wavelet components ratio representing the different damage modes are plotted, and 'event 1' determining the inset of the final propagation phase, is labelled.

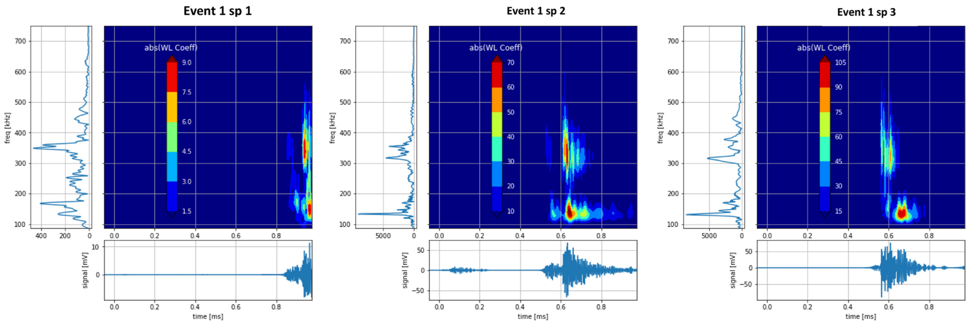

Figure 6.5: Acoustic event preceding the onset of unstable damage propagation in the three tests. The continuum Morlet wavelet scalogram is reported in the three events.

6.5.1 Damage stabilization

In all the specimens, a first phase of increase of sentry function is observed (Figure 6.4 (b1–b3)). This can be attributed to a phase of strain energy storing and relatively low acoustic activity. Although damage is accumulated, as proven by the cumulative acoustic energy (Figure 6.4 (a1–a3)), it does not degrade the capability to store strain energy, since no change in the global stiffness is observed. During this phase, a decrease in the b-value is observed (Figure 6.4 (b1–b3)). This suggests that mostly micro-damage is propagating during this phase since AE energy is released in the form of many low-energy events. During this phase, damage mode fractions are chaotic and there is no good agreement between the different specimens (Figure 6.4 (c1–c3)). To explain this, it must be considered that wavelet ratios are cumulative quantities. A single fiber fracture happening at the beginning of the test has more effect on the wavelet cumulative ratios compared to the same event happening at the end of the test. At the beginning of the test, all damage modes can potentially happen in weak areas of impact damage. Due to the stochastic nature of initial impact damage, no good agreement is found between the different tests. However, as the test goes on, the results converge towards a similar repartition between damage modes in different specimens.

6.5.2 Stable damage accumulation

After the initial increase, the sentry function flattens (spec-1,2) or starts a gradual decrease (spec-3) starting a second phase of damage propagation, which in Figure 6.4 is highlighted by the grey area. During this phase, no drops are observed in the load-displacement curve, suggesting that the material is still storing strain energy. During this phase, an exponential increase in acoustic activity is observed. This can be seen in the first row of plots showing in this phase a linear increase in the logarithm of cumulative acoustic emission energy (Figure 6.4 (a1–a3)). Besides the exponential accumulation of acoustic emission energy, small variations are observed in the b-value during this phase (Figure 6.4 (b1–b3)). This means that the relative frequency of occurrence of the high and low energy peaks does not change dramatically during the test as acoustic energy is progressively released. The damage modes repartition evaluated with cumulative ratios of wavelet packet components (last row of plots) also remains stable and assumes similar values in the different tests

(Figure 6.4 (c1–c3)). During this phase, matrix cracking is the predominant damage mode.

In conclusion, a phase of damage accumulation is observed between 50%–80% of failure displacement. Despite the exponential increase in acoustic emission energy, the nature of damage accumulation in terms of average acoustic energy of the single events (b-value) and repartition between damage modes (wavelet ratios) are stable throughout the displacement range under exam and similar between the different specimens.

6.5.3 Unstable damage accumulation

In all the specimens, the end of the stable damage accumulation is determined by a significant and sudden increase in the cumulative acoustic energy (Figure 6.4 (a1–a3)). After this event, the final phase of unstable damage propagation begins. It is interesting to observe how this initial damage event does not affect the residual stiffness since no drop is observed in the load-displacement curve. This suggests that residual compressive stiffness does not provide a good indication of the integrity of the structure in the case of quasi-static CAI loading.

The sudden release of acoustic energy results in a large drop in the sentry function. Although there is no drop in stiffness, and therefore the specimen remains capable of storing mechanical energy, the continued decrease of the sentry function indicates that a much larger portion of the applied work beyond the 80% displacement is dissipated by failure mechanisms. The step-wise increase of the AE cumulative energy (Figure 6.4 (a1–a3)) and step-wise decrease of the sentry function (Figure 6.4 (b1–b3)) shows that the final failure indeed proceeds in an unstable 'stick-slip' type manner. During this phase, an increase in the b value is observed in all the specimens, meaning that new hits come in the form of relatively high energy events (Figure 6.4 (b1–b3)). This indicates that larger-scale damage is now formed, compared to the previous phase of the tests. In all the tests the unstable phase onset is determined by a sudden increase of the wavelet component associated with debonding (intermediate frequency). The event causing this change is indicated as 'event 1' in Figures 6.4 (c1–c3) and was studied in more detail using a continuum Morlet wavelet analysis. By looking at the scalogram in Figure 6.5, it is evident that the event one in all three tests looks very similar and can be classified as waveform type c (Figure 5.5), which was attributed to a combination of debonding and matrix cracking in Chapter 5. In all tests a second event was observed, releasing a large amount of energy in the matrix cracking frequency range. After these events, the damage mode fraction evolution (as a function of displacement) largely differs in the different specimens. The numerical study of CAI failure by Yang [9] suggested that the CAI failure mode (delamination vs fiber kinking) could be highly dependent on the initial impact damage configuration. The high variability of the damage mode repartition close to CAI failure suggests that this hypothesis formulated by Yang may be correct.

6.6 Relevance for fatigue after impact

In the previous sections, it was shown how different phenomena occur at various load levels in CAI quasi-static tests. In particular, variations of b-value at different applied displacement proves that the scale of damage propagation changes as the applied load increases. Variations in wavelet packet components ratio show that a different repartition between damage modes occurs at different applied loads.

This has some important implications for the fatigue phenomena. In compression after impact fatigue, damage propagation is observed when a maximum compression load superior to 60% of CAI residual strength is applied. Within this load range, there is an obvious dependency between the applied compression load and the fatigue life. A higher load corresponds to a shorter life. However, results from this chapter suggest that varying the load, different types of damage propagation can be expected in fatigue.

At this point, it must be considered that a fatigue test is substantially the repetition of CAI quasi-static tests over time. Referring to the results presented in this chapter, if a fatigue test with a maximum amplitude of 65% of failure displacement is applied, in the first cycle the propagation of micro-scale damage mainly composed by matrix cracks is expected. If instead maximum amplitude 80% of failure displacement is applied, larger scale damage events with multiple active damage modes are expected. If this happens in the first cycle, it is reasonable to assume that similar differences persist throughout fatigue life, as long as the maximum applied load remains constant. Varying the applied load in fatigue may not only change the rate of damage propagation and the fatigue life but also result in a different scale and type of damage propagating.

6

A second important aspect concerns the threshold for delamination growth in fatigue after impact, which was discussed in Chapter 2. In the conclusions of Chapter 2, a load threshold in fatigue after impact activating the growth of delamination was hypothesized. This deduction was made after noticing the qualitative differences in axial stiffness degradation and delamination growth curves between long-life and short-life fatigue. In the case of short-life fatigue, delamination growth was immediately activated and started at the beginning of the fatigue life, while in the case of long life, the previous phase of damage accumulation eventually triggered the onset of delamination growth.

In the CAI quasi-static tests presented in this chapter, the load was increased at a slow rate, reaching eventually failure load. The residual strength after impact is superior to any fatigue load. This means that, at a certain point of the static test, a load level was reached for which delamination growth would have been activated from the first cycle in a fatigue test. It would make sense that, in quasi-static CAI tests, once the threshold load is reached, a change in damage mode distribution and an increased release of acoustic energy are recorded via acoustic emissions. Looking at the graphs in Figure 6.4, in all specimens, the onset of unstable damage accumulation was triggered by an intermediate-frequency acoustic event (Figure 6.5). The waveforms associated with this event were linked in the preliminary tests of Chapter 5 to a combination of debonding and matrix cracking. This event occurred at 80% of failure displacement. In the author's opinion, this event may represent the onset of delamination propagation. This hypothesis has to be validated via more tests and other inspection techniques. However, if validated, it would show the promising scenario of identifying the threshold for delamination fatigue growth by performing acoustic emission monitoring of quasi-static CAI tests.

6.7 Conclusions

In this chapter, the analysis of acoustic emission has shown how different phenomena occur at various load levels in CAI quasi-static tests. In particular, variations of the b-value at different applied displacements proved that the scale of damage propagation changes as the applied load increases. The variations in wavelet packet components ratio instead indicated that a different repartition between damage modes occurs at different applied loads. The combination of all the indicators of damage propagation derived from acoustic emissions revealed three phases in damage accumulation of quasi-static CAI tests, namely damage stabilization, stable damage accumulation, and unstable damage accumulation.

The observation that damage events of different scales and types are triggered at different load levels has implications for fatigue phenomena. Even with similar initial impact damage, different types of fatigue damage propagation with different activation of the damage modes can be expected depending on the applied compressive load.

In all specimens, the onset of unstable damage accumulation appears to be triggered by an intermediate frequency acoustic event, occurring at 80% of failure displacement. This event was characterized by a spectrogram compatible to a mixture of matrix crack and fiber-matrix debonding. It was hypothesized by the author that this event may indicate the onset of delamination growth.

References

[1] Davide Biagini, John-Alan Pascoe, and René Alderliesten. Investigation of compression after impact failure in carbon fiber reinforced polymers using acoustic emission. *Journal of Composite Materials*, 57(10):1819–1832, 2023.

[2] Alan Tate Nettles and Luke Scharber. The influence of gi and gii on the compression after impact strength of carbon fiber/epoxy laminates. *Journal of Composite Materials*, 52(8):991–1003, 2018.

[3] D. J. Bull, S. M. Spearing, and I. Sinclair. Observations of damage development from compression-after-impact experiments using ex situ micro-focus computed tomography. *Composites Science and Technology*, 97:106–114, 2014.

[4] XC Sun and SR Hallett. Failure mechanisms and damage evolution of laminated composites under compression after impact (cai): Experimental and numerical study. *Composites Part A: Applied Science and Manufacturing*, 104:41–59, 2018.

[5] Derek Hull and Yi Bing Shi. Damage mechanism characterization in composite damage tolerance investigations. *Composite Structures*, 23(2):99–120, 1993.

[6] V Arumugam, A Adhithya Plato Sidharth, and C Santulli. Characterization of failure modes in compression-after impact of glass–epoxy composite laminates using acoustic emission monitoring. *Journal of the Brazilian Society of Mechanical Sciences and Engineering*, 37:1445–1455, 2015.

[7] DJ Bull, SM Spearing, and I Sinclair. Observations of damage development from compression-after-impact experiments using ex situ micro-focus computed tomography. *Composites Science and Technology*, 97:106–114, 2014.

[8] Alan Tate Nettles and Luke Scharber. The influence of gi and gii on the compression after impact strength of carbon fiber/epoxy laminates. *Journal of Composite Materials*, 52:991–1003, 2018.

[9] Yu Yang. *A numerical study of damage mechanisms in the CAI of laminated composites for aerospace applications*. PhD thesis, University of Nottingham, 2016.

[10] Nobuhide Uda, Kousei Ono, and Kazuo Kunoo. Compression fatigue failure of cfrp laminates with impact damage. *Composites Science and Technology*, 69:2308–2314, 2009.

[11] Compass ASTM D7136 D7136M-15. Standard test method for measuring the damage resistance of a fiber-reinforced polymer matrix composite to a drop-weight impact event.

[12] Compass ASTM D7137 D7137M-17. Standard test method for compressive residual strength properties of damaged polymer matrix composite plates.

[13] Milad Saeedifar, Mehdi Ahmadi Najafabadi, Dimitrios Zarouchas, Hossein Hosseini Toudeshky, and Meisam Jalalvand. Barely visible impact damage assessment in laminated composites using acoustic emission. *Composites Part B: Engineering*, 152:180–192, 2018.

[14] Giangiacomo Minak and Andrea Zucchelli. Damage evaluation and residual strength prediction of cfrp laminates by means of acoustic emission techniques. *Durand, LP (ed.) Composite Materials Research Progress*, pages 165–207, 2008.

[15] Francisco Sagasta, Miguel E Zitto, Rosa Piotrkowski, Amadeo Benavent-Climent, Elisabet Suarez, and Antolino Gallego. Acoustic emission energy b-value for local damage evaluation in reinforced concrete structures subjected to seismic loadings. *Mechanical Systems and Signal Processing*, 102:262–277, 2018.

[16] Gregory Lee, Ralf Gommers, Filip Waselewski, Kai Wohlfahrt, and Aaron O'Leary. Pywavelets: A python package for wavelet analysis. *Journal of Open Source Software*, 4(36):1237, 2019.

7

Acoustic Emission analysis in CAI fatigue

A convolutional neural network algorithm has been developed to classify waveform types based on the wavelet coefficients matrix. This algorithm successfully performs the task of classifying damage modes throughout the entire fatigue after impact test.

Thanks to the study of damage mode distribution, it was possible to compare the damage evolution in short-life and long-life fatigue and make correlations with ultrasound inspections, DIC results, and stiffness degradation. The investigation reveals that to describe fatigue after impact in composite materials different damage processes activated at different load levels have to be considered.

Furthermore, it was observed that high-energy acoustic events associated with a combination of debonding and matrix cracking, correspond with the onset of delamination growth. These events belong to the same type causing the onset of unstable damage accumulation in static CAI tests.

7.1 Classification of acoustic emissions in CAI fatigue

In Chapter 2 of this thesis, it was shown how different damage evolution can be observed in long-life and short-life fatigue after impact. Short-life fatigue showed a rapid increase in delamination and degradation of stiffness starting at the beginning of fatigue life. In the case of long-life fatigue, instead, a phase of no growth of delamination and no stiffness degradation was observed, followed by a final fast growth of delamination and stiffness degradation. Two points are still unclear:

- What determines the onset of the second phase in the long-life fatigue test?
- What is happening during the initial phase of long-life fatigue, where no global stiffness degradation and no delamination growth is observed?

The inspection techniques used until this point (ultrasound scan and digital image correlation) could not answer these questions. In Chapter 6, it was shown how acoustic emission can help to understand damage propagation in static tests. It was shown how at different load levels different damage modes were activated in CAI static tests. In the study presented in the current chapter, a similar strategy is applied to investigate the damage propagation in fatigue tests comparing long-life and short-life specimens.

A method is developed to exclude noise and friction from the acoustic data analysis. After that, a convolutional neural network (CNN) algorithm is built to classify damage modes based on their wavelet coefficient matrices. The algorithm is applied to analyze the acoustic emissions of short-life and long-life fatigue, and a critical comparison of damage evolutions is conducted.

In the coming sections, first, the acoustic emission setup and preprocessing are described. Then, the structure and training of the algorithm are discussed. Finally, the results from the CAI fatigue tests are presented.

7.2 Experimental methodology and acoustic emission monitoring apparatus

Some of the tests presented in Chapter 2, were also monitored using acoustic emission. In this section, relevant aspects of testing are recalled, but for a more detailed description of manufacturing and testing please refer to Chapter 2. A set of compression fatigue tests were conducted on impacted coupons of CFRP. The impacted face was painted with a speckle pattern for DIC. Ultrasound monitoring was performed at interrupted testing to observe the growth of delamination. In addition to those monitoring strategies, opposite to the impacted surface, acoustic sensors were placed to perform real-time monitoring.

The used AE sensor was the AE1045SVS900 M, a broadband single-crystal piezoelectric transducer with an operational frequency range of 100–900 kHz supplied by Vallen Systeme GmbH. In addition, an external 34 dB pre-amplifier was used to amplify the recorded signals. To reduce noise, an acquisition threshold was set to 45 dB. The AE data was collected with a sampling frequency of 2 MHz by the AMSY-6 Vallen, 4-channel AE system. Ultrasound gel was applied to improve the coupling between the AE sensor and the specimen's surface. The two sensors were kept in position using plastic sensor holders glued to the non-impacted surface of the specimen. The performance of the AE system was validated before each test by conducting a standard pencil lead break procedure.

7.3 Acoustic emission data pre-processing, isolating damage waveforms and reducing data

Acoustic emissions are characterized by a high level of noise, friction, and reflections. Because of this, not all the waveforms that are recorded can be attributed to damage formation in the material. In addition to that, in fatigue tests the level of noise is higher compared to quasi-static tests, due to vibrations of the fixture. In the current work, an approach is proposed to reduce the data by isolating waveforms originating from damage propagation.

1. The first level of noise reduction consisted of applying a relatively high amplitude threshold for the acquisition of transient waveforms (60 dB). This was decided to reduce the noise and to work with a smaller size of AE data. However, it must be considered that AE signals originating from matrix micro cracking and other low energy damage modes may be excluded by setting a threshold this high.

2. It was assumed that, within the load cycle, damage is formed predominantly at high levels of compressive loads. This assumption follows the idea that damage is formed at high local stresses that occur when the compressive load is close to maximum. For this reason, only waveforms recorded at a load level superior to 80% of maximum compressive stress were analyzed.

3. To monitor the propagation of damage from the impact area, it was decided to analyze only the signals that could be located in the area between the sensors. This was done by performing a 1-D localization using the time of arrival difference between the two sensors. Only the hits that were recorded by the two sensors with a time difference

Δt inferior to the distance between the two sensors Δx multiplied by a factor of 1.5 and divided by the speed of sound a in the CFRP (3000 m/s) were accepted.

$$\Delta t < 1.5\frac{\Delta x}{a} \tag{7.1}$$

Thanks to this procedure, it was possible to exclude from the analysis events that could not be localized in the area separating the two AE sensors (Figure 7.2).

4. The analysis of the waveforms recorded with this setting revealed a low frequency (60 kHz) continuous-type signal associated with friction. Signals coming from damage are expected to be burst-type signals, rising and decaying in a very short time, while friction and noise are assumed to be a more 'continuous' type of signal. Considering this, a high pass filter allowing only frequencies >70 kHz was applied.

The selected waveforms were then transformed using continuum Morlet wavelet and the derived coefficient matrices were fed to the CNN classifier as gray scale images.

7.4 Image preparation and building the training dataset

The individuation of waveforms representing specific damage modes was the outcome of the experiments presented in Chapter 5. The knowledge obtained in the preliminary tests is now used as ground truth to develop a classifier based on wavelet scalograms. To perform a classification task, a training set has to be constructed. The set should contain labeled data equally representing each class. In the current implementation of the classifier, 4 classes were introduced representing the four damage modes shown in Figure 5.5 of Chapter 5. A fifth class was used to collect the waveforms that, for various reasons, could not be assigned to a single class of the four damage modes. Using the acoustic emission data of preliminary tests in chapter 5 and CAI fatigue tests, waveforms of the preliminary tests were manually assigned to different classes.

To precisely build the training set the following methodology was adopted. In each acoustic event, the data from sensor 1 and sensor 2 was extracted and a continuum Morlet wavelet transform was performed as described in Chapter 5. To perform image classification, the level of detail of the image should be as accurate as possible. For this reason, it was decided to adopt continuum wavelet transform (Chapter 5) instead of wavelet packet transform (Chapter 6). Ae recorded in quasi-static CAI, preliminary tests of Chapter 5 and first load cycles of CFAI were used in the training.

The scalograms of the waveforms reaching the two sensors (Figure 7.2) were then located next to each other forming one single image. At this point, a labeling decision was taken by visually examining the waveform. Only the events where each sensor observed the same waveform type were included in the four classes representing the damage modes. This was done because it was assumed that an event originating at the impact damage (center between the sensors) should reach the sensors with a short time difference and similar features. A final class was added collecting scalograms characterized by superimposed waveforms, mismatching signals between the two sensors, and waveforms that could not be classified with certainty by a human user.

All the classes were initially composed of a different number of waves. This should not be a surprise since, for instance, fiber failures are not as frequent as matrix failures. For this reason, a data augmentation strategy was tailored to have the same number of waveforms representing each class in the training. The data augmentation was achieved by shifting the target waveform in their respective time windows. This was done to augment the data but as an effect, it made the algorithm more robust and capable of classifying waves regardless of the position in the time window. Once the images were labeled, a data reduction was operated by max-pooling each image in 2x4 windows. After trying multiple reductions the adopted max pooling was considered a satisfactory trade-off between data size and the classification performance. The obtained labeled data was randomly shuffled and separated into 10'000 training images, 2'000 validation images, and 1'000 test images. The preparation of the acoustic signals before being fed into the CNN algorithm is presented in Figure 7.2.

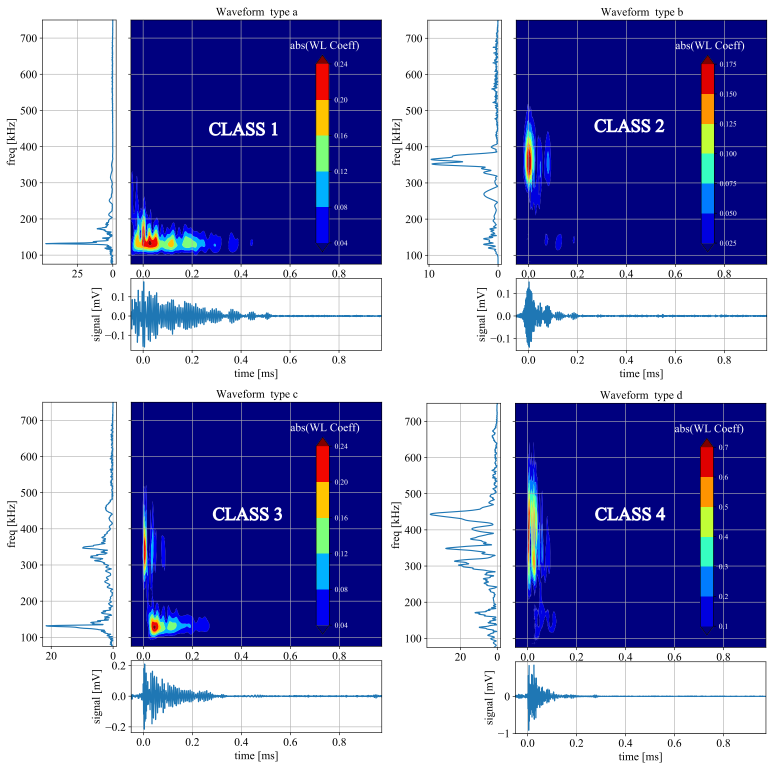

Figure 7.1: Typical scalogram of the four classes assigned to the different damage modes in the preliminary test of Chapter 5

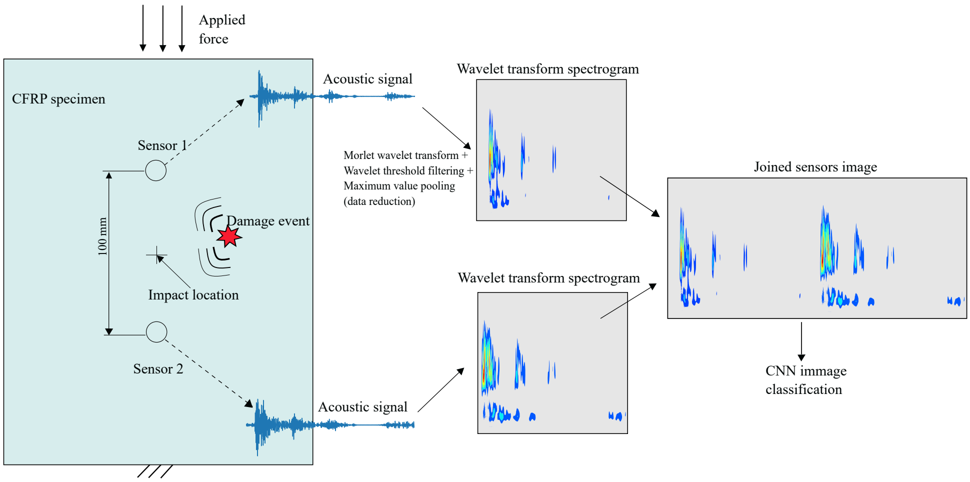

Figure 7.2: Data processing from sensor data to input of the CNN. Continuum Morlet waveform transform is applied to the acoustic signal in the two sensors. Then the two scalograms are joined to form a single image.

7.5 CNN ALGORITHM DESCRIPTION AND TRAINING RESULTS

A Convolutional Neural Network (CNN) is a deep learning algorithm particolarly effective in processing visual data like images. In CNN small matrices called kernels (or filters) are used to extract features from input images. During the convolution operation, the kernel slides over the input image (which is a matrix of coefficients), computing dot products between its values and the corresponding region of the image. This process effectively captures patterns such as edges, textures, or shapes present in the image. By learning the optimal values for these filters through training, the CNN can adaptively extract relevant features, which can be used for tasks like object recognition or image classification.

In the presented work, a CNN algorithm for image classification was implemented in Python using the 'tensorflow.keras' library [1]. The structure of the CNN algorithm is graphically represented in figure 7.3. The input is an (80 x 256) matrix, representing the scalograms of the two waveforms reaching the two sensors pre-processed with the scheme discussed in the previous section.

The first convolutional layer consists of 32 filters with a kernel size of 3x3, employing the Rectified Linear Unit (ReLU) activation function. A regularization term with an L2 penalty (weight decay) of 0.01 is incorporated. Padding is applied to ensure the spatial dimensions remain the same after convolution. A max-pooling layer follows with a pool size of 2x2 and padding to maintain spatial information. The process is repeated with a second convolutional layer consisting of 64 filters, and a max-pooling layer with a pool size of 2x2 mirroring the structure of the first. The output from the convolutional layers is flattened and fed into a densely connected layer with 128 neurons and the ReLU activation function. To prevent overfitting, a dropout layer with a dropout rate of 0.2 is introduced. The final layer is a dense layer with a softmax activation function. This layer produces the probability distribution over the 5 classes for the final classification.

The algorithm was trained on a dataset of 10'000 images divided into 5 classes. The validation set was composed of 2'000 images while a test set of 1'000 labeled images was used to perform an unbiased test of the trained algorithm. A batch size of 400 pictures is used in the training. In figure 7.4 the training accuracy, training loss, validation accuracy, and validation loss are plotted over the 200 training epochs. The loss function was calculated with categorical cross-entropy, which is specifically designed for multi-class classification problems where the target variable is categorical and has more than two classes. The categorical cross-entropy loss function quantifies the dissimilarity between the predicted probabilities and the true categorical labels. It penalizes the model more when it predicts probabilities that are far from the actual labels, and it encourages the model to output higher probabilities for the true class. Accuracy instead is defined as the ratio between the number of correct predictions and the total number of predictions. As shown in the plot, an accuracy of 98% in the validation set classification is reached after 100 epochs. In the 1000 images test set a loss of 0.06 and test accuracy of 98% was obtained.

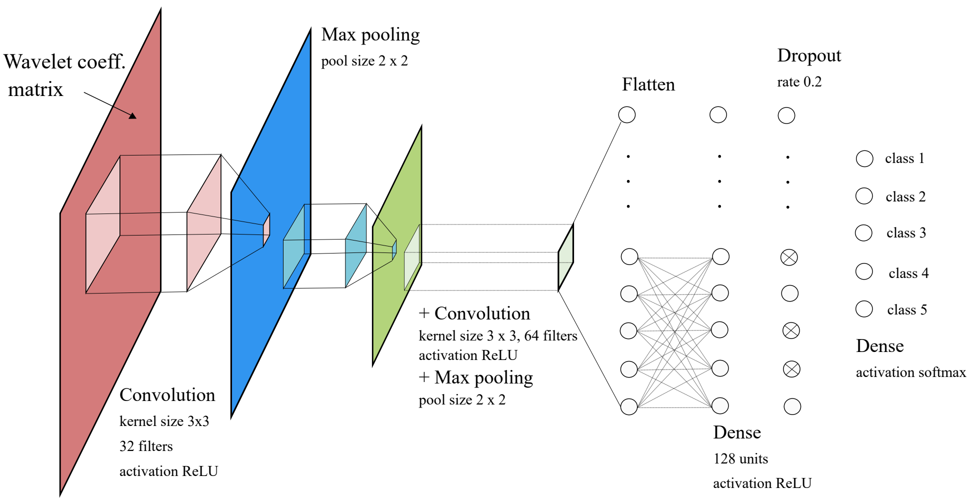

Figure 7.3: Structure of the CNN algorithm. The original images pass through a series of convolution and max pooling layers. Then a dense layer and a dropout are present. Finally dense layer with soft-max activation allows to compute the probability of each class

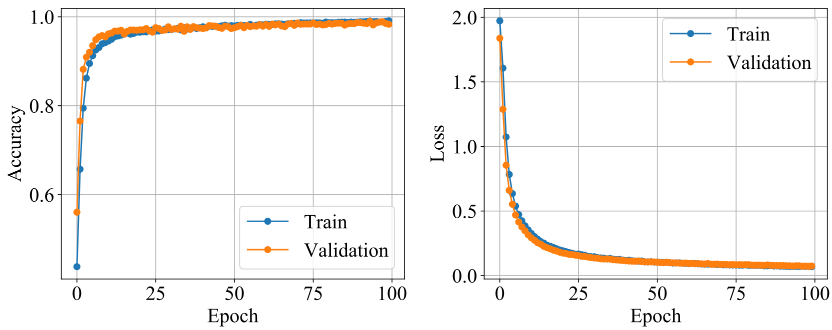

Figure 7.4: Performance of the training. The accuracy and the loss progression in the training and validation set are shown over the epochs. A good convergence is reached at 100 epochs.

7.6 Solution to the events superposition effect

Analyzing the results of the test set, some considerations can be made. The algorithm is capable of successfully individuating specific patterns in relatively noisy backgrounds. When the algorithm has to classify a waveform composed of multiple events, if there is one clear winner in both sensors in terms of wavelet coefficients, it provides a correct classification. In case there is no clear winner, however, the waveform is placed under class 5. During training, this class has been added to collect waveforms that could not be easily linked to a specific damage mode by the human operator.

7

Many of the waveforms in class 5 were characterized by the superposition of different hits. This can be observed in the scalogram by the overlap of wavelet signatures traceable to different damage modes. To classify the waveforms in this situation, a processing strategy is now proposed. It consists of an image pre-processing pipeline that allows for the selective isolation and examination of significant features within the original scalogram, to be handled separately by the CNN classification.

Starting from the wavelet coefficient matrix, a threshold operation is applied to create a binary image, where pixels with intensities below a dynamically set threshold (35% of the maximum intensity in the original image) are set to 0, while those above are set to 1. Connected components labeling is then employed to identify clusters within the binary image. The three more relevant clusters, based on their maximum original intensity, before transforming into binary images, are then extracted into separate images. Only after the segmentation of the image has been performed, the image size is reduced following the procedure of figure 7.2 and fed to the classifier. In conclusion, new images are created to be fed to the classifier individually to determine by which damage modes the waveform is composed. With this strategy is possible to classify complex waveforms characterized by the superposition of different acoustic events (Figure 7.5).

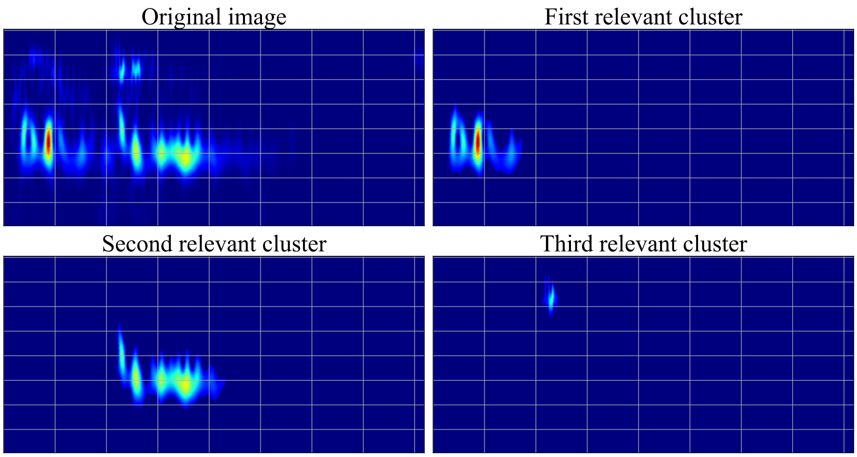

Figure 7.5: Thanks to the segmentation algorithm it is possible to divide complex scalograms with events superposition in sub-images to be handled separately

7.7 CAI fatigue damage mode repartition results

Once trained, the CNN algorithm was used to perform a study on the distribution of damage modes in fatigue tests. The goal of the study was to compare short-life and long-life fatigue progressions. Specimens s3 and s4 discussed in Chapter 2 serve as representatives of the two conditions.

In Figures 7.6 and 7.7, the cumulative counts of the different classes (with the damage mode assignments discussed in Chapter 5) and the cumulative acoustic signal energy (defined in Table 5.2) per class are reported for the two specimens. The preprocessing of signals, which included filtering based on maximum amplitude, load level, and 1-dimensional localization, significantly reduced the amount of data to be analyzed. Starting from several million waveforms, the data was reduced to a few thousand waves that passed the preliminary tests and were considered to originate from damage propagation.

In the long-life fatigue test, the acoustic emission system was active for a number of cycles 30 times higher than the short-life test. Because of that, in the long-life fatigue test, the AE system recorded a number of signals which was orders of magnitude larger than in the short-life tests. After applying the hit selection strategy exposed in section 7.3 however, the number of hits was significantly reduced in the long-life fatigue tests and was only one order of magnitude higher compared to the short-life test.
To explain why this happens, let's now assume that in a fatigue test acoustic emissions are recorded with no filtering of any type. In this case parts of the recorded signals are related to damage, while the rest is related to friction and noise. Among these sources, noise and friction signals increase with the number of cycles. On the opposite, the signals originating from damage depend on the propagation of damage itself. It is reasonable to assume that the additional number of recorded signals in long-life fatigue tests (with respect to short-life) is in large part due to a higher number of noise and friction signals

being recorded, which are independent on the size increase of damage but highly dependent on the number of cycles. It is not a surprise that, after selecting the hits originating from damage propagation, we end up with a total number of events which is comparable despite the large difference in the raw data.

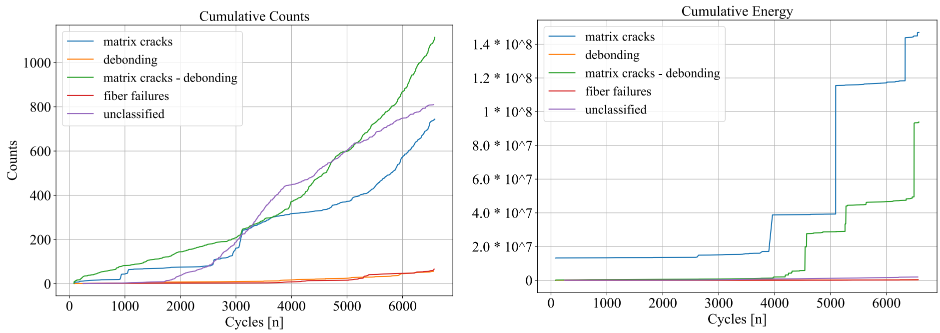

Figure 7.6: Damage modes repartition plots in specimen s4 (short life). In the left plot, the progression of cumulative count in fatigue life is shown for every damage mode. On the right, the cumulative ae signal energy is shown (defined in Table 5.2).

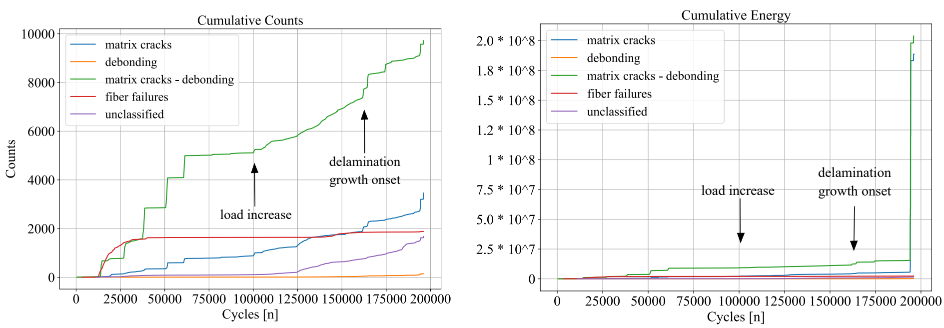

Figure 7.7: Damage modes repartition plots in specimen s3 (long life). In the left plot, the progression of cumulative count in fatigue life is shown for every damage mode. On the right the cumulative signal energy (defined in Table 5.2) is shown for every damage mode.

Adding to the previous point, the difference in the total released energy at the end of the short and long-life fatigue tests has the same order of magnitude in the two tests (Figures 7.7 and 7.6). This shows that despite the largely different number of cycles, if only damage events are included and noise and friction are removed, the total acoustic energy recorded in long-life and short-life tests is comparable.

In both tests, there was a significant number of events that were assigned to class 5 by the CNN algorithm. In fact, the count of 'class 5' events was comparable to the count of matrix crack's related events in specimen s3 (Figure 7.7) and specimen s4 (Figure 7.6). Besides being numerous, the non-classified events were generally characterized by a lower acoustic energy. This can be seen in the cumulative energy logarithmic plots (Figures 7.8). To explain this effect, we must consider that 'class 5' refers to waveforms that are not easily assigned to the four damage modes identified by preliminary tests. By analyzing these waveforms in the tests, it was noted that they were characterized by many events superimposed. If an high energy event corresponding to one damage mode is present in the time window, its coefficients dominate the entire scalogram and the CNN locates it in the correct class, even if it overlaps with other events. On the contrary, if many hits of lower energy are superimposed and there is not a 'clear winner', the scalogram is complex and difficult to classify. Signals assigned to class 5, belong to the latter case and tend to have a lower energy.

In the previous section, image segmentation was proposed as a strategy to decompose these complex spectrograms and analyze the different events separately. In the present implementation, this strategy was not applied. It was decided to not focus on this class of waveform due to their on average lower acoustic energy and time constraint of the project. This is however an interesting aspect to investigate in future research. In the following sections, the propagation of damage in fatigue in short life and long life are discussed.

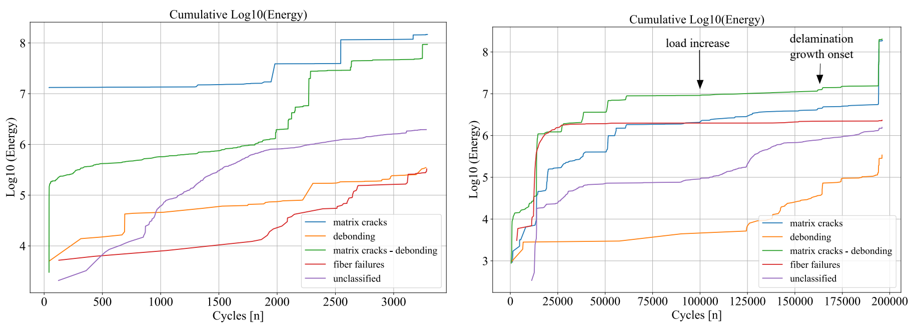

(a) specimen s4 (short fatigue life). (b) specimen s3 (long fatigue life).

Figure 7.8: Cumulative signal energy plot in logarithmic scale

7.7.1 Short-life fatigue

The acoustic emission monitoring of specimen s4 is shown in Figures 7.6 and 7.8 (a). Recalling the results of Chapter 2, this specimen was characterized by a constant progression of delamination and a constant degradation of axial stiffness. The study of damage accumulation with acoustic emission also reveals an incremental acoustic activity, compatible with a progressive propagation of damage occupying the entire fatigue life. This can be observed in the cumulative counts' plot (Figure 7.6 (a)), where events associated with matrix cracks and the combination of matrix cracks and debonding are added progressively.

Looking at the cumulative energy plot (Figure 7.6 (a)), matrix cracks and the combination of matrix cracks and debonding are by far the most relevant damage modes in terms of total released energy. Some fiber failures are recorded from the beginning of the test. This makes sense considering that the compression test started in an impacted specimen. While in a pristine specimen, one could expect to observe fiber failure close to the end of the fatigue life, in this case, fibers that have been weakened during impact start to fail in the first cycles.

Opposite to counts, which seem to be added quite regularly throughout the fatigue life, energy is released with a step-wise increase, alternating high-energy events with lower-energy events (Figure 7.6).

Looking at the logarithmic plot of cumulative energy (Figure **??**), a high-energy matrix crack event can be observed at the very beginning of the fatigue test. In the early stages of fatigue, there is also a noticeable activity of events assigned to a mixture of matrix crack-debonding. This result aligns with the early growth of delamination observed with ultrasounds and digital image correlation.

7.7.2 Long-life fatigue

The acoustic emission evolution of specimen s3, which exhibited a long life, is shown in Figures 7.7 and 7.9. Recalling the results of Chapter 2, this specimen was characterized by an initial phase of no delamination propagation, as evaluated with ultrasound and digital image correlation measurements. In this phase, no significant stiffness degradation was observed either. After 101,000 cycles, since no growth was observed, it was decided to increase the load, and after a second block of approximately 94,000 cycles, the specimen failed.

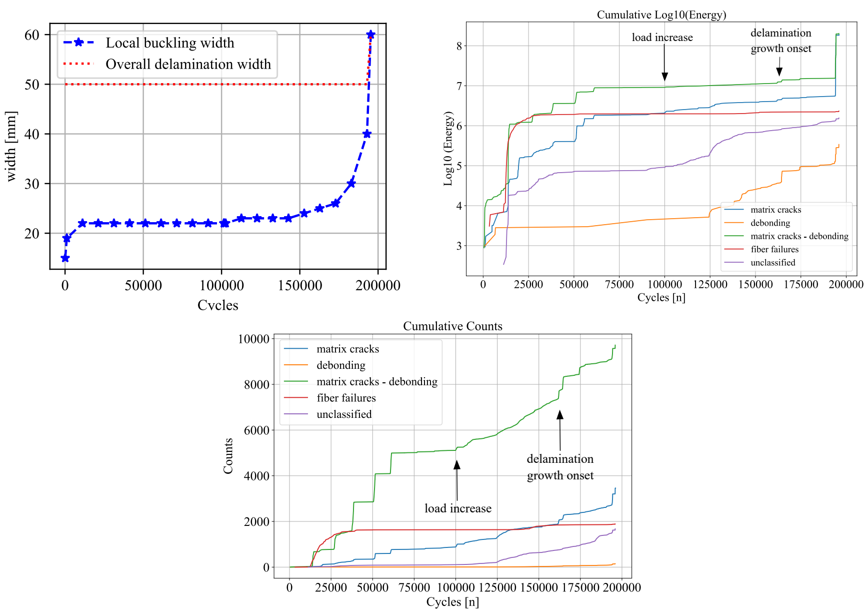

Figure 7.9: Specimen s3 delamination propagation evaluated indirectly with DIC buckle size on the left (Chapter 2), the logarithmic plot of the acoustic signal energy released by the different damage modes, and the cumulative sum of events associated to the different damage modes

Even with the new load, another phase of no detectable growth was observed with ultrasound inspection and DIC, followed by the onset of delamination growth, which occupied the final portion of the fatigue life.

Comparing the acoustic emission results to the damage propagation of Chapter 2, a correspondence can be found and different phases of damage accumulation can be highlighted (Figure 7.9):

1. In the early stages of fatigue life, an increase in the cumulative counts of different damage modes is observed. In this initial phase, it is possible that substructures partially damaged during the impact failed in the following compression cycles. This can be seen as a transition of the impact damage, which was formed in an out-of-plane loading, but then undergoes an in-plane load. During this initial section of fatigue life, many high-frequency events belonging to class 4 related to fiber failures were recorded. This class of events can be attributed to residual failures resulting from impact damage occurring in the first cycles. These events were considered to be quite high in number to be easily attributed to fiber failure. For this reason, the author performed a visual check and these waveforms corresponded in fact to the class 4 waves individuated in Chapter 5.

2. Following this first phase of initial damage 'stabilization', a steady phase with no apparent damage propagation was observed. In this phase, the curve of the cumulative counts looks flat for all damage modes. During this phase, also no obvious degradation of stiffness was observed. The combination of acoustic emission monitoring with ultrasound inspection and DIC suggests that during this portion of fatigue life, no significant damage propagation occurred in the specimen.

3. After the load was increased at 101,000 cycles, an increasing trend in cumulative counts was observed (Figure 7.7). While counts were added regularly, acoustic energy was released in small packets, meaning that no high-energy single events were recorded in this phase. Also in this part of the fatigue life, no obvious degradation of stiffness and no significant delamination growth were observed (a part of a small increase in delamination size immediately after the load change). This result suggests that although no growth was observed using ultrasound inspection and DIC during this phase, the damage was propagating in the form of small matrix cracks and debonding. Compared to the previous phase, now low-energy acoustic events related to pure matrix cracking and the mixture of matrix cracking and debonding are added regularly and progressively. It must be noted that, without acoustic emission monitoring, this phase and the previous one would not be distinguishable. According to the ultrasound inspections, DIC and compliance monitoring presented in Chapter 2, they were both 'no-growth' phases.

4. An abrupt increase in cumulative counts of events associated with matrix cracking and the combination of matrix cracking-debonding determined the onset of a new phase in damage propagation. From this moment, progressive degradation in the compliance of the specimen together with the obvious propagation of delamination was detected with ultrasound monitoring and DIC.

In agreement with the short-life fatigue test, the most energetic damage modes were the combination of debonding and matrix cracks and pure matrix cracks. Despite the increase in event counts from earlier stages, the highest release of energy occupies only the final part of the fatigue life, where delamination propagation was observable with ultrasound scanning.

7.8 Acoustic emission signature for the onset of impact delamination growth

If the results of specimen s3 are analyzed in terms of the accumulation of logarithmic energy (Figure 7.9), an interesting fact can be observed. The onset of shallow delamination growth observed with ultrasound inspections and with DIC buckling area increase, as discussed in Chapter 2, happened in correspondence to the significant accumulation of acoustic energy associated with a combination of debonding and matrix cracking and pure matrix cracking. The reader must consider that the plots of Figure 7.9, are presented in logarithmic scale. This means that although they look similar, the increase in energy related to the combination of matrix cracking and delamination is higher compared to the other damage modes. In this phase, an abrupt increase in the counts related to the mixture of matrix crack and debonding was also observable.

In Chapter 6, it was observed how the onset of unstable damage accumulation in static CAI tests started with high acoustic energy events belonging to the same type (Figure 6.5). It was hypothesized that this event could be representative of the onset of delamination growth in static tests. Results from fatigue tests show that, in correspondence with the onset of growth of delamination, a similar type of acoustic event can be observed. This seems to support the hypothesis that high-energy acoustic events of this type are a signature of the onset of delamination propagation in CAI tests.

In fact, in the short-life Fatigue test (7.8) relatively high-energy events related to matrix cracks and a combination of debonding and matrix cracks are recorded at the beginning of the test. In this test, the growth of delamination and stiffness degradation happened from the beginning of fatigue life.

7.9 Conclusions

A CNN algorithm was developed to classify waveform types based on wavelet transform coefficient matrices. The method successfully separated waveforms between different classes. As a proof of concept, it was shown that this approach, when nested with image segmentation, is capable of separating classes that are difficult to distinguish using traditional classification based on signal descriptors.

The CNN was then utilized to analyze and compare the fatigue after impact damage evolution of long-life and short-life specimens. A selection of hits based on localization, maximum amplitude, and load levels was applied to AE data to separate damage signals from friction and noise. After performing this hits selection, despite the significantly different number of cycles, long-life and short-life fatigue tests showed accumulated acoustic emission energy of the same order of magnitude.

The analysis with the CNN comparing the damage evolution in long and short life fatigue suggests that multiple damage activation thresholds exist in compression fatigue after impact. In particular, in the first phase of the long-life test, low-energy acoustic events occurred but after, damage propagation ceased, and a steady phase of minimal acoustic activity was observed. A load increase caused a new phase of gradual accumulation of low-energy acoustic events attributed to the growth of matrix cracks and debonding not detectable with ultrasound. Since the new phase started after the load increase, and before that the acoustic activity was almost absent, it's possible that without intervention, the specimen might not have exhibited any further growth. Further investigation is required to verify the presence of a first growth/no growth load threshold.

Towards the end of the long-life fatigue test, higher energy acoustic events marked the start of a phase characterized by delamination growth. The short-life fatigue specimen instead, exhibited a behavior compatible with this last phase from the beginning of fatigue life. Considering this, it is concluded that a second threshold, this time for the growth of delamination, may be present. The short life specimen, which was tested with a higher applied load, started the growth at the beginning of fatigue life. In the long life specimen instead, the previous phase of damage propagation was necessary to eventually trigger delamination growth. The phase of propagation happening prior to the onset of delamination was characterized by low energy acoustic events which were associated to matrix cracks and debonding of smaller size not detectable via ultrasound. It is unclear how precisely this phase of damage propagation triggered the start of delamination growth. One hypothesis is that the intralaminar matrix cracks reduced the axial stiffness of the sub laminates, increasing the opening displacement at the delamination front until eventually triggering the onset of delamination growth. However, buckling is not the only mechanism triggering delamination growth. Transverse cracks inside the plies can also trigger mode II delamination growth as explained in Section 2.3.6 of Chapter 2.

To conclude, results clearly indicate that the effect of varying maximum compression stress must be considered in the description of CAI fatigue. This is because, depending on the applied stress, phases of damage propagation characterized by different activities of the damage modes can take place. Changing the compressive stress applied to the impacted coupon not only affects the velocity of propagation and the expected fatigue life but also alters the 'history', i.e., the sequence of phases in damage propagation.

Finally, the same class of acoustic events marked the onset of unstable growth of damage in static CAI tests and the onset of delamination in fatigue CAI tests. It is hypothesized that this event constitutes a signature for the onset of delamination growth; however, to validate this assumption, more specimens must be tested.

References

[1] Martín Abadi, Ashish Agarwal, Paul Barham, Eugene Brevdo, Zhifeng Chen, Craig Citro, Greg S. Corrado, Andy Davis, Jeffrey Dean, Matthieu Devin, Sanjay Ghemawat, Ian Goodfellow, Andrew Harp, Geoffrey Irving, Michael Isard, Yangqing Jia, Rafal Jozefowicz, Lukasz Kaiser, Manjunath Kudlur, Josh Levenberg, Dandelion Mané, Rajat Monga, Sherry Moore, Derek Murray, Chris Olah, Mike Schuster, Jonathon Shlens, Benoit Steiner, Ilya Sutskever, Kunal Talwar, Paul Tucker, Vincent Vanhoucke, Vijay Vasudevan, Fernanda Viégas, Oriol Vinyals, Pete Warden, Martin Wattenberg, Martin Wicke, Yuan Yu, and Xiaoqiang Zheng. TensorFlow: Large-scale machine learning on heterogeneous systems, 2015. Software available from tensorflow.org.

8

Conclusion

Fatigue after impact in composite laminates cannot be reduced to a delamination growth discussion since much more happens below the surface. To correctly describe the fatigue after impact process, different damage processes activated at different load levels have to be considered. In this chapter, the general conclusions of the thesis are presented alongside recommendations for inspection, monitoring and future research.

8.1 Aim of the thesis

The literature review presented in the introduction of this thesis has shown that despite several experiments being performed in the past, knowledge gaps persist in characterizing fatigue growth in impacted CFRP materials. To summarize, it remains unclear how the fatigue limit should be defined and what determines the onset of fatigue damage growth in impacted CFRP coupons. Additionally, once the fatigue process starts, it is uncertain how the damage propagates from its initial state to the advanced delamination growth often observed with ultrasound inspections. Given these uncertainties, it was decided at the beginning of the research to investigate the following research question:
How can we describe fatigue growth after impact in CFRP?
This fundamental question was broken down into the following sub-questions:

- Which mechanisms are at play during fatigue growth after impact damage propagation?
- How can we explain the discrepancies in previous experiments monitoring fatigue growth after impact?
- How accurately do commonly performed tests represent fatigue growth after impact in a real structure?
- How general is the observed propagation concerning different stress amplitudes and initial impact damage configurations?

Considering the initial aim and scope of the research, this chapter collects the main conclusions of the thesis, discussing their relevance in overcoming the identified knowledge gaps. In the first section, the synthesis of all the experimental investigations presented in the thesis is provided, combining various monitoring and inspection strategies. This synthesis offers an updated description of the phenomenology of CAI fatigue at different load levels. Then a section is dedicated to discussing how this description relates to previous results in the literature. In the following sections, the implications of this description on damage-tolerant design and the generality and scalability of the tests are discussed. Finally, the chapter presents a series of recommendations for inspections and for future research.

8.2 Phenomenology of CAI fatigue at different load levels

Fatigue after impact cannot be reduced to delamination projected areal growth discussion since much more is happening below the surface. The ultrasound analysis of CAI fatigue experiments presented in (Chapter 2), revealed two mechanisms that are not captured if projected area or width is considered. The through-thickness transmission scan showed initial growth in the non-delaminated cone, a phenomenon previously documented only in quasi-static CAI tests. The echo-pulse scan revealed the initial growth of superficial shorter delaminations within the projected delamination impact area. Both of these phenomena occurred before the onset of delamination growth perpendicular to the loading direction, extending beyond the projected delamination area. It was noted that many previous studies, that monitored the overall width and area of delamination, may have overlooked these features in their growth descriptions.

Adopting the wrong damage descriptor can indeed lead to a misinterpretation of the results. To prove this, digital image correlation was utilized to indirectly measure shallow delamination growth near the impacted surface by assessing local buckling width (Chapter 2). This method tracked the preferential growth of short delaminations observed in echo pulse scans while allowing for more frequent data acquisition. The analysis revealed that, in the case of a short-life specimen, considering the growth of shorter delaminations showed progressive damage propagation throughout the entire fatigue life. However, if only the projected area or width had been monitored, a phase of no-growth followed by delamination growth would have been observed instead.

Not all the delamination 'no growth' phases observed in previous literature however, can be attributed to the use of wrong damage descriptors. Performing the DIC analysis in a long-life fatigue test yielded different results (Chapter 2). In this instance, the delamination propagation curves indicated the presence of an initial no-growth phase, even when using a more precise damage descriptor. This behavior was further supported by the axial compliance curve (also discussed in Chapter 2). These findings suggest that the behavior of fatigue damage propagation varies depending on the applied load and the local stresses within the impact damage area. When the applied stress surpasses a certain threshold level, delamination growth starts at the beginning of fatigue life. Conversely, if the applied stress is lower, a transitional phase occurs wherein other damage modes or shadowed delaminations may become active.

In fact, different damage modes are activated within the structure at different load levels compatible with fatigue. This is shown in the acoustic emission monitoring of static CAI tests presented in Chapter 6. In all specimens, the onset of unstable damage accumulation was initiated by an intermediate frequency acoustic event, associated with a combination of debonding and matrix cracking, occurring at 80% of failure displacement. The identification of an acoustic event triggering unstable damage accumulation in static tests was linked to the concept of a threshold for delamination growth under fatigue, as introduced in Chapter 2. In the static test it was observed that different phases of damage propagation and different damage modes repartition take place at different load levels.

Varying phases of fatigue damage propagation are observed depending on the maximum applied stress and the activated damage modes. In Chapter 7, a CNN algorithm was developed to classify recorded waveforms based on wavelet coefficient and associate them with damage modes. The analysis suggests that multiple damage activation thresholds exist in compression fatigue after impact. This result was obtained by comparing the damage propagation in fatigue of short and long life fatigue specimens. The damage propagation in the long-life specimen was synthesized into four phases.

phase 1: Initial low energy events due to failure of partially damaged substructures.

phase 2: Deactivation of damage growth.

phase 3: Reactivation of damage growth after a load increase and gradual accumulation of damage that could only be detected by acoustic emissions.

phase 4: Final delamination growth.

The short-life fatigue specimen instead exhibited from the beginning a behavior compatible with phase 4 i.e. gradual increase of delamination.

Notably, a load increase was applied before passing from phase 2 to phase 3 in the long-life specimen. It's conceivable that without intervention, the specimen might not have exhibited any further growth. This suggests the presence of a first growth/no growth load threshold.

A similar reasoning can be made for the transition between phase 3 and phase 4. While in the long-life fatigue test, higher energy acoustic events, classified as a mix of matrix crack and debonding, marked the start of the final fatigue phase of delamination growth, in the short-life fatigue specimen delamination growth happened from the beginning of fatigue life. Considering this, it is concluded that a threshold for growth of delamination may be present. The short life specimen, which exceeded this value, started the growth at the beginning of fatigue life. In the long-life specimen instead, previous phases of damage propagation were necessary to trigger the onset of delamination growth.

In conclusion, the results clearly indicate that the effect of varying maximum compressive stress must be considered in the description of CAI fatigue. This is because, depending on the applied stress, phases of damage propagation characterized by different activities of the damage modes can take place. Changing the compressive stress applied to the impacted coupon not only affects the velocity of propagation and the expected fatigue life but also alters the 'history', i.e., the sequence of phases in damage propagation.

8.3 Explaining the discrepancy in the previous literature

Before the present work, several experimental studies have described delamination growth using overall width or projected area. One test [1] reported a phase in which no fatigue growth happened outside of the impact delamination projected area followed by the fast and unstable growth of a single delamination. In another experiment [2], no delamination growth was observed in inspections until the failure of the specimen. In two tests [3, 4], an initial growth of delamination width was observed, followed by a phase of no apparent growth followed by a third phase of fast and unstable growth which led to failure. Finally, in other experiments, a gradual growth of delamination outside the damaged envelope was observed from the beginning of fatigue life [5, 6]. The discrepancy of these observations was highlighted as one of the challenges to overcome in the review by Davies and Irving [7].

Considering the description of damage propagation provided in this thesis, two explanations are individuated in a) the use of imprecise damage descriptors and b) the effect of different stress levels.

Through-thickness transmission scans presented in Chapter 2 revealed growth in the non-delaminated cone while the echo-pulse scans presented in Chapter 2 detected the preferential growth of superficial shorter delaminations within the projected delamination impact area. Both observations occurred before the onset of delamination growth perpendicular to the loading direction extending beyond the projected impact damage area. Many previous studies focusing on the overall width and area of delamination may have overlooked these features in their growth descriptions. It is possible that instances where a plateau or 'no-growth' phase was observed before the sudden onset of delamination growth in prior literature, could have been due to undetected delamination growth, as suggested by Pascoe [8].

Furthermore, in most studies, the applied load is defined as a percentage of residual static compressive strength after impact (CSAI). While this facilitates the comparison of fatigue lives in specimens with different initial damage sizes, it poses challenges. The compression after impact strength value is either statistically derived from other specimens impacted under similar conditions (but never identical) or calculated using models attempting to estimate residual strength from impact damage. Since the load is defined in this way, there may be large differences in local stresses within the impact damage even in tests conducted at similar estimated percentages of CSAI. The previous sections have shown how different types of evolution are expected at different applied loads. This shows that some of the differing trends in fatigue growth observed in the literature may in fact be attributed to variations in load levels.

The conclusions from this thesis can be contextualized with two CFAI tests performed in the past using the ASTM CAI standard fixture [9] on similar CFRP with the same stacking sequence adopted in this thesis. Xu et al. [1] performed a CFAI test at a maximum compression fatigue load of 77% of the estimated CSAI. The test resulted in a relatively short fatigue life of 6500 cycles. In their test, only an attenuation scan was used and the projected width of delamination (in the transverse to the load direction) was tracked. They reported a first phase of no growth, followed by a phase of fast increase of delamination projected width. In this test, a decrease in compliance was observed even in the absence of projected delamination width growth. Considering the short fatigue life and the observed decrease in compliance, it is possible that in this case, the growth of shorter delamination started at the beginning of fatigue life but was undetected for a large part of fatigue. Ogasawara et al. [2] also performed a CFAI and obtained a long fatigue life of 1.23 x 10^6 cycles. In this case, no damage growth was observed in the various inspections performed using ultrasound attenuation scan. Images of the surface of the specimen however indicate a fast and unstable growth of elongated local buckling, which took place in the last portion of fatigue life not captured via inspection. In this case, due to the long life of the test, it is possible that a behavior composed of multiple phases, similar to the one reported in this thesis' long-life specimen, happened instead.

8.4 Implications on damage tolerant design and potential for 'slow growth' approach

The description of fatigue growth provided in this thesis, highlights the importance of assigning the correct target number of cycles in the no-growth certification procedure implemented via ultrasound inspections. The damage propagation phases 2 and 3, as defined in section 7.7.2, did not show any growth via ultrasound inspection. However, while case 2 had a stable acoustic emission activity which seemed to reduce over time, phase 3, after small load increase, had an incremental accumulation of damage (undetected via the ultrasound) determining the onset of the unstable phase. This means that, if the target number of cycle is not properly set, and growth is only measured via ultrasound, it's possible to have instability leading to failure in few cycles after the target life.

The description of CAI damage propagation provided in this thesis shows that there is no room for the application of the slow growth approach if standard coupon tests are considered. To apply a slow-growth approach, the designer has to ensure a slow stable behavior and be able to predict it [10, 11]. The results presented in Chapter 7, seem to indicate that there is no room for the application of slow growth. In fact, during phases 1 to 3 (section 8.2), the growth could not be measured. Once a measurable growth started, in phase 4, it happened in a fast and unstable manner, leading to failure in a short time.

There may be potentially a 'slow growth' behavior in the context of planar delamination growth in compression fatigue if some conditions are respected. In Chapter 4 of this thesis, a surrogate impact delamination envelope was manufactured using PTFE inserts and tested under fatigue. The edges of the PTFE inserts constituted an initiation site for delamination growth. In fatigue, delaminations and local buckle progressed perpendicular to load towards the lateral edges. A more detailed analysis of the C-scan results, however, revealed some differences in local buckling allowing for large mode I opening and lower ply stress in the surrogate compared to CAI fatigue growth. Despite those differences, the fatigue growth of multiple planar delaminations in compression fatigue was obtained, a condition encountered also in the CAI fatigue advanced state, described as phase 4 in section 8.2. Opposite to CAI fatigue tests, the growth of delaminations in the surrogates proved to be slow and stable accompanied by a gradual decrease in compliance. These results indicate that a slow growth behavior in planar delamination compression fatigue is possible under certain conditions. Further research is needed to verify if this behavior can be actually observed in fatigue after impact scenarios of real structures.

8.5 Generality of the results and scalability of the test

There is a high dependency of the expected growth on the test setup and the initial impact damage configuration.

The numerical analysis reported in Chapter 4 shows that, in the case of a simplified surrogate of impact damage, a state with global buckling without restrictions promotes the increase of SERR in a single interface of the laminate. On the contrary, suppressed global buckling and enhanced local buckling produce high SERR in multiple interfaces of the laminate. In many applications, the ratio between impact damage and the size of the plate tends to be larger. This means that in many applications the impacted structure is more likely to undergo a global buckling. This has implications on the scalability of the test result, but also on how the inspection results have to be interpreted. If an increase in projected area is detected with ultrasounds, in case of growth of single delamination this corresponds to the same increase in total delaminated area. In case multiple delaminations are growing at the same time, this corresponds to a much larger increase in the total delaminated area.

A further numerical analysis performed in Chapter 4 shows that, in the case of a central non-delaminated circular area in a simplified surrogate of impact damage, a reduction in the size of this area increases the mode *II* strain energy release rates in the internal front. This indicates that a smaller central non-delaminated area is more likely to face delamination growth compared to a large one. With the presence of internal non-delaminated region linked to out-of-plane compression stress during the impact, the results suggest that different impactor-head geometry may result in different expected growth of impact delamination in fatigue. The modeling approach has several limitations, which are discussed in chapter 4. To capture with high fidelity the growth in a simulation, initial damage must be represented in the model with higher accuracy. Then a growth simulation must be run, since capturing the initial SERR distribution only serves to determine the most likely location of initial growth. Despite the limitations, this approach show the potential sensitivity of the results on the central non-delaminated area, an aspect that is usually neglected in the literature.

8.6 Recommendations for inspection and monitoring in fatigue tests

Results of this thesis indicate that projected delamination area or width is not a sufficient metric to capture fatigue after impact delamination growth. The results presented in Chapter 2 reveal at least two delamination mechanisms that are not captured by measuring projected area/width: the growth of shorter delaminations and the growth inside the central non-delaminated cone. Those mechanisms were observed thanks to a combination of pulse-echo and through transmission. It is unclear how these phenomena contribute to strength degradation, hence, when it's possible, a combination of pulse-echo and through transmission scan is recommended.

When ultrasounds are not capable of capturing the growth, damage propagation can be detected using acoustic emission (Chapter 7). Phase 3 of damage propagation of the long life specimen (section 8.2) was characterized by damage propagation recorded with acoustic emission but undetected via ultrasounds.

Concerning acoustic emissions, a series of technical recommendations can be formulated based on the experience maturated in this thesis. First of all, wavelet transform is a superior approach to precisely distinguish waveform originating from different damage modes even in some cases of events superposition (Chapter 5). Analyzing the waveforms originating in an entire fatigue test is possible if a proper selection of events is performed. In this work, events were critically selected based on the load level and their localization. This allowed to train and use a CNN able to classify acoustic events and provide information about the different damage modes throughout the entire fatigue life. More generally, this thesis shows once more that combining a series of inspection and monitoring strategies provides a superior description of impact damage propagation.

8.7 Recommendations for future research

Drawing from the results and experience gained, some concrete suggestions for further investigation are now presented.

The hypothesis that was advanced in chapter 2, is that load thresholds may exist which determine different evolution in fatigue life, such as the immediate growth of delamination, a phase of transition before delamination or a no-growth behavior. This was supported by the observation performed in chapters 6 and 7 showing with acoustic emission the activation of different mechanisms at different load levels. In particular, the results presented in Chapter 7, show a phase of reduced acoustic emission activity (phase 2) linked to no significant growth, and a phase of incremental acoustic activity (phase 3) linked to the growth of damage undetected via other methods leading to instability. Quite interestingly, the passage from Phase 2 to Phase 3 was triggered by a load increase and was immediately detectable via acoustic emissions. It is possible that combining acoustic emission studies with a better understanding of the different damage mechanisms at different load amplitudes could allow to link the acoustic activity at the beginning of the test to ‘no-growth’ behavior, defined as no-strength degradation after a target number of cycles. Avoiding run-out tests would primarily reduce the testing time. In addition to that, working with small load variations and acoustic emission monitoring, would allow to determine with greater precision the no-growth limit value. Current research is still far from reaching this point. Further investigation is needed to establish the link between features in acoustic emission, fatigue damage propagation and the consequent strength degradation.

Chapter 6 highlighted the occurrence of a specific acoustic waveform at the onset of unstable damage growth in static CAI tests. This was hypothesized to be the signature of delamination onset, supported by a match with observed waveforms in fatigue after impact (Chapter 7). A practical next step could involve conducting interrupted static tests, stopping the test at the load level immediately after the one where the event is recorded, to verify the type of damage propagation that occurs. This approach is similar to the methodology employed by Bull et al. [12] and would provide an opportunity to establish connections between static and fatigue tests in CAI.

In past literature, impact damage propagation in fatigue has been often identified with the growth of delamination. In fact, delamination can be measured using ultrasound and can be linked to the familiar concept, originating from metal research, of an increase in flaw dimension progressing over cycles. The results from this thesis demonstrate that different ’histories’ of damage evolution (intended as sequence of phases) are possible for similar initial impact damage when the compressive load level is changed. Many of these do not involve an increase in damage area. The author suggests that fundamental research should prioritize explaining and describing this aspect.

References

[1] Fan Xu, Wenli Liu, and Phil E. Irving. Fatigue life and failure of impact-damaged carbon fibre composites under compressive cyclic loads. *ICCM International Conferences on Composite Materials*, 2017-Augus:20–25, 2017.

[2] Toshio Ogasawara, Sunao Sugimoto, Hisaya Katoh, and Takashi Ishikawa. Fatigue behavior and lifetime distribution of impact-damaged carbon fiber/toughened epoxy composites under compressive loading. *Advanced Composite Materials*, 22:65–78, 2013.

[3] A. S. Chen, D. P. Almond, and B. Harris. Impact damage growth in composites under fatigue conditions monitored by acoustography. *International Journal of Fatigue*, 24:257–261, 2002.

[4] Hongliang Tuo, Tao Wu, Zhixian Lu, and Xiaoping Ma. Evaluation of damage evolution of impacted composite laminates under fatigue loadings by infrared thermography and ultrasonic methods. *Polymer Testing*, 93, 1 2021.

[5] Milan Mitrovic, H. Thomas Hahn, Greg P. Carman, and Peter Shyprykevich. Effect of loading parameters on the fatigue behavior of impact damaged composite laminates. *Composites Science and Technology*, 59:2059–2078, 1999.

[6] G. Clark and T. J. Van Blaricum. Load spectrum modification effects on fatigue of impact-damaged carbon fibre composite coupons. *Composites*, 18:243–251, 1987.

[7] Glyn Davies and Philip Irving. *Impact, post-impact strength, and post-impact fatigue behavior of polymer composites.* Elsevier Ltd, 2020.

[8] John-Alan Pascoe. Slow-growth damage tolerance for fatigue after impact in FRP composites: Why current research won't get us there. *Theoretical and Applied Fracture Mechanics*, 116:103127, 2021.

[9] Compass ASTM D7137 D7137M-17. Standard test method for compressive residual strength properties of damaged polymer matrix composite plates.

[10] Federal Aviation Administration. Composite aircraft structure. Advisory circular 20-107B, 2010.

[11] European Union Aviation Safety Agency. Annex ii - amc 20-29 to ed decision 2010/003/r. Technical report, 2010.

[12] D. J. Bull, S. M. Spearing, and I. Sinclair. Observations of damage development from compression-after-impact experiments using ex situ micro-focus computed tomography. *Composites Science and Technology*, 97:106–114, 2014.

Aknowledgements

I would like to express my deepest gratitude to all those who have supported me throughout the journey of completing this thesis.

To my daily supervisor, John-Alan Pascoe. A lot has changed since our first online meetings during the Covid era. Over the years, you entrusted me with freedom, consistently encouraging my curiosity while gently steering me back on course when I strayed too far from the main path (which happened often). Your genuine motivation has always been my academic and personal growth, and for that, I will always be grateful.

To my promotor, René Alderliesten, thank you for your insightful advice and critical, thought-provoking questions. Your guidance has been invaluable, not only in enhancing the quality of my work but most importantly for my development as a researcher.

In the course of my Ph.D., I spent countless hours manufacturing impacting and breaking coupons. Alexander, Chantal, Dave, Fred, Johan and Victor, your technical help has been invaluable. Science is about making discoveries. Some of mine included finding all the problems with the testing machines. Apologies for all the trouble along the way!

To the secretaries of AS&M department Gemma, Mylène, Shanta and Tess, thank you for your hard work. Gemma, from my first day in the Netherlands, you have been there, helping me settle in and navigate bureaucratic challenges. I am extremely grateful for your support.

To my friends and colleagues - Abhas, Alessandro C., Alessandro P., Andrea, Antonio, Billy, Caroline, Chantal, Daniele, Demetrio, Eva, Fabio, Federica, Ferda, Francesco F., Francesco M., Francesco N., Francisco, George, Gioele, Giovanna, Huub, Ines, Javier, Kevin, Lorenzo, Lubin, Luigi, Mariana, Matteo, Michele, Mirko, Morteza, Muhammad, Onur, Panos, Rosemere, Sasan, Satya, Silvia, Stratos, Thanos, Wenjie, and Xavier - thank you for being there when I needed you and for all the good times. I cherish all the discussions, especially the silly ones.

To my parents, Andrea and Cristina, my sister Giorgia, and my grandparents, Anna e Piero, thank you for your love and care.

To those who were there, and to those who are no longer here but are still present in my heart.

I am deeply grateful to each one of you.

Davide

Curriculum Vitæ

Davide Biagini

The author was born in Modena, Italy, on August 28, 1995.

In 2014, he graduated from the Scientific High School A. Tassoni in Modena. Following this, he enrolled in the Aerospace Engineering program at the University of Bologna campus in Forlì, earning his Bachelor's degree in 2017.

The author continued at the University of Bologna for his master's degree, during which he undertook a four-month internship at the Delft University of Technology in the Netherlands. There, he worked on his master's thesis under the joint supervision of Dr. Calvin Rans (TU Delft) and Dr. Enrico Troiani (University of Bologna). After completing his internship, he graduated cum laude from the University of Bologna in March 2020 obtaining a Master of Science in Aerospace Engineering.

In April 2020, he started his Ph.D. project at TU Delft, supervised by Dr. Ir R.C. Alderliesten as promotor and Dr. Ir J.A. Pascoe as co-promotor and daily supervisor.

List of Publications

- *Davide Biagini, John-Alan Pascoe, René Alderliesten*: Investigation of compression after impact failure in carbon fiber reinforced polymers using acoustic emission. Journal of Composite Materials, 57(10):1819–1832, 2023.
- *Davide Biagini, John-Alan Pascoe, René Alderliesten*: Investigating apparent plateau phases in fatigue after impact damage growth in CFRP with ultrasound scan and acoustic emissions. International Journal of Fatigue, 177:107957, 2023.
- *Davide Biagini, John-Alan Pascoe, René Alderliesten*: Experimental investigation of fatigue after impact damage growth in cfrp. Procedia Structural Integrity, 42:343–350, 2022. 23 European Conference on Fracture.

Included in this thesis.